PIONEER AND ACADEMIC STUDIES IN ENGINEERING



All Sciences Academy

PIONEER AND ACADEMIC STUDIES IN ENGINEERING

Editor Asst. Prof. Dr. Umut ÖZKAYA





Pioneer and Academic Studies in Engineering Editor: Asst. Prof. Dr. Umut ÖZKAYA

Design: All Sciences Academy Design

Published Date: June 2025

Publisher's Certification Number: 72273

ISBN: 978-625-5900-62-3

© All Sciences Academy

www.allsciencesacademy.com allsciencesacademy@gmail.com

CONTENT

1. Chapter	6
Digital Twin Based Smart Cities with Focus on Frameworks Applications Research Frontiers	s and
Casim YAZICI	
2. Chapter	24
Investigation of the Effect of Heat Transfer Performance and Temperatur Distribution in a Rotating Industrial Roller with a Novel Spiral Groove D	
Mahir ŞAHİN, Mustafa KILIÇ	
3. Chapter	44
An Investigation on Design Criteria of Heat Exchangers by Using Tree Models of Machine Learning Methods	
Mahir ŞAHİN, Mustafa KILIÇ, Merve ALA	
4. Chapter	58
LSTM-Based Regional Load Forecasting for Electricity Distribution Feed The Bölcek Case	ders:
Turgay ÖZZEFTCİ, İlker DURSUN	
5. Chapter	69
Analysis of uncontrolled blowouts from oil and gas drilling	
Timur Chis, AL-Gburi Hasan Ali Mosleh, Daniel Iancu	
6. Chapter	84
Risk assessment in the operation and safety of marine oil installations	
Timur Chis, Daniel Iancu, AL-Gburi Hasan Ali Mosleh	
7. Chapter	95
High-Performance and Durable DSSCs with PtNP/PANI/g-CN	
Nanocomposites: Moving Beyond Traditional Platinum Electrodes	
Mücella ÖZRAY KARAKUS	

Digital Twin Based Smart Cities with Focus on Frameworks Applications and Research Frontiers

Casim YAZICI¹

¹ Asst. Prof. Dr.; Department of Construction, Ağrı İbrahim Çeçen University, 04100 Ağrı, cyazici@agri.edu.tr Türkiye, ORCID: 0000-0002-2061-4275

ABSTRACT

This chapter explores the transformative role of digital twin (DT) technologies in shaping the future of smart cities. By creating real-time, virtual replicas of physical urban systems, DTs enable advanced monitoring, predictive analytics, and data-driven decision-making across multiple domains including urban planning, disaster management, energy, transportation, and citizen engagement. The chapter synthesizes findings from 41 peer-reviewed studies to present a comprehensive overview of current DT architectures, application frameworks, and integration challenges. Particular attention is given to the convergence of DTs with artificial intelligence, Internet of Things (IoT), and immersive technologies to enhance real-time situational awareness and participatory governance. The social digital twin paradigm, which emphasizes equity, privacy, and public involvement, is discussed as a critical direction for future development. Moreover, the chapter examines key implementation barriers such as data interoperability, cybersecurity, and algorithmic accountability. Through the inclusion of schematic diagrams and a domainspecific application table, the chapter offers both conceptual insights and practical guidance for researchers, practitioners, and policy-makers. Ultimately, it argues that digital twins are not merely technological innovations, but socio-technical systems capable of supporting more resilient, inclusive, and sustainable urban futures.

INTRODUCTION

Digital twin (DT) technology has emerged as a transformative paradigm in urban innovation, enabling real-time monitoring, simulation, and optimization of complex urban systems. The integration of DT into smart cities offers significant opportunities for urban planning, infrastructure management, disaster resilience, energy optimization, and citizen-centric governance. Unlike traditional static models, digital twins represent dynamic, continuously updated virtual counterparts of physical city components, drawing from real-time sensor data, geographic information systems, and predictive analytics.

The widespread deployment of Internet of Things (IoT) devices and the proliferation of big data analytics have further empowered DT applications in urban environments. For instance, Li et al. proposed a deep learning-based data processing framework utilizing CNN architectures to enhance the efficiency and accuracy of data transmission in IoT-enabled digital twin networks for smart cities (Batty, 2020). Furthermore, Ma et al. emphasized that DT-based smart city governance fosters transparency, accountability, and inclusive participation in policy-making processes (Fuller et al., 2021).

In the context of sustainable development, DTs play a critical role in energy management and environmental monitoring. Alvi et al. demonstrated that digital twin systems can support multi-domain integration, enabling predictive maintenance and resilience-oriented urban policies (Alvi et al., 2023). Similarly, White et al. explored how citizen feedback can be embedded into urban DT platforms to facilitate participatory planning and democratic engagement (White et al., 2022).

Given these multifaceted applications and potential benefits, there is an urgent need to consolidate fragmented research findings into a structured framework. This chapter aims to synthesize the current body of knowledge on digital twinbased smart cities, identify key application domains, discuss prevailing technical and governance challenges, and suggest directions for future research.

CONCEPTUAL FOUNDATIONS AND DEFINITIONS

Digital twin (DT) technology is rooted in the convergence of computational modeling, cyber-physical systems, and real-time data analytics. The concept was initially adopted in manufacturing and aerospace industries, particularly by NASA in the early 2000s for spacecraft health monitoring. Over the past decade, DTs have been progressively integrated into urban systems, aligning with the proliferation of IoT infrastructure, GIS data, and artificial intelligence (AI) applications.

A digital twin is broadly defined as a virtual replica of a physical entity or system that continuously receives real-time data from sensors, processes, and user inputs to simulate, analyze, and predict behaviors of its physical counterpart. In the context of smart cities, DTs serve as cybernetic feedback systems that integrate multi-source urban data—including transportation, energy, waste, environment, and population dynamics—into centralized digital environments (Batty, 2020), (Yang and Kim, 2022). These environments facilitate decision-making, predictive maintenance, and adaptive planning.

Several architectural frameworks have been proposed for urban DTs. For example, the architecture outlined by Yang and Kim includes layers such as data acquisition, modeling, analytics, and interface modules that connect users to actionable insights (Khan et al., 2024). The core components of an urban DT typically encompass:

- Data Layer: Real-time streaming from IoT sensors, mobile networks, satellite imagery, and GIS databases.
- Modeling Layer: Integration of BIM, physics-based models, and statistical models.
- Processing Layer: Use of AI and ML algorithms for pattern recognition, forecasting, and anomaly detection.

 Visualization Layer: Dashboards, immersive 3D interfaces, and AR/VR components.

Digital twins in urban settings are often coupled with Building Information Modeling (BIM) systems, allowing detailed, object-oriented representations of infrastructure. When integrated with AI and machine learning, DTs evolve into autonomous systems capable of optimizing urban resource allocation (Ravid and Gutman, 2022).

Recent studies have further expanded the DT paradigm by introducing the concept of the "social digital twin," wherein human behaviors, preferences, and interactions are modeled alongside physical systems. This approach aims to enrich participatory governance and improve urban livability by capturing socio-spatial patterns (Askary et al., 2023).

As the technological landscape matures, the definition of urban digital twins is increasingly context-sensitive, shaped by factors such as city scale, administrative goals, and stakeholder interests. This diversity necessitates flexible, modular, and scalable frameworks that can adapt to specific urban challenges while ensuring interoperability, security, and ethical data use.

APPLICATION DOMAINS OF URBAN DIGITAL TWINS

Digital twin systems are being integrated across a variety of urban domains, enabling enhanced monitoring, simulation, and decision-making capabilities. These applications range from infrastructure modeling and traffic optimization to public health monitoring and citizen engagement platforms. Table 1 presents an overview of smart city domains and the corresponding digital twin applications identified in the literature.

Table 1. Smart city domains and corresponding digital twin applications.

Smart City Domain	Digital Twin Applications
Urban Planning	3D city modeling, zoning simulations, infrastructure planning
Disaster	Risk assessment, early warning systems, response
Management	coordination
Energy Systems	Smart grid simulation, load forecasting, energy efficiency monitoring
Transportation	Traffic flow prediction, real-time navigation, fleet management
Citizen Engagement	Participatory planning platforms, feedback collection, sentiment analysis
Healthcare	Hospital capacity monitoring, outbreak simulation, patient tracking
Environmental	Air quality monitoring, pollution source analysis,
Monitoring	sustainability forecasting

Urban Planning and Infrastructure Optimization

Urban planning is one of the most prominent application areas of digital twin (DT) technologies in smart city development. Through the creation of real-time, data-rich virtual models of urban spaces, DTs enable the simulation of infrastructural scenarios, predictive modeling of urban growth, and optimization of land-use strategies. The capacity to model, analyze, and visualize urban systems at varying spatial and temporal scales facilitates proactive planning and supports policy makers in managing rapidly expanding metropolitan areas.

A key advantage of DTs in urban planning lies in their ability to integrate heterogeneous data sources such as satellite imagery, building information models (BIM), traffic sensors, demographic datasets, and environmental indicators. For instance, Askary et al. demonstrated how DT models incorporating UAV-based photogrammetry and LiDAR scanning can be used for heritage-informed urban planning, allowing city planners to reconcile developmental goals with conservation priorities (Lee et al., 2022). Similarly, in the work by Liu et al., a multilayered urban DT architecture was proposed to simulate underground utility networks in conjunction with above-ground urban infrastructure, enhancing resilience and coordination in large-scale redevelopment projects (Ford and Wolf, 2021).

Digital twins are also instrumental in transportation planning and mobility management. By leveraging real-time data streams and AI-driven simulation, urban DTs can optimize traffic flows, reduce congestion, and assess the impact of new transport policies prior to their implementation. In this context,

the study by Ghosh et al. introduced a DT-enabled traffic simulation platform to evaluate multi-modal transit solutions under various urban stress conditions (Ahmed et al., 2022).

Moreover, urban DTs support scenario-based infrastructure investment planning. Stakeholders can simulate multiple urban development pathways under constraints such as climate change projections, energy demands, and population growth trajectories. This approach enables data-informed decision-making that is both agile and evidence-based.

In summary, digital twins transform traditional urban planning by facilitating holistic, anticipatory, and participatory approaches. By serving as decision-support environments, they help city officials, engineers, and residents co-create adaptive infrastructure systems that are resilient, efficient, and sustainable.

Energy Management and IoT Integration

Digital twin (DT) technology has emerged as a powerful enabler of energy efficiency and sustainability in the context of smart cities. By integrating Internet of Things (IoT) infrastructures with predictive data analytics, DTs provide a dynamic and real-time understanding of urban energy consumption, distribution, and infrastructure performance. This facilitates intelligent energy management strategies, demand-response planning, and integration of renewable energy sources.

One of the foundational contributions in this domain is the implementation of IoT-driven sensor networks within digital twin frameworks to enable real-time monitoring of energy consumption patterns across buildings, public lighting systems, and transportation nodes (Alarifi et al., 2023). For example, Khan et al. proposed a digital twin system to monitor and optimize energy flow in smart grid infrastructure, emphasizing its role in reducing system latency and improving fault detection capabilities (Lee et al., 2022).

Moreover, DTs support simulation-based optimization for microgrid control and distributed energy resource integration. In their work, Ahmed et al. developed a comprehensive digital twin platform for hybrid energy systems, combining wind, solar, and battery storage models with AI-powered forecasting algorithms to achieve resilient energy planning in urban districts (Ahmed et al., 2022). This kind of integration allows cities to mitigate energy supply risks and improve sustainability indices.

Digital twins also facilitate the deployment of smart meters and adaptive control systems. These technologies enable not only real-time data acquisition but also two-way communication between energy providers and consumers. According to the findings of Zhong et al., such capabilities contribute to the development of intelligent energy dashboards that promote transparency and

informed decision-making at both the individual and municipal levels (Yang and Kim, 2022).

Furthermore, energy-oriented DTs serve as a basis for evaluating the impact of urban climate conditions on energy demand. By coupling environmental data with building performance simulations, cities can devise climate-resilient retrofitting strategies. In this context, the work of Lu et al. provides a case study of climate-responsive DT models that inform policy frameworks for green infrastructure development (Ford and Wolf, 2021).

In conclusion, digital twins integrated with IoT systems represent a transformative approach to urban energy management. They enable proactive planning, enhance operational efficiency, and support the transition to low-carbon cities by facilitating the intelligent orchestration of energy networks and consumer behaviors.

Citizen Engagement and Participatory Platforms

Citizen engagement is a fundamental component of inclusive urban governance and a critical domain for the application of digital twin (DT) technology. Urban DTs provide a platform for real-time dialogue between citizens and decision-makers, facilitating participatory planning, feedback integration, and social innovation. Unlike conventional top-down governance models, DT systems can incorporate grassroots-level inputs through crowdsensing, social media data, and mobile feedback mechanisms.

One key development in this domain is the integration of the "social digital twin" concept, which expands traditional DT models to include human behaviors, preferences, and social interactions. According to Ravid and Gutman, social digital twins help model citizen engagement dynamics and create spaces for digital deliberation in urban planning processes (Ravid and Gutman, 2022). These models not only represent physical environments but also the emotional and experiential aspects of living in the city.

Digital twin platforms also enable co-creation and participatory simulations. For instance, the VELUX Living Places project integrated user-generated feedback into its digital models to evaluate citizen satisfaction with new urban designs (White et al., 2022). Similarly, the MetaOmniCity framework developed by Lee et al. utilizes immersive technologies and social data to generate multi-user participatory spaces in the metaverse, creating new forms of democratic urban interaction (Askary et al., 2023).

In practice, citizen feedback integrated into urban DTs can affect real-time decisions related to public services, traffic rerouting, safety alerts, and event management. For example, Ford and Wolf demonstrated that DT systems can process citizen-reported emergency data to improve the efficiency of disaster response and municipal coordination (Alarifi et al., 2023).

Despite their potential, participatory DTs also raise challenges related to digital literacy, data bias, and inclusion. Ensuring equitable access and preventing marginalization requires the design of user-friendly interfaces and policies for ethical data use. As such, future systems must balance technical sophistication with social sensitivity.

In summary, digital twins foster a shift from centralized control to participatory urbanism by embedding citizen voices into the digital fabric of the city. These systems hold the potential to reshape civic engagement, making urban planning more transparent, inclusive, and responsive to community needs.

Smart Governance and Decision Support

Smart governance is one of the foundational pillars of digital twin (DT)-enabled smart cities, focusing on the integration of real-time data analytics, simulation tools, and collaborative platforms to enhance administrative decision-making. Unlike traditional governance models that often rely on static or outdated information, DT systems empower policy makers with up-to-date, contextual insights derived from multiple data streams including IoT sensors, satellite imagery, demographic trends, and socio-economic indicators.

Ma et al. demonstrated that DT-driven governance frameworks facilitate transparency and inclusivity by allowing stakeholders to visualize the implications of proposed policies before their implementation (Fuller et al., 2021). Through scenario modeling and what-if analysis, DT platforms help urban administrators understand the cascading effects of decisions across multiple domains, including transportation, energy, health services, and public safety.

Digital twins also support multi-agency coordination by enabling a shared digital environment where city departments can interact, simulate interventions, and resolve conflicting objectives. According to the framework proposed by Liu et al., a layered DT architecture improves data interoperability and facilitates the synchronization of various urban systems (Ford and Wolf, 2021). These features contribute to the creation of agile governance models that are both reactive and anticipatory.

Moreover, DTs can serve as regulatory compliance tools by tracking urban performance indicators in real time. For example, Ahmed et al. integrated energy usage analytics and emissions tracking into their DT platform, enabling city authorities to monitor progress toward sustainability goals and regulatory benchmarks (Ahmed et al., 2022). Such systems are increasingly important in the context of climate change adaptation and the implementation of global frameworks such as the UN Sustainable Development Goals.

However, the deployment of digital twins in governance contexts is not without challenges. Issues related to data privacy, algorithmic transparency, and equity in access must be addressed to ensure fair and effective implementation. The use of explainable AI and ethical data governance principles is critical to maintaining public trust in DT-enabled governance platforms.

In conclusion, smart governance powered by digital twins represents a paradigm shift toward evidence-based, adaptive, and participatory urban administration. By enabling continuous feedback loops, real-time analytics, and cross-sectoral collaboration, DTs have the potential to revolutionize how cities are governed in the 21st century.

Disaster Management and Resilience Building

Digital twins (DTs) have emerged as transformative tools in urban disaster risk management and resilience-building efforts. Through the integration of real-time sensor data, predictive simulation, and historical analysis, DTs provide cities with dynamic capabilities to anticipate, monitor, and respond to natural and anthropogenic hazards. These include seismic events, floods, wildfires, and pandemics.

One of the key applications of DTs in this domain lies in early warning and preparedness systems. DT platforms incorporate meteorological, hydrological, and geospatial data to simulate hazard scenarios and forecast the spatial and temporal impacts of disasters. Ford and Wolf developed a spatially explicit digital twin framework for urban disaster preparedness, illustrating its use in optimizing emergency response coordination and resource deployment across municipalities (Alarifi et al., 2023).

Another critical function is structural vulnerability assessment. By integrating Building Information Modeling (BIM) with DT platforms, it becomes possible to simulate structural responses to hazard loads in real time. Liu et al. proposed a layered DT architecture that supports vulnerability assessments and prioritization of post-disaster recovery based on digital replicas of built environments (Ford and Wolf, 2021). This integration aids emergency managers in identifying critical assets, planning evacuation strategies, and allocating recovery resources.

Digital twins also enable long-term urban resilience planning by simulating the effects of climate adaptation measures and urban retrofitting. Alvi et al. demonstrated how multi-domain DT systems can evaluate infrastructure performance under extreme conditions while accounting for socio-economic vulnerabilities (Alvi et al., 2023). Such capabilities support resilient design strategies and proactive policy-making.

Furthermore, participatory approaches to resilience are being facilitated by DT technologies. Platforms that incorporate citizen-generated data help improve situational awareness and align emergency responses with localized needs. White et al. highlighted how embedding real-time citizen feedback into DT systems enhances inclusiveness and effectiveness in disaster mitigation planning (White et al., 2022).

In summary, DTs offer a proactive, adaptive, and data-driven framework for managing disasters and enhancing urban resilience. By fusing real-time monitoring with predictive analytics and citizen engagement, these systems allow city administrators to move beyond reactive crisis response toward integrated risk governance.

This integration of digital twin systems into disaster management processes enables real-time monitoring of environmental, infrastructural, and social parameters. It supports predictive modeling, early warning generation, and scenario-based planning. Figure 1 presents a schematic overview of the system architecture used in digital twin-enhanced disaster resilience planning.

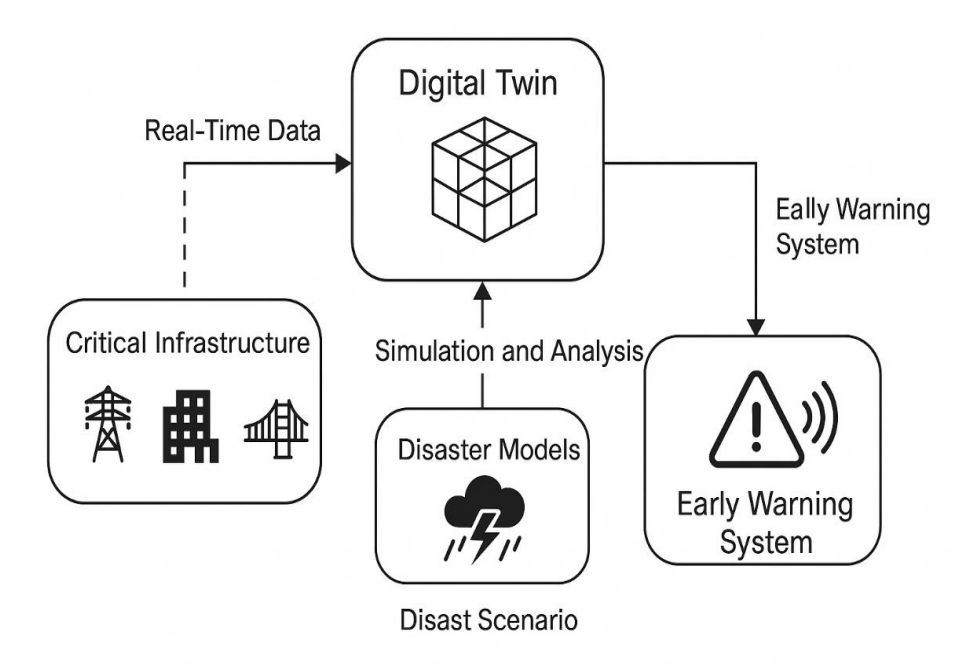


Figure 1. Digital twin architecture for disaster management.

Heritage Conservation and Cultural Digitalization

Heritage conservation has traditionally relied on physical archives, field surveys, and manual documentation, often constrained by limited accessibility

and vulnerability to degradation. Digital twin (DT) technology now offers a novel approach to preserving cultural assets through high-fidelity virtual representations that combine 3D scanning, geographic information systems (GIS), and historical data integration.

Digital twins in heritage contexts are developed using technologies such as photogrammetry, LiDAR scanning, and BIM to create accurate digital surrogates of monuments, historical buildings, and archaeological sites. Askary et al. demonstrated the use of drone-based photogrammetry to model ancient urban districts, facilitating both conservation and public engagement through interactive digital environments (Lee et al., 2022). These virtual reconstructions allow for remote inspection, condition monitoring, and immersive educational experiences.

In addition to preservation, DTs serve as tools for risk analysis and disaster recovery. Liu et al. presented a DT framework that integrates seismic hazard data with 3D models of cultural sites to assess vulnerability and prioritize retrofitting efforts (Ford and Wolf, 2021). This enables heritage managers to simulate various hazard scenarios and develop evidence-based mitigation strategies.

Digital twins are also reshaping cultural storytelling through virtual museums and digital archives. Virtual replicas allow for global access to culturally significant locations, democratizing heritage experiences and supporting inclusive educational initiatives. The work of Lee et al. with MetaOmniCity illustrates how immersive virtual spaces can be embedded with social narratives and community-generated content, enhancing the socio-cultural relevance of digital heritage models (Askary et al., 2023).

Moreover, DT platforms can be linked to sensor-based monitoring systems that track environmental stressors such as humidity, temperature, and vibration. These systems enable real-time condition assessments and maintenance planning, extending the lifespan of heritage structures.

Despite these advancements, several challenges remain, including the standardization of data formats, integration with archival systems, and intellectual property rights related to digitized heritage. Addressing these issues requires interdisciplinary collaboration among historians, engineers, data scientists, and legal experts.

In summary, digital twins provide a comprehensive, scalable, and interactive framework for cultural heritage conservation and dissemination. By bridging physical preservation with digital innovation, DTs play a critical role in safeguarding cultural identity and transmitting historical knowledge to future generations.

Immersive Systems and Metaverse Integration

The integration of immersive technologies with digital twins (DTs) represents a pivotal advancement in the evolution of smart cities, enabling more intuitive interaction with urban data and spatial phenomena. Augmented reality (AR), virtual reality (VR), and mixed reality (MR) tools allow stakeholders to visualize, manipulate, and experience urban environments in immersive formats, fostering new paradigms in planning, education, governance, and public engagement.

Digital twin systems enriched with AR and VR interfaces provide decision-makers, urban planners, and citizens with the ability to navigate city models in three-dimensional, dynamic contexts. These immersive environments support scenario-based exploration of infrastructure projects, emergency response drills, and sustainability simulations. According to Lee et al., the MetaOmniCity framework leverages immersive VR and social sensing technologies to construct metaverse-based digital twins that accommodate citizen participation and collaborative urban design (Askary et al., 2023).

Furthermore, the metaverse, a persistent and networked three-dimensional virtual space, offers a complementary platform for smart cities to extend digital twin capabilities beyond data visualization into experiential interaction. Smart city metaverses can host virtual town halls, community design sessions, and digital public consultations, enabling inclusive urban planning across geographic and demographic boundaries. Askary et al. highlighted the use of immersive visualization tools for heritage-informed planning, indicating their effectiveness in communicating complex spatial narratives to non-expert stakeholders (Lee et al., 2022).

Digital twin-based metaverses are also being explored for simulation training and capacity building in urban operations. Emergency responders, urban service providers, and students can engage in lifelike simulations to rehearse procedures, analyze decision-making outcomes, and understand urban dynamics. Ford and Wolf demonstrated the applicability of immersive DT platforms in disaster scenario rehearsals, improving preparedness and interagency coordination (Alarifi et al., 2023).

However, realizing the potential of immersive DT systems requires overcoming challenges related to interoperability, hardware accessibility, and computational performance. Scalable architectures must support large datasets, real-time rendering, and cross-platform compatibility. Additionally, privacy concerns and equitable access to immersive platforms must be addressed to avoid digital exclusion.

In conclusion, the convergence of digital twins and immersive systems signals a transformative shift in how cities are experienced, understood, and shaped. These technologies hold the potential to democratize urban decision-making,

enhance stakeholder collaboration, and promote experiential learning in the smart city domain.

TECHNICAL CHALLENGES AND DATA GOVERNANCE

The implementation of digital twin (DT) systems within smart cities presents numerous technical and governance-related challenges. As urban environments generate massive amounts of heterogeneous data from a multitude of sources including IoT devices, mobile applications, satellite imagery, and citizen-generated content, ensuring the seamless integration, security, and governance of this data becomes a critical concern.

One of the most fundamental technical challenges in urban DT systems is interoperability. Cities operate with legacy systems and diverse technological infrastructures that often lack standardized protocols for data exchange. As noted by Yang and Kim, achieving real-time data synchronization across departments and platforms necessitates modular architectures and open standards that support cross-domain integration (Khan et al., 2024). Without such mechanisms, DT systems remain fragmented, reducing their effectiveness in decision support and policy implementation.

Scalability is another major barrier. As cities grow and adopt more sensors and digital services, DT platforms must be capable of processing and analyzing vast volumes of data in real time. Alvi et al. highlighted the importance of scalable data management frameworks that can handle high-frequency inputs and support edge computing for latency-sensitive applications (Alvi et al., 2023). However, this scalability must also be accompanied by efficient data compression, cloud integration, and optimized storage strategies to avoid overloading system infrastructure.

Data governance is equally critical. The growing reliance on personal and behavioral data within DT models raises serious privacy concerns. Ravid and Gutman introduced the concept of the social digital twin, where individuals' preferences, movements, and sentiments are modeled in conjunction with physical infrastructure (Ravid and Gutman, 2022). While this enriches participatory urban planning, it also demands rigorous ethical standards, transparent algorithms, and robust data anonymization techniques to prevent misuse and ensure compliance with regulations such as the GDPR.

Cybersecurity is another pressing issue. Smart city DTs are attractive targets for cyber-attacks due to the sensitive nature of the data they collect and process. Khan et al. emphasized the need for multi-layered cybersecurity strategies that include secure communication protocols, threat detection systems, and resilient network architectures (Lee et al., 2022). Ensuring the integrity and confidentiality of data is essential for maintaining public trust and system reliability.

Legal and institutional challenges also persist. Questions about data ownership, consent, liability, and access rights must be addressed through comprehensive regulatory frameworks. White et al. advocated for participatory governance models that involve citizens in setting data usage policies, thereby promoting legitimacy and transparency (White et al., 2022). However, such frameworks must balance inclusivity with administrative efficiency, ensuring that data-driven innovation does not stall due to bureaucratic inertia.

In addition to policy-level challenges, technical issues such as real-time data fusion, semantic heterogeneity, and spatio-temporal alignment of datasets complicate the design of accurate and responsive DT systems. Ford and Wolf noted that emergency preparedness applications require not only rapid processing of heterogeneous inputs but also contextual interpretation to support actionable insights (Alarifi et al., 2023). Addressing these challenges calls for advancements in AI, federated learning, and knowledge graph-based reasoning within DT ecosystems.

In conclusion, while digital twins offer significant opportunities for smarter urban governance, their implementation is hindered by multifaceted technical and governance challenges. Ensuring interoperability, privacy, scalability, and regulatory compliance requires interdisciplinary collaboration among urban planners, computer scientists, policy makers, and legal experts. Only through such coordination can digital twins reach their full potential as trusted and intelligent urban infrastructure systems.

FUTURE RESEARCH DIRECTIONS AND OPEN PROBLEMS

Despite significant advancements in the development and deployment of digital twin (DT) systems for smart cities, several critical research gaps and unresolved challenges remain. Future investigations must address these limitations by advancing technological capabilities, refining conceptual models, and fostering interdisciplinary collaborations.

First, the integration of digital twins with emerging technologies such as edge computing, federated learning, and quantum computing remains an underexplored frontier. Current DT platforms heavily rely on centralized cloud infrastructures, which often result in latency and privacy issues. Transitioning toward decentralized architectures could enhance real-time responsiveness and data sovereignty. Researchers such as Ahmed et al. have begun exploring hybrid DT models incorporating edge nodes, but further empirical validation is needed to assess their scalability and reliability in large urban contexts (Ahmed et al., 2022).

Second, the social dimension of digital twins warrants deeper theoretical and methodological attention. While the concept of the social digital twin

introduced by Ravid and Gutman provides a foundation for modeling human behaviors and preferences, there is a lack of standardized frameworks to capture, analyze, and visualize these complex social dynamics (Ravid and Gutman, 2022). Future research should develop robust ontologies and agent-based modeling techniques to represent citizens not only as data points but as active stakeholders with evolving preferences and interactions.

Interoperability remains a persistent challenge. Many existing DT implementations are developed as bespoke systems that lack the ability to interface with legacy infrastructure or other urban platforms. Yang and Kim highlighted the need for open-source standards and modular architectures, yet there is limited consensus on universal protocols or APIs that could facilitate seamless data exchange (Khan et al., 2024). Developing these standards is essential for scaling DT solutions across multiple urban domains and jurisdictions.

Moreover, there is a need for advanced explainable artificial intelligence (XAI) techniques within DT systems. As digital twins increasingly rely on black-box AI models for prediction and decision-making, it becomes imperative to ensure transparency, accountability, and interpretability of outcomes. Future work should explore how XAI methods can be embedded into DT dashboards to assist policymakers and citizens in understanding and trusting algorithmic recommendations.

Longitudinal validation and benchmarking of DT systems also represent a research gap. Most existing studies focus on proof-of-concept models or short-term simulations without assessing long-term system performance, resilience, or social acceptance. Comprehensive longitudinal studies are necessary to evaluate the sustained impact of DTs on urban governance, resource management, and quality of life.

Furthermore, ethical and legal frameworks governing digital twin deployment are still nascent. As highlighted by White et al., participatory data governance is essential, but there is limited empirical research on the effectiveness of existing frameworks and the conditions required for equitable implementation (White et al., 2022). Future studies should investigate models for institutional coordination, citizen consent mechanisms, and algorithmic accountability.

Lastly, immersive DT applications, including those in the metaverse, require further interdisciplinary collaboration. While efforts such as MetaOmniCity represent promising integrations of VR and social data, there is limited knowledge on the cognitive, social, and behavioral impacts of these environments (Askary et al., 2023). Collaborative research among urban planners, psychologists, designers, and engineers is needed to ensure that immersive DT platforms promote inclusivity, accessibility, and well-being.

In conclusion, digital twin technologies for smart cities are entering a phase of maturation and diversification. To unlock their full transformative potential, future research must address unresolved technical, social, ethical, and methodological questions through holistic and multidisciplinary approaches. This will ensure that DT systems evolve as inclusive, resilient, and intelligent infrastructures for sustainable urban development.

CONCLUSION

Digital twin (DT) technologies are rapidly transforming the conceptualization, operation, and governance of smart cities by enabling real-time integration of physical and digital systems. As demonstrated throughout this chapter, the deployment of DT frameworks across diverse domains-ranging from urban planning and energy management to disaster resilience and citizen engagement-has enabled a shift toward data-informed, participatory, and adaptive urban development.

The literature reviewed in this chapter underscores the importance of modular architectures, real-time analytics, and interoperability standards in developing scalable DT platforms (Khan et al., 2024), (Ford and Wolf, 2021), (Lee et al., 2022). Furthermore, the convergence of DTs with immersive technologies and the social digital twin paradigm introduces novel opportunities for participatory governance, democratized urban planning, and enhanced public engagement (Ravid and Gutman, 2022), (Askary et al., 2023), (Alarifi et al., 2023).

Nonetheless, the advancement of DT systems is hindered by critical challenges such as data governance, algorithmic transparency, cybersecurity, and ethical concerns related to privacy and inclusion. These issues must be addressed through interdisciplinary collaboration and regulatory innovation. As White et al. and Ravid and Gutman argue, participatory frameworks and human-centric models are necessary to ensure equitable access and public trust in DT-enabled decision-making (White et al., 2022), (Ravid and Gutman, 2022).

In light of these insights, this chapter proposes several key recommendations for researchers and policy makers. First, future DT implementations must adopt open standards and federated architectures to facilitate interoperability and decentralization (Khan et al., 2024), (Ahmed et al., 2022). Second, longitudinal studies are required to evaluate the socio-technical impacts of DT systems over time. Third, immersive DT applications must be co-designed with diverse stakeholders to avoid digital exclusion and maximize societal value (Lee et al., 2022), (Askary et al., 2023).

In conclusion, digital twins are not merely technological tools but sociotechnical systems with the potential to redefine urban life. Their successful

integration into smart cities demands holistic strategies that blend technical excellence with ethical foresight, institutional coordination, and active citizen participation.

REFERENCES

Ahmed, S., Malik, H. and Shahbaz, M. (2022). Breaking down data sharing barrier of smart city: A digital twin approach. Future Generation Computer Systems, 137, 331–345.

Alarifi, L., Almazyad, R., Alhussein, A. and others. (2023). Situation awareness of energy Internet of Things in smart city based on digital twin: From digitization to informatization. Digital Communications and Networks, 9(2), 416–425.

Alvi, A., Rehman, S. U., Shah, M. and Kim, S. W. (2023). Digital twin in smart cities: Recent advances, architecture, and open challenges. Future Generation Computer Systems, 141, 221–239.

Askary, T., Shen, J. and Zhang, A. (2023). Smart city platform enabling digital twin. Buildings, 13(3), 775.

Batty, M. (2020). Digital twins. Environment and Planning B: Urban Analytics and City Science, 47(4), 507–510.

Ford, R. and Wolf, M. (2021). Smart cities with digital twin systems for disaster management. In Proceedings of the 16th International Conference on Availability, Reliability and Security (ARES) (pp. 1–6).

Fuller, J., Fan, A., Day, C. and Barlow, T. (2021). Digital twin: Enabling technologies, challenges and open research. Journal of Manufacturing Systems, 58, 719–730.

Khan, K., Salah, A., Iqbal, F. and Imran, M. (2024). Digital twins in smart cities: Applications, architectures, and challenges. Future Internet, 16(1), 47.

Lee, J., Lim, M., Choi, S. and Jung, J. (2022). MetaOmniCity: Toward immersive urban metaverse cyberspaces using smart city digital twins. Scientific Reports, 12(1), 16278.

Ravid, Y. and Gutman, A. (2022). The social digital twin: The social turn in the field of smart cities. Urban Planning, 7(3), 348–359.

White, G., Johnson, M., Shah, A. and Barton, R. (2022). Barriers to the adoption of digital twins in smart cities: A sociotechnical perspective. Information Systems Frontiers, 24(6), 1571–1587.

Yang, L. and Kim, H. (2022). Digital twin-driven smart city architecture: A systematic literature review. Sustainable Cities and Society, 76, 103526.

Investigation of the Effect of Heat Transfer Performance and Temperature Distribution in a Rotating Industrial Roller with a Novel Spiral Groove Design

Mahir ŞAHİN¹

Mustafa KILIÇ²

¹⁻ Res. Asst.; Adana Alparslan Türkeş Bilim ve Teknoloji Üniversitesi Makine Mühendisliği Bölümü. msahin@atu.edu.tr ORCID No: 0000-0002-9565-9160

²⁻ Prof. Dr.; Adana Alparslan Türkeş Bilim ve Teknoloji Üniversitesi Makine Mühendisliği Bölümü. mkilic@atu.edu.tr ORCID No: 0000-0002-8006-149X

ABSTRACT

Industrial rollers are widely used for various applications, such as facilitating product flow, subjecting products to thermal treatments, and maintaining specific moisture conditions. However, traditional industrial rollers often consume excessive amounts of cooling fluid to achieve these goals. In this study, a novel roller design was developed, and its design parameters were optimized using ANSYS Fluent software based on the Moving Reference Frame (MRF) method. The parameters investigated include the rotational velocity of the roller (n = 0-90 rpm), Reynolds number of the fluid (Re = 4000-10000), and spiral groove spacing (L = 15-36 mm). Results indicated that increasing the rotational velocity from 0 to 90 rpm enhanced heat transfer effectiveness by 12.8%. Decreasing the Reynolds number from 10000 to 4000 resulted in a 15.1% improvement in heat transfer effectiveness, while reducing the groove spacing from 36 mm to 15 mm improved effectiveness by 24%. Based on these findings, it is evaluated that improved roller designs can be developed to increase heat transfer rates and achieve more homogeneous temperature distributions in industrial applications.

Keywords – Heat transfer, rotating roller, temperature distribution, spiral groove.

INTRODUCTION

Industrial rollers are highly durable cylindrical structures that play a critical role in maintaining products at desired thermal conditions, ensuring structural stability, and enhancing production efficiency in various industrial applications. Typically manufactured from steel or similarly durable materials, the design of these rollers varies significantly according to their intended application area and the characteristics of the processed products. These rollers perform critical functions across diverse industrial settings, including metal processing, textiles, paper production, and plastic manufacturing, and their designs are optimized according to specific operational conditions and product requirements. By ensuring consistent temperature distribution and reliable operation, industrial rollers enable continuous production lines and the maintenance of product quality standards. Moreover, their adaptable structures allow easy integration into different production processes, contributing positively to manufacturing productivity and product consistency (Berni et al., 2021:190), (Alam, 2022:105132), (Fénot et al., 2011:1138), (Tachibana et al., 1960:119), (Ullah et al., 2023:119), (Kilic et al., 2023:147), (Gunes et al., 2023:1117).

There are numerous studies in literature examining the performance characteristics of industrial rollers and rotating cylinders. For instance, Du et

al. (2017:638) extensively studied the influence of rotational conditions on the performance of vortex cooling systems, examining parameters such as rotational number, rotational direction, and density ratio. Their results indicated that increasing rotational number caused reductions in flow velocity and pressure, while the direction of rotation had no significant impact on vortex cooling performance. Additionally, an increase in the density ratio enhanced heat transfer intensity. Baghel et al. (2020:120487) performed a detailed investigation of heat transfer due to a water jet impinging on a semi-cylindrical curved surface. In their study, the ratio of cylindrical surface diameter to nozzle diameter (D/d) and Reynolds number were considered primary parameters. The results showed that increasing Reynolds number enhanced heat transfer efficiency by increasing the Nusselt number. Zhao et al. (2020:118819) examined the effects of spray cooling on temperature distribution over roller surfaces, considering parameters such as heat flux, nozzle-to-surface distance, and spray pressure. Experimental results revealed that flow velocity significantly influenced heat transfer.

In a study by Dalgic et al. (2021:1348), the effects of adiabatically rotating cylinders on fluid dynamics and heat transfer performance were investigated in detail. Their results showed that applying varying rotational velocities in different regions of the cylinder significantly enhanced fluid dynamics and heat transfer compared to stationary conditions. Liu et al. (2017:411) investigated thermal stresses on cylinder surfaces under varying Reynolds numbers, rotational velocities, and different fluid types (ATF, isobutyl-alcohol, water, acetone). Their findings demonstrated that ATF exhibited superior heat transfer performance compared to other fluids, while increases in rotational velocity and Reynolds number significantly reduced surface temperatures. Jahedi et al. (2019:124) studied the cooling process of a hollow cylinder using impinging jets, focusing on parameters such as water jets, flow rate, rotational velocity, jet spacing, and angular positioning. Their goal was to achieve higher heat flux, lower surface temperatures, and a reduction in individual jet mass flow rates of up to 50%, noting a significant effect at a rotational velocity of 30 rpm. Yurtseven (2021:552) comprehensively compared heat transfer performance in roller models with different fluid channel configurations under varying operating conditions. Results highlighted that models with converging spiral channel designs provided significant advantages in achieving uniform surface temperature distributions. Hamraoui (2009:2386) numerically analyzed temperature distribution within a single hollow cylinder used in rolling mills, examining the detailed effects of cylinder rotation speed and heat exchange with surroundings on temperature behavior. Luo et al. (2021:121749) numerically investigated the hydrodynamic effects of sequential droplet impingement on cylinder surface heat transfer, concluding that decreasing the vertical spacing between droplets enhanced heat transfer effectiveness. Selimefendigil et al. (2018:233) studied nanofluid impinging jet cooling between an adiabatically rotating cylinder and an isothermal surface, considering Reynolds numbers (100–400), angular velocity (–0.1 to 0.1), horizontal position (0–3.75), and particle volume fraction (0–0.04). Their results indicated that the highest particle concentration increased the Nusselt number by 8.08%, demonstrating improved heat transfer at higher Reynolds numbers.

In literature studies, heat transfer performance and temperature distribution in industrial rollers and cylinders have been investigated extensively in terms of roller geometry, surface cooling methods, fluid velocities, impinging jets, and different types of cooling fluids, including nanofluids. Unlike previous studies, this research presents a novel roller design featuring a spiral channel embedded within the hollow roller wall. Numerical investigations were conducted to analyze the effects of fluid velocity-dependent Reynolds number, spiral groove spacing, and rotational velocity of the roller on heat transfer performance.

MATERIALS AND METHODS

Numerical Modelling

The industrial roller design was generated using ANSYS CFD software within the SpaceClaim module, as illustrated in Figure 1. The roller has an outer diameter of 132 mm and a length of 394 mm. Spiral channels with a diameter of 9.5 mm were positioned inside the roller wall at a distance of 5.25 mm from the outer surface. The roller itself is composed of aluminum.

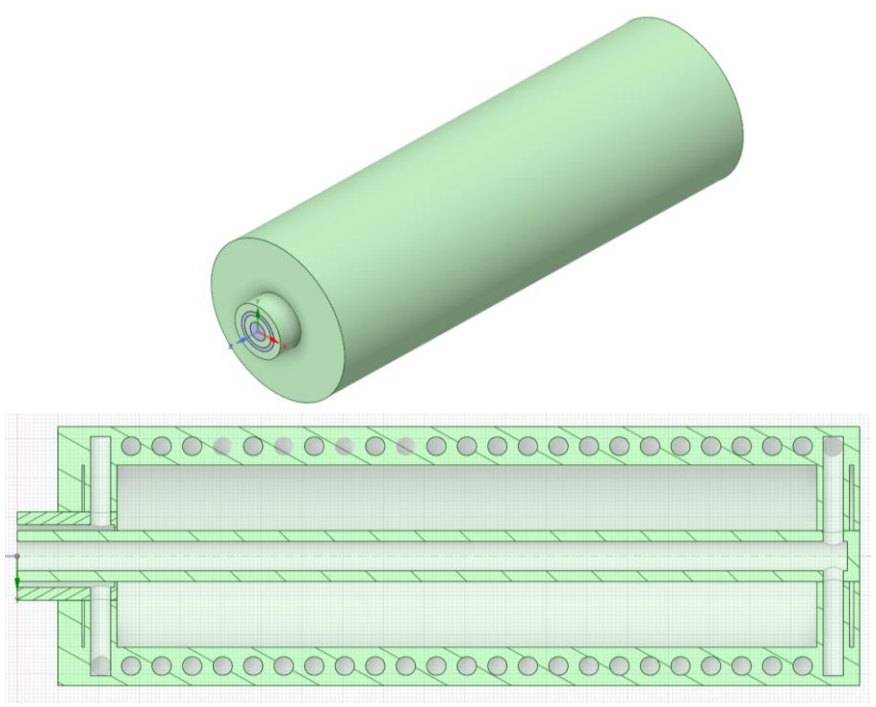


Figure 1: 3D model and cross-section view of the industrial roller

Pure water was chosen as the working fluid, entering the roller at an inlet temperature of 15° C. The fluid entering the roller is evenly divided into two equal parts at the roller's far end, flowing in opposite directions through the spiral grooves. Each fluid stream circulates through its respective path within the grooves and exits the roller at the same side where the fluid initially entered. The roller surface is subjected to a uniform heat flux of $50,000 \text{ W/m}^2$.

Mathematical Formulation and Boundary Conditions

The governing equations for the steady-state heat transfer problem, including the continuity, momentum, and energy equations, are presented below. The equations are expressed in cylindrical coordinates to accurately represent the geometry of the rotating roller and the spiral groove structure, ensuring precise modeling of flow and heat transfer characteristics.

Continuity equation:

$$\frac{1}{r}\frac{\partial(ru_r)}{\partial r} + \frac{1}{r}\frac{\partial(u_\theta)}{\partial \theta} + \frac{\partial(u_z)}{\partial z} = 0$$

Momentum equations:

For r-direction:

$$\begin{split} p \left(\frac{\partial (u_r)}{\partial t} + u_r \frac{\partial (u_r)}{\partial r} + \frac{u_\theta}{r} \frac{\partial (u_r)}{\partial \theta} - u_\theta^2 + u_z \frac{\partial (u_r)}{\partial z} \right) \\ &= -\frac{\partial P}{\partial r} + p g_r \\ &+ \mu \left[\frac{1}{r} \frac{\partial}{\partial r} \left(r \frac{\partial u_r}{\partial r} \right) - \frac{u_r}{r^2} + \frac{1}{r^2} \frac{\partial^2 u_r}{\partial \theta} - \frac{2}{r^2} \frac{\partial u_\theta}{\partial \theta} + \frac{\partial^2 u_r}{\partial z^2} \right] \end{split}$$

For θ - direction:

$$\begin{split} p\left(\frac{\partial u_{\theta}}{\partial t} + u_{r}\frac{\partial u_{\theta}}{\partial r} + \frac{u_{\theta}}{r}\frac{\partial u_{\theta}}{\partial \theta} + \frac{u_{\theta}u_{r}}{r} + u_{z}\frac{\partial u_{\theta}}{\partial z}\right) \\ &= -\frac{1}{r}\frac{\partial P}{\partial \theta} + pg_{\theta} \\ &+ \mu\left[\frac{1}{r}\frac{\partial}{\partial r}\left(r\frac{\partial u_{\theta}}{\partial r}\right) - \frac{u_{\theta}}{r^{2}} + \frac{1}{r^{2}}\frac{\partial^{2}u_{\theta}}{\partial \theta^{2}} + \frac{2}{r^{2}}\frac{\partial u_{r}}{\partial \theta} + \frac{\partial^{2}u_{\theta}}{\partial z^{2}}\right] \end{split}$$

For z-direction:

$$\begin{split} p\left(\frac{\partial u_z}{\partial t} + u_r \frac{\partial u_z}{\partial r} + \frac{u_\theta}{r} \frac{\partial u_z}{\partial \theta} + u_z \frac{\partial u_z}{\partial z}\right) \\ &= -\frac{\partial P}{\partial z} + p g_z + \mu \left[\frac{1}{r} \frac{\partial}{\partial r} \left(r \frac{\partial u_z}{\partial r}\right) + \frac{1}{r^2} \frac{\partial^2 u_z}{\partial \theta^2} + \frac{\partial^2 u_z}{\partial z^2}\right] \end{split}$$

Energy equation:

$$\frac{\partial T}{\partial t} + u_r \frac{\partial T}{\partial r} + \frac{u_\theta}{r} \frac{\partial T}{\partial \theta} + u_z \frac{\partial T}{\partial z} = \frac{\dot{q}_g}{c_p} + \alpha \left[\frac{1}{r} \frac{\partial}{\partial r} \left(r \frac{\partial T}{\partial r} \right) + \frac{1}{r^2} \right. \left. \frac{\partial^2 T}{\partial \theta^2} + \frac{\partial^2 T}{\partial z^2} \right] + \frac{\varphi}{p c_p}$$

Reynolds number in determining the velocity of the fluid inside the spiral channel with a circular cross-section;

$$Re = u_0 D_h / v$$

Heat transfer effectiveness (ϵ) is defined as the ratio of the actual heat transfer rate to the maximum possible heat transfer rate.

$$\varepsilon = \frac{\dot{Q}_{act}}{\dot{Q}_{max}} = \frac{Actual\ heat\ trasanfer\ rate}{Maximum\ possible\ heat\ trasner\ rate}$$

Here, \dot{Q}_{act} represents the heat transfer rate of the fluid in the spiral channel along the roller wall, and is calculated as follows:

$$\dot{Q}_{act} = \dot{m}c_p(T_{in} - T_{out})$$

The maximum heat transfer represents the highest possible heat transfer rate that can be transferred to the fluid and is equal to the value defined as the constant heat flux.

The boundary conditions of the numerical model are defined to accurately represent the physical conditions of the system. A constant heat flux of 50,000 W/m² is applied to the outer surface of the rotating roller to simulate the thermal energy input. The working fluid, pure water, enters the spiral channels with an inlet temperature of 15°C and a specified velocity based on the Reynolds number. At the fluid inlet, the velocity components are set as U=0, V=0, and W=W_{in}, while the temperature is defined as T=T_{in}. At the fluid outlet, the velocity and temperature gradients along the axial direction are assumed to be zero, expressed as $\partial U/\partial x=0$, $\partial V/\partial x=0$, $\partial W/\partial x=0$, and $\partial T/\partial x=0$. For the roller surface, no-slip conditions are imposed with U=0, V=0, and W=W_{body}, while the thermal boundary condition is represented as $\partial T/\partial z=0$. Additionally, the roller's rotational motion is incorporated into the model to account for its effect on fluid dynamics and heat transfer performance. These boundary conditions ensure an accurate numerical representation of the flow and thermal characteristics inside the rotating industrial roller.

Grid Independence Study of the Numerical Model

Different grid models were generated to ensure the independence of the numerical model from the mesh structure. Although variations in the outlet temperature were observed as the cell density increased, these differences became negligible from the latest models onward. This indicates that the numerical model has achieved grid independence. Consequently, transitioning to models with a higher number of elements was deemed unnecessary as it would only prolong the computation time.

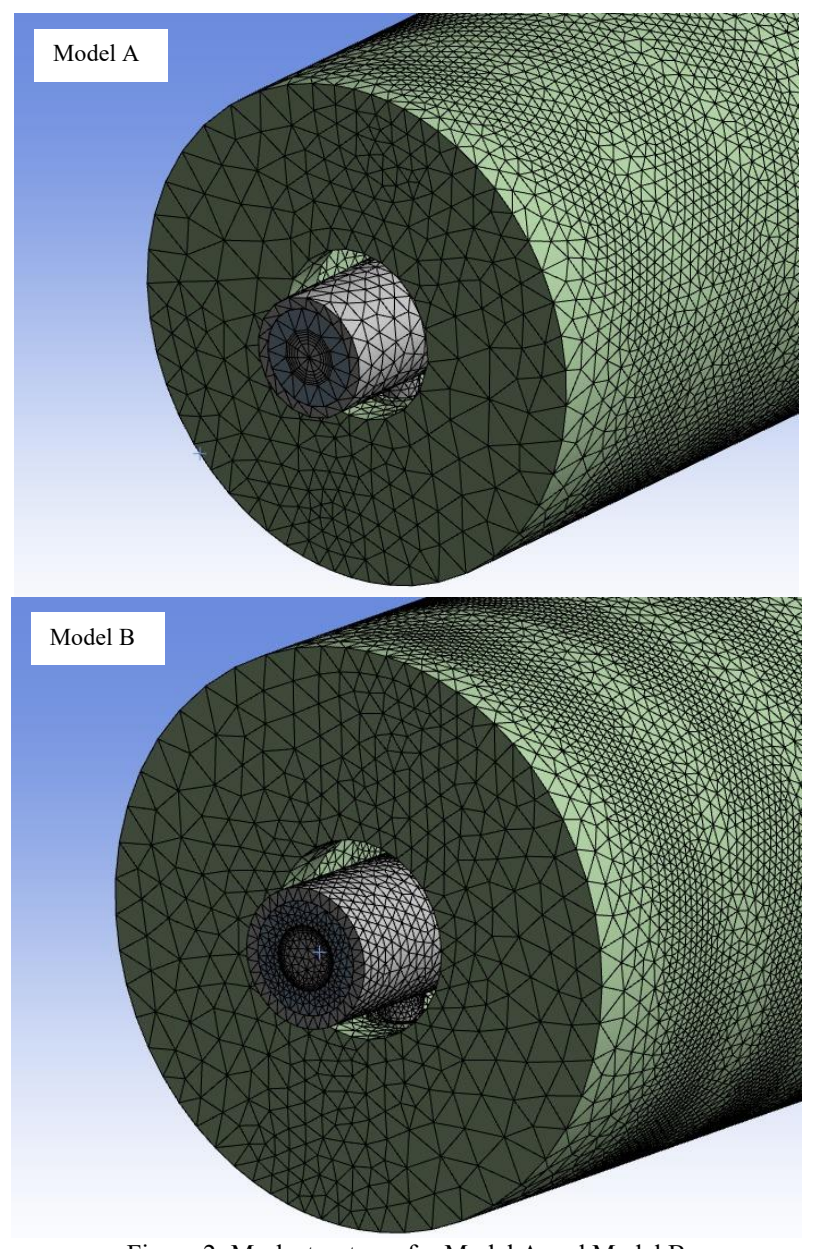


Figure 2: Mesh structures for Model A and Model B

The cells in the mesh structure of the numerical model were refined at the solid-liquid interface to enhance computational accuracy. The mesh structures for two different models are presented in Figure 2. The relationship between the number of cells and the outlet temperature of the working fluid is shown in Figure 3.

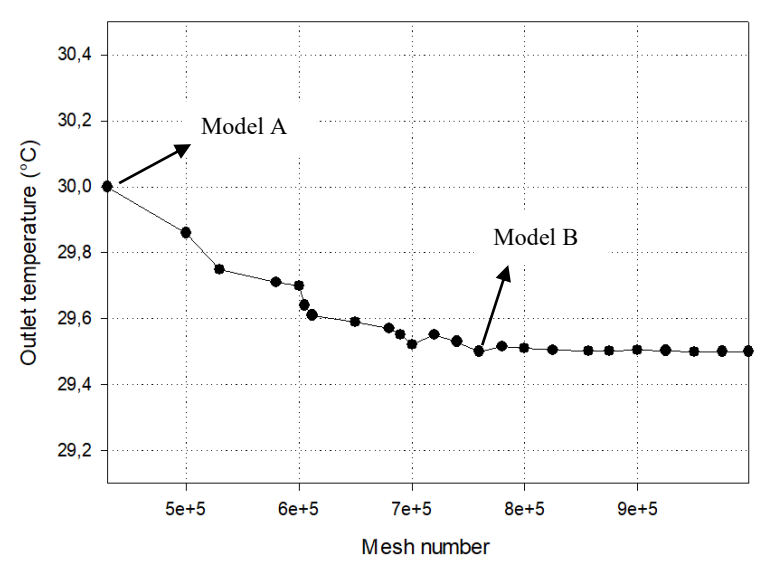


Figure 3: Outlet temperature variation with different mesh number

As seen from the figure, increasing the number of mesh elements initially results in a noticeable decrease in the fluid outlet temperature. However, after approximately 750,000 elements, the variation in outlet temperature becomes negligible, indicating that further refinement does not significantly affect the numerical accuracy.

Iteration Independence Study of the Numerical Model

To ensure the independence of the numerical model from the number of iterations, the error rates calculated in the continuity, momentum, turbulence, and energy equations must approach the predefined limits. The graph illustrating the convergence process of the residual values of these equations is presented in Figure 4.

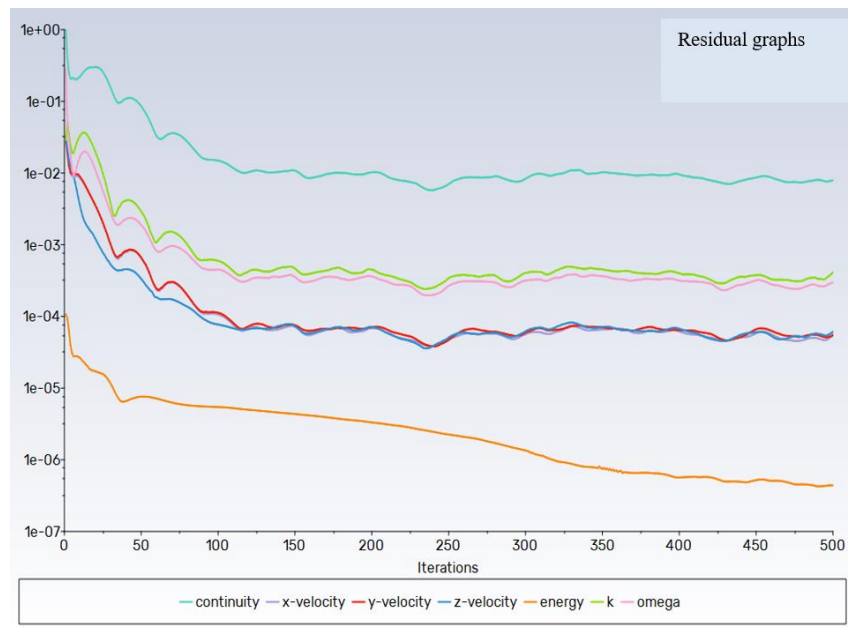


Figure 4: Iteration test for numerical calculations

It can be observed from the residual graphs that the residual values exhibit a rapid and significant decrease during the initial phase of the simulation, indicating effective convergence at an early stage. After this initial period, the residuals begin to stabilize and remain relatively constant for the remainder of the simulation process. This behavior indicates that most numerical corrections and adjustments occur early, after which the solution reaches a stable state with minimal variations. The stabilized residuals suggest that further iterations do not produce substantial changes, confirming that the numerical solution has converged and providing confidence in the reliability and accuracy of the simulation results.

RESULTS AND DISCUSSION

In this study, a new roller design was created using ANSYS Fluent software, and the effects of roller rotational velocity (n = 0, 30, 60, 90 rpm), Reynolds number based on fluid velocity (Re = 4000, 6000, 8000, 10000), and spiral channel pitch (L = 15, 18, 27, 36 mm) on heat transfer performance and temperature distribution were numerically investigated.

Effect of Rotational Velocity

To investigate the effect of the rotational velocity of the roller, the velocity gradually increased at a constant Reynolds number and specific spiral channel spacings. For Re=4000 and a spiral channel pitch of L=15

mm, increasing the rotational velocity from n=0 to 90 rpm resulted in a 12.8% increase in heat transfer effectiveness. When this effect was examined for Re = 10000, a 12.3% increase in heat transfer effectiveness was observed. The impact of increasing rotational velocity on heat transfer performance is presented in Figure 5.

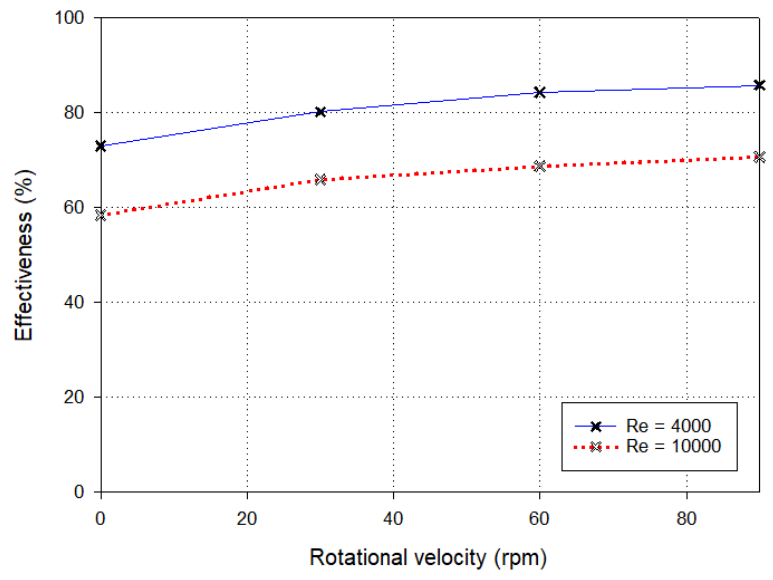


Figure 5: The effect of rotational velocity on effectiveness for L = 15 mm

At the higher rotational velocity (n = 90 rpm), a noticeable temperature gradient and local hot spots are observed, particularly near the fluid outlet region as can be observed in Figure 6. This behavior occurs due to increased turbulence intensity and enhanced mixing at higher rotational velocities, disrupting the thermal boundary layer and intensifying local convective heat transfer.

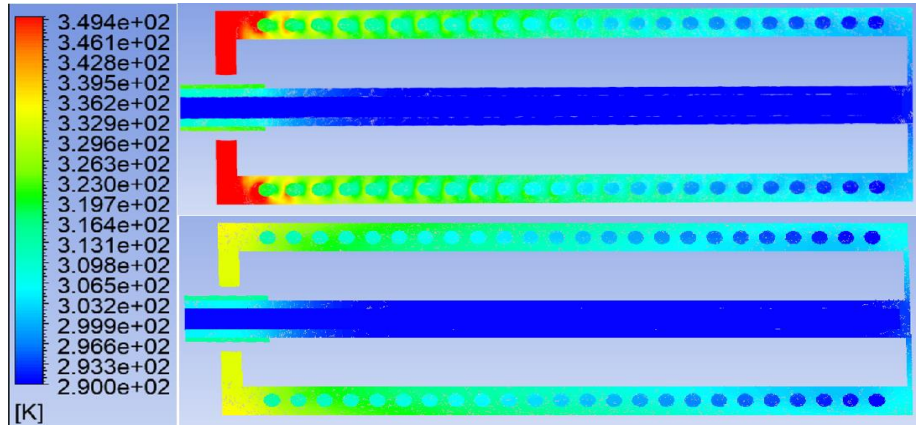


Figure 6: Temperature contours for n = 90 rpm (upper) and n = 30 rpm (Re = 4000 and L = 15 mm)

Although this turbulence-driven effect significantly enhances the overall heat transfer rate, it can result in less homogeneous surface temperatures, which could potentially impact material thermal stresses or product quality in practical applications. Therefore, optimizing rotational velocity involves balancing improved heat transfer effectiveness against maintaining an acceptably homogeneous temperature distribution. For a constant Re=10000, the effect of different L values on heat transfer performance under increasing rotational velocity is presented in Figure 7.

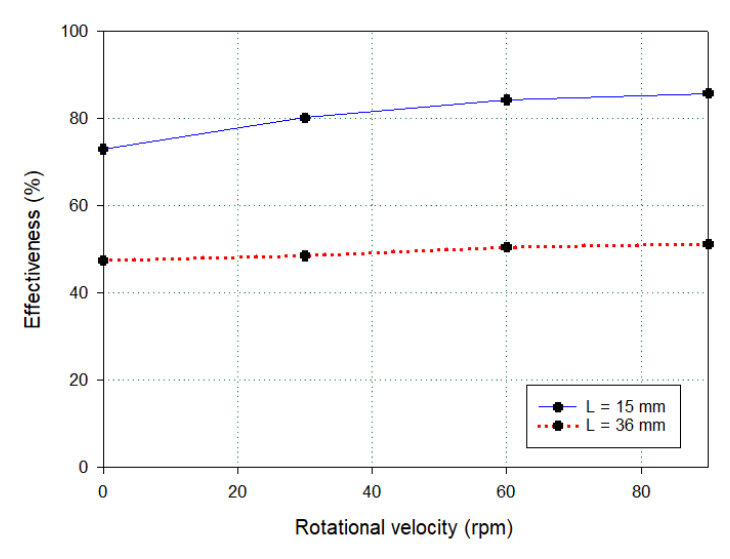


Figure 7: The effect of rotational velocity on effectiveness for Re = 10000

The results indicate that the rotational velocity of the roller enhances heat transfer effectiveness by promoting better fluid mixing and disrupting the thermal boundary layer, leading to improved convective heat transfer. Higher heat transfer performance was observed at lower Reynolds numbers, possibly because, at higher Reynolds numbers, convective heat transfer is already dominant due to increased turbulence, reducing the relative contribution of rotational velocity. Nevertheless, the observed improvements across different Reynolds numbers suggest that incorporating roller rotation is an effective approach for enhancing heat transfer performance in industrial applications.

Effect of Fluid Re Number

For L=15 mm, the Reynolds number was gradually varied to examine its effect on heat transfer performance. When the Reynolds number was reduced from 10000 to 4000 at n=0 rpm, heat transfer effectiveness increased by 14.6%. At n=90 rpm, this increase was observed to be 15.1%.

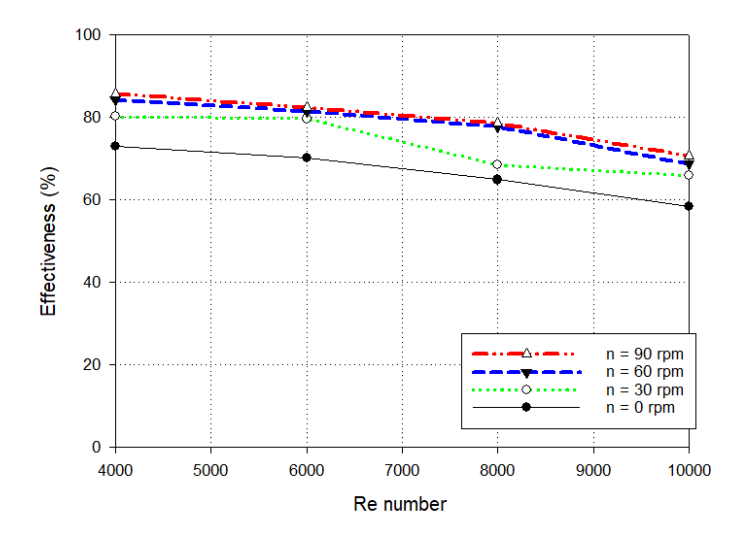


Figure 8: The effect of rotational velocity on effectiveness for Re = 10000

These results indicate that decreasing the Reynolds number enhances heat transfer effectiveness (Figure 8). At lower Reynolds numbers, the flow remains more stable with reduced turbulence intensity, allowing for a more effective interaction between the fluid and the heated surface.

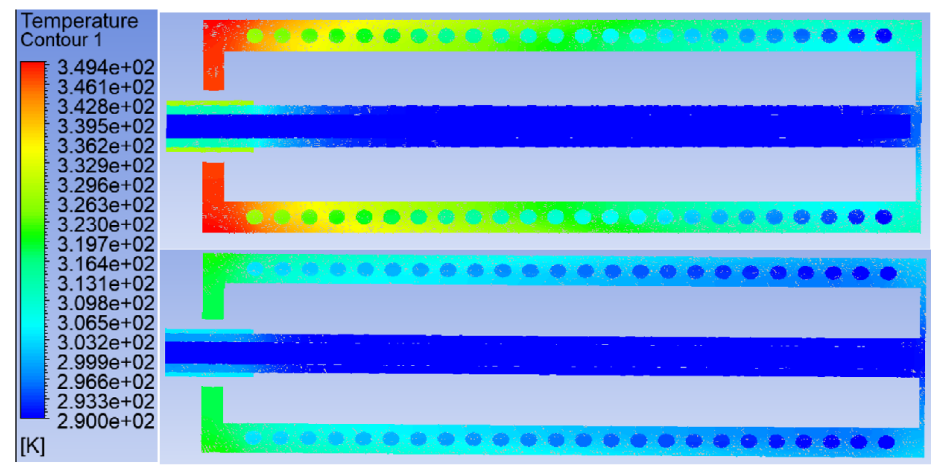


Figure 9: Temperature contours for Re = 4000 (upper) and Re = 10000 (L = 15 mm and n = 90 rpm)

Additionally, at lower velocities, the residence time of the fluid in contact with the roller surface increases, improving thermal energy transfer. The slight increase in effectiveness at n=90 rpm suggests that the combined effect of rotational velocity and reduced Reynolds number further enhances convective heat transfer. This trend highlights the significance of flow characteristics in optimizing heat transfer performance within the system. Temperature contours for Re=4000 and Re=10000 are presented in Figure 9.

Effect of Groove Spacing

To investigate the effect of groove spacing on heat transfer performance, the spacing (L) was gradually reduced at a constant Reynolds number (Re = 4000) and different rotational velocities. For n=0 rpm, decreasing the groove spacing from L=36 mm to L=15 mm resulted in a 5.0% increase in heat transfer effectiveness. At n=30 rpm, the same reduction in L led to an 12.8% increase in effectiveness. When this effect was examined for n=60 rpm, the increase in effectiveness was 18.2%, while at n=90 rpm, the improvement reached 24.0%. The impact of decreasing groove spacing on heat transfer performance is presented in Figure 10.

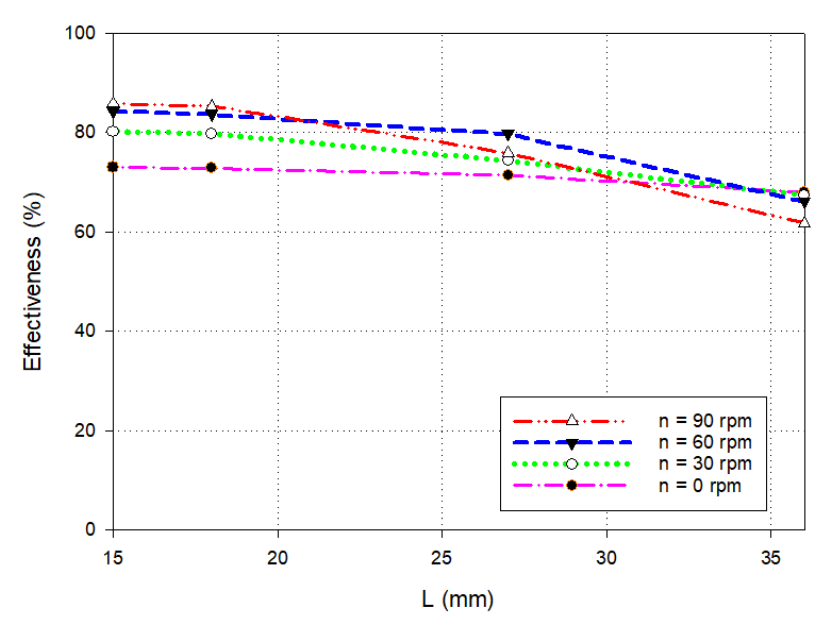


Figure 10: Effect of increasing groove spacing on heat transfer performance

The results indicate that reducing the groove spacing enhances heat transfer effectiveness by increasing the interaction between the working fluid and the heated roller surface. As L decreases, the fluid flow remains in longer contact with the heat source, allowing for more efficient convective heat transfer. Temperature contours for L=15~mm and L=36~mm are presented in Figure 11.

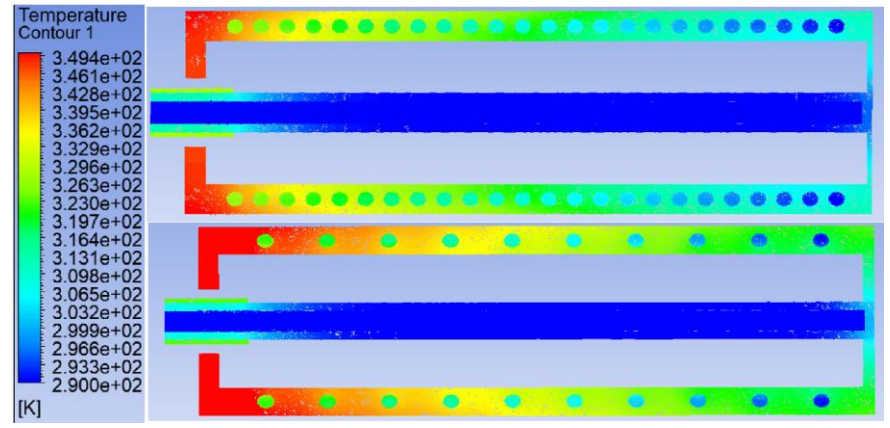


Figure 11: Temperature contours L=15 mm (upper) and L=36 mm (Re = 4000 and n=90 rpm)

The effect becomes more pronounced at higher rotational velocities, where the combination of rotational motion and reduced groove spacing further disrupts the thermal boundary layer and improves mixing. At higher rotational velocities, this interaction strengthens, leading to a more significant improvement in heat transfer performance. However, the effectiveness gain diminishes as L approaches its smallest value, suggesting a potential limit to further enhancements. Nevertheless, the findings confirm that optimizing groove spacing, particularly in combination with rotational velocity, can significantly enhance heat transfer performance in industrial applications. When groove spacing is increased, particularly from L = 30mm onward, the rotational velocity of the roller negatively affects the fluid velocity inside the channels, causing reverse flow phenomena. This leads to a reduction in heat transfer effectiveness. The occurrence of reverse flow at larger groove spacings suggests that careful optimization is necessary to balance the roller's rotational velocity with groove spacing, ensuring stable fluid flow and optimal thermal performance.

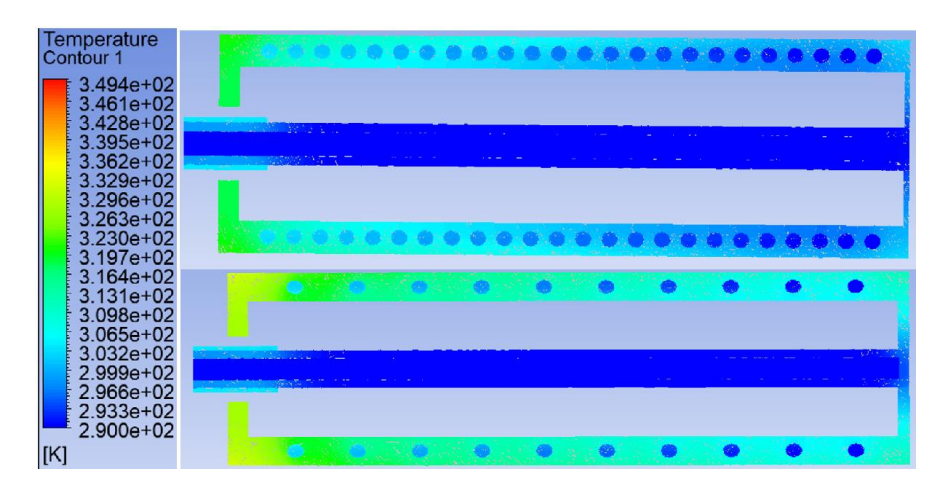


Figure 12: Temperature contours L = 15 mm (upper) and L = 36 mm (Re = 10000 and n = 90 rpm)

When examining the temperature contours, it can be observed that for the case of $L=36\,$ mm, where the groove spacing is larger, the surface temperature distribution is more homogeneous. However, due to the smaller difference between fluid inlet and outlet temperatures, the heat transfer rate decreases. This effect is presented in Figure 12 for Re = 10000, showing that a more homogeneous surface temperature distribution is obtained as a result of the reduction in the thermal boundary layer thickness.

CONCLUSION

In this study, the effects of different parameters on the heat transfer performance and temperature distribution in a rotating industrial roller with a novel spiral groove design were investigated numerically. The investigated parameters are the rotational velocity of the roller ranging from 0 to 90 rpm, Reynolds number ranging from 4000 to 10000, and spiral groove spacing ranging from 15 mm to 36 mm. In conclusion;

- 1. Increasing the rotational velocity of the roller from 0 to 90 rpm significantly enhanced the heat transfer effectiveness, with improvements of 12.8% at Re = 4000 and 12.3% at Re = 10000, indicating the beneficial role of roller rotation in heat transfer enhancement.
- 2. Reducing the Reynolds number from 10000 to 4000 resulted in an increase in heat transfer effectiveness of 14.6% at n = 0 rpm and 15.1% at n = 90 rpm for a spiral channel pitch of L = 15 mm. These findings suggest that lower Reynolds numbers contribute positively to heat transfer performance due to increased fluid stability and longer residence times, enabling better thermal interaction between the fluid and roller surface.
- 3. Reducing the groove spacing (L) from 36 mm to 15 mm at a constant Reynolds number (Re = 4000) resulted in enhanced heat transfer effectiveness, with observed improvements of 5.0% at n = 0 rpm, 12.8% at n = 30 rpm, 18.2% at n = 60 rpm, and 24.0% at n = 90 rpm. These findings clearly demonstrate that smaller groove spacings significantly improve heat transfer performance by prolonging fluid interaction with the heated roller surface, thereby enhancing convective heat transfer.
- 4. It was determined that the results of this study could provide significant benefits in industrial applications. Due to decreased fluid consumption resulting from enhanced heat transfer performance, more economical and environmentally friendly systems can be developed. Additionally, energy-efficient systems can be achieved through reduced energy consumption. Furthermore, optimizing heat transfer performance through the identified parameters could improve product quality while reducing operational costs.
- 5. For future studies, the use of nanofluids and hybrid nanofluids in rotating industrial rollers could significantly improve heat transfer performance due to their enhanced thermal properties. Additionally, further investigations on different spiral groove geometries and configurations might provide better control over fluid flow, potentially improving temperature uniformity and

overall thermal efficiency. Exploring these areas would not only enhance system performance but also offer broader opportunities for optimizing industrial processes in terms of energy savings, economic benefits, and environmental sustainability.

ABBREVIATIONS

CFD Plate heat exchangers
NTU Number of transfer unit
Re Reynolds number

CAE Computer aided engineering

HVAC Heating, ventilation, and air conditioning

EG Ethylene glycol
DI Deionized water

MWCNT Multi-walled carbon nanotubes
ATF Automatic transmission fluid

REFERENCE

- Alam, M. M. (2022). A review of cylinder corner effect on flow and heat transfer. Journal of Wind Engineering and Industrial Aerodynamics, 229, 105132.
- Yurtseven, A. (2021). Isi Transfer Silindirlerinde Halka Akış Kanalı Geometrisinin Isil Performansa Etkisinin Sayısal Olarak İncelenmesi. Avrupa Bilim ve Teknoloji Dergisi, (23), 552-562.
- Baghel, K., (2020) "Heat transfer characteristics of free surface water jet impingement on a curved surface", International Journal of Heat and Mass Transfer, 2020, 164: 120487.
- Berni, F., Cicalese, G., Borghi, M., & Fontanesi, S. (2021). Towards grid-independent 3D-CFD wall-function-based heat transfer models for complex industrial flows with focus on in-cylinder simulations. Applied Thermal Engineering, 190, 116838.
- C. Du, L. Li, and X. Fan, (2017) "Numerical study on vortex cooling flow and heat transfer behavior under rotating conditions," Int J Heat Mass Transf, vol. 105, pp. 638–647, Feb. 2017, doi: 10.1016/j.ijheatmasstransfer.2016.10.028.
- Fénot, M., Bertin, Y., Dorignac, E., & Lalizel, G. (2011). A review of heat transfer between concentric rotating cylinders with or without axial flow. International journal of thermal sciences, 50(7), 1138-1155.
- Güneş, T., Şahin, M., & Kılıç, M. (2023). Investigation of the effect of different parameters of phase change materials on heat exchanger performance. Cukurova Üniversitesi Mühendislik Fakültesi Dergisi, 38(4), 1117-1128.
- I. Dalgıç, N. Tokgöz, and C. Özalp, (2021) "Açık bir kavite içinde dönen silindirle aktif akış kontrolü: 1s1 transferi ve akış özelliklerinin sayısal incelenmesi," Mühendislik Bilimleri ve Tasarım Dergisi, vol. 9, no. 4, pp. 1348–1371, Dec. 2021, doi: 10.21923/jesd.949998.
- Jahedi, M., Moshfegh, B., (2019) "Quenching a rotary hollow cylinder by multiple configurations of water-impinging jets", International Journal of Heat and Mass Transfer, 2019, 137: 124-37.

- J. Luo, S. Y. Wu, L. Xiao, and Z. L. Chen, (2021) "Hydrodynamics and heat transfer of multiple droplets successively impacting on cylindrical surface," Int J Heat Mass Transf, vol. 180, Dec. 2021, doi: 10.1016/j.ijheatmasstransfer.2021.121749.
- Kılıç, M., Şahin, M., Demircan, T., Kilinc, Z., & Ullah, A. (2023). Numerical investigation of cooling an industrial roller by using swirling jets. El-Cezeri, 10(1), 147-159.
- Liu, Y. Q., Sen, L. U., Zheng, B., & Peng, S. U. N. (2017). Numerical Simulation of Heat Transfer from Rotary Cylinder by Spray Cooling. Materials Science, 23(4), 411-415.
- M. Hamraoui, (2009) "Thermal behaviour of rollers during the rolling process," Appl Therm Eng, vol. 29, no. 11–12, pp. 2386–2390, 2009, doi: 10.1016/j.applthermaleng.2008.12.013.
- Selimefendigil, F., Öztop, H., (2018) "Analysis and predictive modeling of nanofluid-jet impingement cooling of an isothermal surface under the influence of a rotating cylinder", International Journal of Heat and Mass Transfer, 2018, 121: 233-245.
- Tachibana, F., Fukui, S., & MITSUMURA, H. (1960). Heat transfer in an annulus with an inner rotating cylinder. Bulletin of JSME, 3(9), 119-123.
- Ullah, A., Kilic, M., Habib, G., Sahin, M., Khalid, R. Z., & Sanaullah, K. (2023). Reliable prediction of thermophysical properties of nanofluids for enhanced heat transfer in process industry: a perspective on bridging the gap between experiments, CFD and machine learning. Journal of Thermal Analysis and Calorimetry, 148(12), 5859-5881.
- X. Zhao, Z. Yin, B. Zhang, and Z. Yang, (2020) "Experimental investigation of surface temperature non-uniformity in spray cooling," Int J Heat Mass Transf, vol. 146, Jan. 2020, doi: 10.1016/j.ijheatmasstransfer.2019.118819.

An Investigation on Design Criteria of Heat Exchangers by Using Tree Models of Machine Learning Methods

Mahir ŞAHİN¹

Mustafa KILIÇ²

Merve ALA³

¹⁻ Res. Asst.; Adana Alparslan Türkeş Bilim ve Teknoloji Üniversitesi Makine Mühendisliği Bölümü. msahin@atu.edu.tr ORCID No: 0000-0002-9565-9160

²⁻ Prof. Dr.; Adana Alparslan Türkeş Bilim ve Teknoloji Üniversitesi Makine Mühendisliği Bölümü. mkilic@atu.edu.tr ORCID No: 0000-0002-8006-149X

³⁻ Adana Alparslan Türkeş Bilim ve Teknoloji Üniversitesi Makine Mühendisliği Bölümü. merveala01@gmail.com ORCID No: 0009-0001-4045-5267

ABSTRACT

This study examines the use of tree-based machine learning models, including Random Forest, AdaBoost, and XGBoost, for the analysis and optimization of heat exchanger design parameters. Each model is evaluated according to its predictive accuracy and compatibility with different data conditions to determine its effectiveness for specific design criteria. The results indicate that XGBoost performs well in predicting parameters such as heat transfer rate, safety, and reliability when large datasets are available. AdaBoost is more suitable for cases involving limited data, particularly for predicting exchanger type and ease of maintenance. Random Forest provides consistent results in estimating cost and pumping power. Additionally, the study categorizes design parameters based on data volume and accuracy requirements, offering guidance for appropriate model selection. The integration of these models supports improved energy efficiency, early fault detection, and reduced operational costs. Their use in the early stages of design can contribute to the development of more reliable, efficient, and sustainable heat exchanger systems, with future potential to incorporate advanced materials and innovative cooling fluids.

Keywords – Heat exchangers, machine learning, tree models, design criteria.

INTRODUCTION

Heat exchangers are essential engineering systems designed to facilitate the transfer of thermal energy between two fluid streams. They are extensively employed across a wide range of industries, including aerospace, petrochemical, and automotive sectors (Ghajar and Cengel, 2021:874). The selection and design of heat exchangers for these applications are primarily influenced by critical parameters such as heat transfer coefficient, material properties, physical dimensions, and overall weight (Jradi et al., 2022:1514).

Recent advancements in unmanned aerial vehicle (UAV) research have increasingly focused on developing solutions that achieve both weight reduction and improved cooling efficiency in heat exchangers. Particularly in high-altitude applications, the emergence of technologies such as electric motor cooling systems, lightweight thermal batteries, and the use of phase change materials has substantially influenced the design requirements of heat exchangers (Kilic et al., 2024:10973), (Wang et al., 2023:233726), (Koca et al., 2023:1366). During the heat exchanger design process for an unmanned aerial vehicle, several factors come into play, including geometric constraints, battery thermal management, limited available space, weight restrictions, and the need for efficient heat dissipation under varying flight conditions. These considerations collectively shape the thermal system architecture and directly impact the overall performance and reliability of the

UAV (Alexiou et al., 2021:12038), (Son et al., 2023:120186). Traditional data-driven approaches such as linear and polynomial regression are generally suited for limited datasets and a small number of input parameters. In contrast, machine learning models offer enhanced capabilities for performance analysis of heat exchangers by effectively supporting tasks such as regression, classification, and correlation analysis.

Supervised learning methods are utilized for various purposes in different types of heat exchangers, depending on factors such as computational efficiency, physical adaptability, and performance evaluation criteria (Sammil and Sridharan, 2024:102337). Techniques such as Support Vector Classification (SVC), Gaussian Process Regression, Extreme Gradient Boosting (XGBoost), Radial Basis Function Networks (RBFN), Light Gradient Boosting Machine (LightGBM), and Artificial Neural Networks (ANN) represent submodels from different categories within the domain of supervised learning (Luo and Li., 2023:2).

ANN have demonstrated accurate and practical results in a range of applications related to unmanned aerial vehicles (Abbaspour et al., 2020:3401). These include the prediction and identification of nonlinear system behavior in control design, performance estimation of propulsion systems, and the evaluation of key performance parameters (Thanikodi et al., 2020:2), (Isik et al., 2020:1177). Additionally, ANN models have proven effective in assessing the thermal durability and reliability of heat exchanger systems used in UAV platforms (Khan et al., 2022:119135). SVC is frequently employed in UAV systems for modeling and simulating the performance of heat exchangers. Moreover, when integrated with hybrid modeling approaches, SVC facilitates precise enhancements in the prediction and optimization of thermo-hydraulic performance parameters, particularly in numerical analyses involving delta winglet configurations (Muthukrishnan et al., 2020:499), (Ekrani et al., 2023:108141). Gaussian Process Regression (GPR) has proven effective in the performance optimization of various types of heat exchangers, including those equipped with helical wire turbulators. It also enables precise prediction of thermodynamic properties and vaporliquid equilibrium behavior in propulsion and power generation systems, contributing to improved system design and operational reliability (Celik et al., 2023:108439), (Zhou et al., 2023:124888). Extreme Gradient Boosting (XGBoost) can be effectively utilized for modeling and simulating complex processes such as surface roughness. Owing to its high accuracy and computational efficiency, it is particularly well-suited for predicting key thermal parameters, including the heat transfer coefficient (Shaeri et al.,). XGBoost is capable of capturing complex relationships within datasets, making it a powerful tool for evaluating the effects of various nanofluids on heat transfer. Its ability to handle nonlinear interactions allows for accurate predictions in thermofluid analysis involving advanced working fluids (Godasiaei and Chamkha, 2024:1). The Radial Basis Function Network (RBFN) model demonstrates strong predictive performance in accurately estimating fouling resistance in heat exchanger data. Its capability to handle nonlinear patterns makes it a reliable tool for analyzing thermal degradation phenomena in heat transfer systems (Ikram et al., 2024:253). The Light Gradient Boosting Machine (LightGBM) model offers an effective strategy for predicting heating and cooling loads in buildings, particularly during the early design stages. Its predictive capabilities enable the implementation of improved energy efficiency measures, contributing to more sustainable thermal management solutions (Panda et al., 2023:322036).

A comprehensive review of the existing literature indicates that machine learning applications in heat exchanger studies generally fall into two main categories: those addressing fluid-related parameters (such as hot and cold fluid properties) and those focusing on flow characteristics and geometric configurations. However, a gap remains in the literature regarding the application of machine learning techniques specifically tailored to heat exchanger design criteria. Addressing this gap, the present study explores the use of machine learning methods across various types of heat exchangers, with a particular emphasis on evaluating and comparing these methods in terms of their relevance to design parameters. The study is structured into three principal sections. The first section introduces a foundational overview and classification of machine learning techniques, highlighting their roles in heat exchanger applications. The second section delves into the critical factors that influence model selection, supported by tabulated data identifying variables that impact model performance across different exchanger types. The final section offers recommendations for improving the integration of machine learning into heat exchanger design, informed by both current literature and prospects for future research.

MATERIALS AND METHODS

Machine Learning Models

Machine learning techniques are typically divided into five major categories: supervised learning, unsupervised learning, reinforcement learning, deep learning, and hybrid learning. Among these, models such as AdaBoost, Random Forest (RF), and Extreme Gradient Boosting (XGBoost) fall under the class of tree-based algorithms, as illustrated in Figure 1.

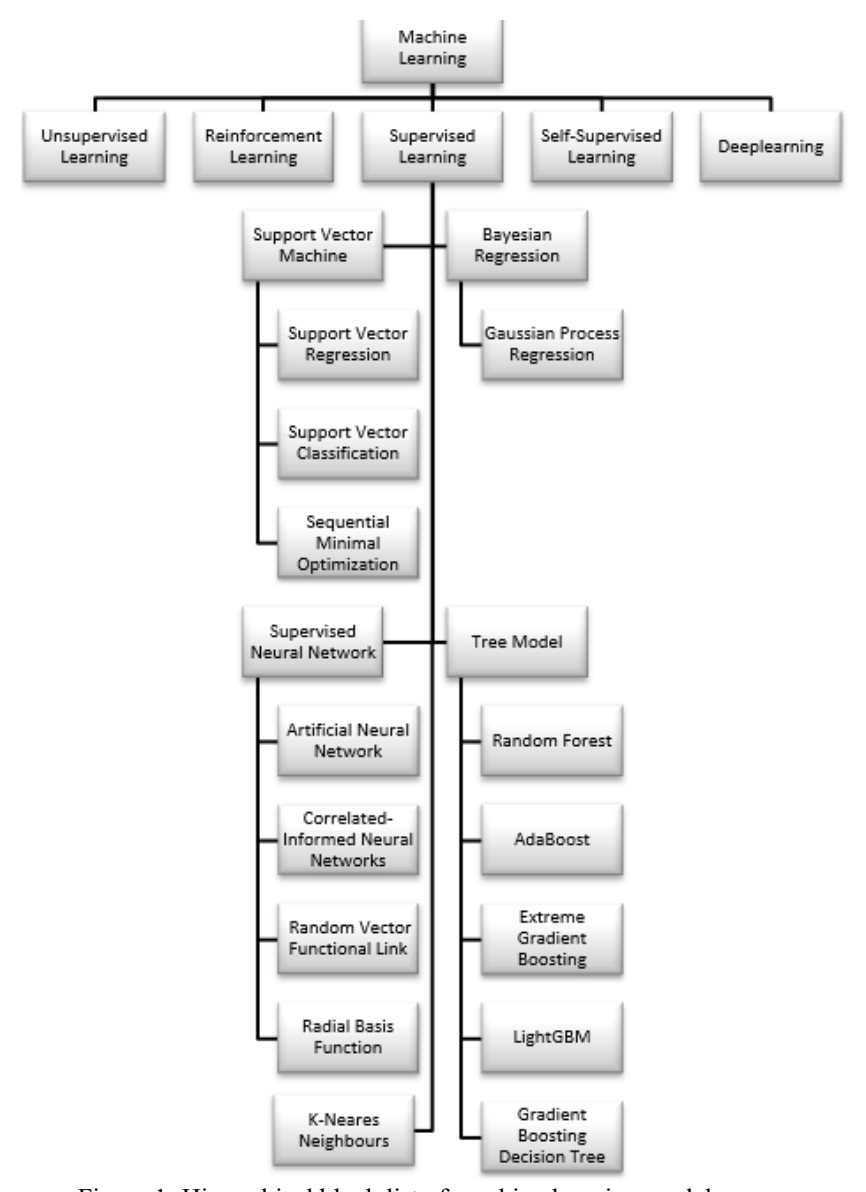


Figure 1: Hierarchical block list of machine learning models

As presented in Table 1, XGBoost, AdaBoost, and Random Forest share certain structural similarities while also differing in their algorithmic frameworks and application purposes. Random Forest operates by aggregating the outcomes of multiple decision trees, each constructed from a randomly drawn subset of the training data using the bootstrap method. This ensemble strategy enhances the robustness and accuracy of the predictions. AdaBoost, on the other hand, is an ensemble learning technique that iteratively adjusts the weights of misclassified samples, learning from

previous errors to build a more accurate model. It combines multiple weak learners by assigning greater importance to those with higher predictive accuracy, ultimately forming a strong composite classifier. methodology not only improves prediction performance but also contributes to enhanced computational efficiency (Freund and Schapire, 1996:148), (Giorgio et al., 2023:620). XGBoost, in contrast, constructs its predictive framework using decision trees that iteratively partition the dataset into smaller, more homogeneous segments. The model's performance is evaluated using an objective function, which commonly involves the mean squared error for regression tasks and the logarithmic loss function for classification problems. This structure enables XGBoost to effectively handle complex nonlinear relationships while maintaining computational efficiency (Chen and Guestrin, 2016:785).

Overall, while machine learning models offer significant advantages in terms of reduced computational burden and improved time efficiency, their true potential lies in their ability to be tailored and applied more effectively to specific problem domains.

Table 1: Compression of tree learning methods.

Machine Learning Approaches	Output Type	Algorithm Type	Purpose of Use
Random Forest	Classification/ Regression	Bagging	Medium or big sized datasets
AdaBoost	Classification/ Regression/	Boosting	Small or medium sized datasets, more focus on misclassified samples
XGBoost	Classification/ Regression/Ran king	Gradient Boosting	Big data sets, Complex problems, Prevent overfitting

RESULTS AND DISCUSSION

This section provides a review of existing research concerning the use of machine learning models in determining design criteria for heat exchangers. Various tree-based algorithms are assessed across datasets of differing sizes and evaluated using performance metrics such as Root Mean Square Error (RMSE), Mean Absolute Error (MAE), and the coefficient of

determination (R²). Among the influencing factors, dataset size is identified as the most significant determinant in the selection of suitable tree-based models. The literature reveals that such models are extensively applied in domains including energy consumption forecasting, fault detection, estimation of thermophysical properties, and design optimization. Additionally, it has been observed that tree-based models can be combined with other machine learning techniques to develop hybrid frameworks that offer enhanced predictive accuracy.

Heat Transfer Rate

The heat transfer rate is one of the primary criteria influencing the selection of heat exchangers. Machine learning techniques such as General Regression Neural Networks (GRNN), Random Forest (RF), Extreme Gradient Boosting (XGBoost), and AdaBoost have shown strong capabilities in accurately predicting heat transfer coefficients on internal surfaces, including plates and tubes. These data-driven methods not only enhance predictive accuracy but also offer robust generalization, resulting in significant reductions in design optimization costs and considerable time savings during the selection process. Comparative analyses indicate that AdaBoost performs well in generating convergent predictions even with relatively small datasets; however, it tends to yield higher mean absolute error (MAE) values relative to other algorithms. In contrast, XGBoost consistently delivers higher accuracy in larger datasets, exhibiting superior overall predictive performance across a range of evaluation metrics.

Size and Weight

The compact and lightweight nature of heat exchangers significantly increase their suitability for use in sectors such as aerospace and automotive, where space and mass limitations are critical. The materials used for both the structure and working fluid, as well as complex geometries that affect the surface area-to-volume ratio, directly influence these design constraints. In this context, the XGBoost algorithm integrated with autoencoders has shown strong predictive accuracy based on RMSE, MAE, and R² metrics. Additionally, when combined with hybrid modeling approaches, it enables precise estimation of key design parameters such as the number of transfer units, which are essential for optimizing the dimensions and weight of heat exchangers.

Cost

Budget limitations represent a fundamental consideration in the selection of heat exchangers. Key factors such as the type of working fluid,

material selection, design specifications, and application domains have a direct influence on overall costs. The Random Forest algorithm contributes to cost efficiency by accurately predicting fouling accumulation, pressure, and temperature in medium-to-large datasets, thereby supporting performance optimization. Similarly, the AdaBoost algorithm enhances fault detection capabilities in heat exchangers using small-to-medium datasets, and the resulting improvements in operational efficiency have a direct impact on reducing system-related expenditures.

Pumping Power

Temperature, flow rate, and system pressure are among the most influential parameters determining pump power requirements. The Random Forest algorithm has shown strong predictive performance in estimating essential heat pump characteristics, including heating capacity, efficiency, thermal behavior, and power consumption. By effectively capturing the complex interactions among operational variables, this method offers a reliable alternative to traditional modeling approaches, combining high accuracy with improved computational efficiency.

Type of Heat Exchanger

Shell-and-tube, compact, double-pipe, plate-and-frame, and regenerative heat exchangers are among the most commonly utilized types in industry, with their selection guided by factors such as fluid thermophysical properties, operating pressure and temperature ranges, and overall system design constraints. The AdaBoost algorithm has proven effective in predicting key thermophysical parameters and the Number of Transfer Units (NTU), which is closely associated with exchanger size and weight, based on data derived from computational fluid dynamics simulations. Its strong predictive capability, particularly in scenarios with limited datasets, offers a valuable advantage for optimizing thermal systems and improving energy efficiency.

Safety and Reliability

Key parameters influencing the safety and reliability of heat exchangers include the toxicity level of the working fluid, sealing integrity, vibration and noise levels, as well as the inlet and outlet fluid temperatures and pressures. The XGBoost algorithm, known for its high accuracy when applied to large datasets, has proven to be an effective tool for fault detection and diagnostic applications. In addition, it provides notable advantages in sustaining the desired thermal comfort conditions within the system.

Ease of Servicing

Heat exchanger design should accommodate in-situ cleaning processes, and the selection of materials should prioritize corrosion-resistant options such as stainless steel or titanium to ensure long-term structural integrity. Moreover, routine maintenance is essential for sustaining operational efficiency and extending system lifespan. The AdaBoost algorithm contributes to overall system optimization by iteratively learning from past prediction errors, thereby improving accuracy on new data. It also facilitates early fault detection through the analysis of corrosion data and provides reliable forecasts of fouling development.

Materials

In material selection for heat exchangers, corrosion resistance, thermal conductivity, and mechanical strength are key criteria that significantly influence performance and durability. As a result, materials such as copper, aluminum, stainless steel, and titanium are commonly utilized. The XGBoost algorithm has proven to be an effective approach for predicting the thermophysical properties of fluids subjected to surface roughness, particularly in estimating parameters like the heat transfer coefficient. Its ability to deliver high accuracy and computational efficiency, even with limited datasets, makes it a valuable tool in material and thermal performance assessments.

Prospects for Tree Models in Heat Exchangers

In general, the utilization of machine learning models in heat exchanger applications for future perspective can be categorized into several key areas:

- Optimization of performance and thermo-hydraulic modeling,
- Development of AI-assisted intelligent heat exchangers,
- Enhancement of energy efficiency and sustainability,
- Estimation of overall heat transfer coefficients,
- Detection and prevention of fouling,
- Prediction of the thermal properties of fluids,
- Fault detection and reliability assessment under variable operating conditions,
- Real-time monitoring and predictive maintenance scheduling,
- Selection of optimal materials and working fluids based on performance criteria,

• Support for geometry design and configuration selection through data-driven approaches.

Tree-based models such as Random Forest, AdaBoost, and XGBoost are increasingly utilized for the analysis and optimization of heat exchanger systems. These algorithms offer considerable potential in predicting not only energy transfer between fluids but also fluid–structure interactions and the thermophysical properties of working fluids. Additionally, they contribute to improved performance efficiency and allow for more accurate modeling of operational conditions. Future advancements are anticipated to involve the integration of these models with complementary techniques to enhance predictive accuracy in solving complex thermal engineering problems.

By leveraging large datasets, optimal correlations between thermal and hydraulic properties can be identified, supporting the design of more efficient heat exchanger configurations. Decision tree-based models enable the analysis of historical performance data to generate predictive insights that support system adaptation under varying environmental and operational conditions. This predictive capability contributes to the long-term enhancement of system efficiency and facilitates more effective energy consumption optimization.

To support fouling detection and prevention, the influence of particle size on heat transfer characteristics can be systematically analyzed using data-driven approaches. This analysis enables the development of more robust fault detection and diagnostic methodologies. As a result, system performance can be optimized, and maintenance operations can be executed more effectively and efficiently, reducing downtime and extending equipment lifespan.

CONCLUSION

In this study, heat exchanger design parameters were analyzed using a range of machine learning techniques, and the most appropriate method was identified for each parameter based on predictive accuracy and computational efficiency. In conclusion, tree-based models such as Random Forest, XGBoost, and AdaBoost have demonstrated strong potential in addressing complex heat exchanger design challenges. Their ability to handle nonlinear relationships, process large datasets, and adapt to varying operational conditions makes them valuable tools for improving performance, enhancing energy efficiency, and supporting intelligent system design. The findings suggest that integrating these models into early design stages and operational strategies can lead to more reliable, cost-effective, and high-performance thermal systems.

1. Considering the varying data density and accuracy requirements associated with tree-based models, it can be concluded that

different heat exchanger design criteria are best addressed under specific application conditions. Design aspects such as heat transfer rate, safety, and reliability are most effectively analyzed in scenarios involving large datasets and high accuracy demands. Pumping power can be reliably assessed in applications with extensive datasets but lower precision requirements. In contrast, cost estimation, heat exchanger type, and material selection are better suited for cases with limited datasets that require high prediction accuracy. Finally, parameters such as ease of maintenance and servicing can be evaluated adequately under conditions involving both low data volume and minimal accuracy requirements.

- 2. The application of tree-based machine learning methods in heat exchanger systems provides substantial advantages in enhancing energy efficiency, enabling early fault detection, streamlining maintenance operations, and minimizing operational costs. By optimizing system performance, these methods contribute to longterm improvements in both sustainability and overall operational effectiveness.
- 3. Looking ahead, the integration of tree-based machine learning models into industrial applications is expected to play a critical role in optimizing heat exchanger design parameters, leading to the development of more efficient thermal systems. These advancements may also accelerate the adoption of novel materials and cooling fluids, such as metamaterials and nanofluids, while supporting the design and manufacturing of heat exchangers that are cost-effective, reliable, easy to maintain, and environmentally sustainable.

ABBREVIATONS

ANN Artificial neural network
CFD Computational fluid dynamics
CNN Convolutional neural networks

DC District cooling
DT Decision tree
KNN K-nearest neighbor
MLP Multilayer perceptron

Greek letters

- ε Heat transfer effectiveness
- ρ Fluid density (kgm⁻³)
- μ Dynamic viscosity (kgm⁻¹s⁻¹)

REFERENCE

- A. Ghajar and Y. Cengel, Heat and Mass Transfer Fundamentals and Applications, 6th Edition, McGraw-Hill Education, New York, NY, 2020. 2021.
- A. Abbaspour, K. K. Yen, P. Forouzannezhad, and A. Sargolzaei, "A Neural Adaptive Approach for Active Fault-Tolerant Control Design in UAV," IEEE Trans Syst Man Cybern Syst, vol. 50, no. 9, pp. 3401–3411, Sep. 2020, doi: 10.1109/TSMC.2018.2850701.
- A. de Giorgio, G. Cola, and L. Wang, "Systematic review of class imbalance problems in manufacturing," Dec. 01, 2023, Elsevier B.V. doi: 10.1016/j.jmsy.2023.10.014.
- A. Koca, C. İ. Çalışkan, E. Koç, and Ö. Akbal, "A Novel 3D Printed Air-Cooled Fuel Cooler Heat Exchanger for Aviation Industry," Heat Transfer Engineering, vol. 44, no. 15, pp. 1350–1371, Aug. 2023, doi: 10.1080/01457632.2022.2134077.
- E. Alexiou, S. Dimitriou, T. Dimopoulos, D. Paliaikos, P. Panagiotou, and K. Yakinthos, "Cooling system design for the internal combustion engine of a BWB UAV prototype," IOP Conf Ser Mater Sci Eng, vol. 1024, no. 1, p. 012038, Jan. 2021, doi: 10.1088/1757-899X/1024/1/012038.
- G. Işık, S. Ekici, and G. Şahin, "A neural network model for UAV propulsion system," Aircraft Engineering and Aerospace Technology, vol. 92, no. 8, pp. 1177–1184, Aug. 2020, doi: 10.1108/AEAT-04-2020-0064.
- H. Luo and X. Li, "A hybrid model of CNN-BiLSTM and XGBoost for HVAC systems energy consumption prediction," 2023 5th International Conference on Industrial Artificial Intelligence (IAI), pp. 1–6, 2023, doi: 10.1109/IAI59504.2023.10327594.
- J. Guo et al., "Prediction of heating and cooling loads based on light gradient boosting machine algorithms," Build Environ, vol. 236, p. 110252, May 2023, doi: 10.1016/J.BUILDENV.2023.110252.
- J. P. Panda, B. Kumar, A. K. Patil, M. Kumar, and R. Kumar, "Machine learning assisted modeling of thermohydraulic correlations for heat exchangers with twisted tape inserts," Acta Mechanica Sinica/Lixue Xuebao, vol. 39, no. 1, Jan. 2023, doi: 10.1007/s10409-022-22036-x.
- K. Ikram, K. Djilali, D. Abdennasser, R. Al-Sabur, B. Ahmed, and A. N. Sharkawy, "Comparative analysis of fouling resistance prediction in shell and tube heat exchangers using advanced machine learning techniques," Research on Engineering Structures and Materials, vol. 10, no. 1, pp. 253–270, 2024, doi: 10.17515/resm2023.858en0816.
- M. Z. A. Khan, H. A. Khan, and M. Aziz, "Performance optimization of heat-exchanger with delta-wing tape inserts using machine learning," Appl Therm Eng, vol. 216, Nov. 2022, doi: 10.1016/j.applthermaleng.2022.119135.
- M. Kilic, M. Sahin, and A. Abdulvahitoglu, "A new approach for enhancing the effectiveness of a regenerative heat exchanger by using organic and inorganic phase change material," J Therm Anal Calorim, Nov. 2024, doi: 10.1007/s10973-024-13599-2.
- M. Zhou, C. Ni, C. L. Sung, S. Ding, and X. Wang, "Modeling of thermophysical properties and vapor-liquid equilibrium using Gaussian process regression," Int J Heat Mass Transf, vol. 219, Feb. 2024, doi: 10.1016/j.ijheatmasstransfer.2023.124888.

- M. R. Shaeri, M. C. Ellis, and A. M. Randriambololona, "XGBOOST-BASED MODEL FOR PREDICTION OF HEAT TRANSFER COEFFICIENTS IN LIQUID COLD PLATES." [Online]. Available: https://github.com/dmlc/xgboost
- N. Celik, B. Tasar, S. Kapan, and V. Tanyildizi, "Performance optimization of a heat exchanger with coiled-wire turbulator insert by using various machine learning methods," International Journal of Thermal Sciences, vol. 192, Oct. 2023, doi: 10.1016/j.ijthermalsci.2023.108439.
- R. Jradi, C. Marvillet, and M. R. Jeday, "Application of an Artificial Neural Network Method for the Prediction of the Tube-Side Fouling Resistance in a Shell-And-Tube Heat Exchanger," Fluid Dynamics and Materials Processing, vol. 18, no. 5, pp. 1511–1519, 2022, doi: 10.32604/fdmp.2022.021925.
- S. Wang et al., "A novel battery thermal management system for an unmanned aerial vehicle using the graphene directional heat transfer structure," J Power Sources, vol. 588, p. 233726, Dec. 2023, doi: 10.1016/j.jpowsour.2023.233726.
- S. Sammil and M. Sridharan, "Employing ensemble machine learning techniques for predicting the thermohydraulic performance of double pipe heat exchanger with and without turbulators," Thermal Science and Engineering Progress, vol. 47, p. 102337, Jan. 2024, doi: 10.1016/J.TSEP.2023.102337.
- S. Thanikodi, D. K. Singaravelu, C. Devarajan, V. Venkatraman, and V. Rathinavelu, "Teaching learning optimization and neural network for the effective prediction of heat transfer rates in tube heat exchangers," Thermal Science, vol. 24, pp. 1–7, 2020, doi: 10.2298/TSCI190714438T.
- S. Muthukrishnan, H. Krishnaswamy, S. Thanikodi, D. Sundaresan, and V. Venkatraman, "Support vector machine for modelling and simulation of heat exchangers," Thermal Science, vol. 24, no. 1 Part B, pp. 499–503, 2020, doi: 10.2298/TSCI190419398M.
- S. M. Ekrani, S. Ganjehzadeh, and J. A. Esfahani, "Multi-objective optimization of a tubular heat exchanger enhanced with delta winglet vortex generator and nanofluid using a hybrid CFD-SVR method," International Journal of Thermal Sciences, vol. 186, Apr. 2023, doi: 10.1016/j.ijthermalsci.2023.108141.
- S. H. Godasiaei and A. J. Chamkha, "Advancing heat transfer modeling through machine learning: A focus on forced convection with nanoparticles," Numeri Heat Transf A Appl, pp. 1–23, Jan. 2024, doi: 10.1080/10407782.2023.2299734.
- T. Chen and C. Guestrin, "XGBoost," in Proceedings of the 22nd ACM SIGKDD International Conference on Knowledge Discovery and Data Mining, New York, NY, USA: ACM, Aug. 2016, pp. 785–794. doi: 10.1145/2939672.2939785.
- Y. Freund and R. E. Schapire, "Experiments with a new boosting algorithm," in Proceedings of the Thirteenth International Conference on International Conference on Machine Learning, in ICML'96. San Francisco, CA, USA: Morgan Kaufmann Publishers Inc., 1996, pp. 148–156.
- Y. W. Son, D. Kang, and J. Kim, "Passive battery thermal management system for an unmanned aerial vehicle using a tetrahedral lattice porous plate," Appl Therm Eng, vol. 225, p. 120186, May 2023, doi: 10.1016/j.applthermaleng.2023.120186.

LSTM-Based Regional Load Forecasting for Electricity Distribution Feeders: The Bölcek Case

Turgay ÖZZEFTCİ* İlker DURSUN ²

¹Department of Electrical and Electronics Engineering, Sakarya University of Applied Sciences, Turkey (ORCID: https://orcid.org/0009-0005-3110-3648)

²Graduate Education Institute, Sakarya University of Applied Sciences, Turkey (ORCID: https://orcid.org/0000-0002-2550-8666)

^{*(22500405012@}subu.edu.tr) Email of the corresponding author

ABSTRACT

Accurate electricity load forecasting at the feeder level is crucial for ensuring operational reliability and informed investment decisions in modern power distribution systems. This study proposes a machine learning-based load forecasting model for the Bölcek feeder, situated within the Bergama Transformer Center in western Turkey. The model was developed using hourly multivariate data collected between 2022 and 2024, including electrical parameters such as current, voltage, and active/reactive power. Data preprocessing steps included time indexing, normalization via Min-Max scaling, and the application of a sliding window technique to extract sequential dependencies. A Long Short-Term Memory (LSTM) neural network was trained using these sequences, with training conducted over 100 epochs using the Adam optimizer. The model demonstrated successful convergence during training, achieving a final MSE of approximately 0.0022. However, performance on the 2024 test set revealed generalization limitations, with a negative R² value indicating overfitting. Despite this, the model was able to replicate seasonal load patterns to a certain degree. The results emphasize that while LSTM models are capable of capturing temporal trends, their forecasting reliability depends heavily on input diversity and model regularization. This research contributes to the ongoing exploration of deep learning for localized energy forecasting and offers insights for smarter grid management and feeder-level planning.

Keywords – Electricity, Bölcek, machine learning, forecasting, feeder-level planning

I. Introduction

The increasing complexity of modern power distribution systems has made accurate and localized load forecasting an essential component of operational planning and network optimization. Factors such as growing energy demand, the integration of renewable energy sources, changing consumption patterns, and the electrification of transportation have led to more dynamic and unpredictable grid behaviors. In this context, the ability to predict short- and medium-term electricity load at the regional or feeder level has become vital for ensuring the stability, efficiency, and resilience of electricity networks. As distribution system operators seek to improve infrastructure management and resource allocation, the use of intelligent forecasting techniques has gained momentum. Traditional statistical methods are gradually being replaced or complemented by machine learning models that can handle high-dimensional, nonlinear, and time-dependent data. Among these, deep learning architectures such as Long Short-Term Memory (LSTM) networks have shown promise in capturing temporal dependencies and learning complex patterns from historical operational data. This study proposes a data-driven forecasting framework tailored to a specific regional feeder in Türkiye. Using multivariate time-series data that include current, voltage, and various types of power measurements, the model aims to generate hourly electricity load forecasts for future years. The results of this approach are intended to support decision-making processes related to capacity planning, preventive maintenance, and investment prioritization within regional distribution grids.

Accurate load estimation is foundational to the success of rural and regional electrification planning, particularly in settings with limited consumption data. Namaganda-Kivimba et al. [1] addressed this challenge by proposing an improved load estimation methodology tailored for rural electrification systems. Their approach integrates socio-economic survey data and stochastic user behavior models to enhance the accuracy of demand projections, which is crucial for right-sizing distributed energy systems. This framework offers a robust alternative to conventional load profiling methods that often suffer from generalization issues in low-infrastructure settings. Complementing this, Azeem et al. [2] presented a comprehensive review of load forecasting models across various electricity generation modalities. They systematically evaluated statistical, intelligence (AI), and hybrid forecasting techniques based on their performance across different time horizons and power system types (e.g., conventional, renewable, and hybrid grids). The study highlights how machine learning models particularly deep neural networks and ensemble methods—outperform traditional models in complex, data-rich environments, whereas simpler statistical models retain value in short-term or low-resolution contexts. These insights form the theoretical foundation for adopting AI-based models in localized forecasting scenarios like the Bölcek feeder. The performance of artificial neural networks (ANNs) in short-term electricity load forecasting is better understood through experimental analyses conducted on categorized data. Evren and Özkan (2021) categorized daily electricity load data into three categories—summer, winter, and transitional seasons—and compared different ANN structures in a comparative manner. The effects on accuracy were evaluated by changing the number of inputs, the number of hidden layers, and the epoch parameters in the model architectures. It was observed that prediction errors increased in summer and that ANNs performed more consistently in transitional seasons. These findings reveal that seasonal effects and data categorization play a decisive role in model success. The study emphasizes the contribution of seasonal analyses to enhancing the generalizability and accuracy of electricity load prediction models at the regional level [3]. Another significant contribution to the field comes from Chodakowska, Nazarko, and Nazarko [4], who examined the robustness of Autoregressive Integrated Moving Average (ARIMA) models in the context of noise-affected electric load forecasting. Their study rigorously assessed how stochastic disturbances influence forecasting precision across different time horizons. The analysis revealed that although ARIMA models generally deliver stable and interpretable outputs, their sensitivity to noisy input data may limit performance, especially in high-resolution or volatile demand scenarios. Importantly, the authors highlighted the importance of preprocessing techniques to reduce noise impact and enhance model robustness. These insights are valuable for applications in regional distribution networks, where data integrity can vary, and reinforce the necessity of preprocessing in this study's methodology. Recent advancements in hybrid modeling have emphasized the integration of deep learning architectures with classical time-series frameworks for enhanced accuracy in load forecasting. Shohan et al. [5] developed a hybrid LSTM-Neural Prophet model tailored to capture both trend and seasonality components in electric load data. Their work demonstrated that by leveraging the strengths of both long short-term memory networks (which are adept at capturing temporal dependencies) and the Neural Prophet model (which efficiently handles additive components and changepoints). significant improvements in forecast precision can be achieved. This hybrid approach was validated using real-world consumption datasets, showing that it consistently outperformed baseline models, especially under fluctuating demand conditions. The study underlined the adaptability of hybrid models in dynamically changing environments and suggested their applicability in localized and highresolution load forecasting tasks, similar to the objectives of the current research. s power systems move toward greater electrification, particularly with the integration of electric vehicles (EVs) and nonlinear residential loads, ensuring accurate load forecasting must also consider their power quality implications. One recent study introduced a probabilistic methodology to assess harmonics and voltage unbalance resulting from increased penetration of such loads in residential low voltage networks [6]. The analysis, grounded in Monte Carlo simulations, incorporated uncertainties in load behavior, EV charging patterns, and stochastic spatial-temporal allocation. The results revealed that power quality could significantly deteriorate under high EV and nonlinear load penetration, especially when integrated with photovoltaic generation. The methodology was validated using both the IEEE European Low Voltage test system and a 471-bus residential network, offering results benchmarked against EN50160 standards. These findings stress the importance of embedding power quality considerations into regional load forecasting frameworks, particularly when dealing with evolving residential consumption patterns—a concern especially relevant for distribution-level systems like the Bölcek feeder. Chen and Zhang (2021) proposed a theory-guided deep learning framework (TgDLF) that incorporates physical load characteristics into an ensemble LSTM network. This model leverages both historical consumption data and theoretical load profiles to improve short-term and mid-term forecast accuracy. In comparative evaluations against traditional LSTM models, TgDLF demonstrated superior performance, particularly in scenarios with noisy or incomplete data. The study emphasized the value of embedding theoretical constraints within the learning process to prevent overfitting and to better generalize across varying operational conditions. These findings align well with the methodological direction of this study, which also leverages LSTM-based architectures for feeder-level load prediction under real-world data variability [7]. Gasparin et al. (2022) proposed a comprehensive examination of deep learning methods applied to electric load forecasting. Their study demonstrated the ability of models such as CNNs, RNNs, and LSTMs to capture complex temporal dependencies, non-linearities, and hidden trends in consumption patterns. Moreover, the authors emphasized the importance

of data quality and the benefits of transfer learning techniques in domains with limited labeled data. The review also highlighted challenges such as overfitting, model interpretability, and computational cost. This study supports the integration of deep learning architectures into feeder-level forecasting frameworks, offering valuable insights for regional energy planning strategies [8]. Another innovative approach is presented by Dong, Ma, and Fu (2021), who propose a hybrid deep learning model that integrates the K-Nearest Neighbors (KNN) algorithm as a prefiltering mechanism before feeding data into a deep neural network for load forecasting. Their method aims to reduce the noise and variance in the training dataset by selecting the most relevant historical data based on similarity in features such as time, temperature, and consumption trends. This KNN-based preselection improves the neural network's ability to learn meaningful temporal patterns, especially in non-linear and non-stationary time series data. Experimental results on real-world load datasets demonstrate that the model significantly outperforms traditional deep learning architectures in both short- and medium-term forecasting accuracy. The study highlights the potential of blending statistical proximity-based methods with deep learning architectures to enhance both precision and robustness in electricity demand modeling, offering a promising direction for feeder-level forecasting where data variability is often high [9]. Artificial neural networks (ANN) remain a pivotal tool in short-term load forecasting, especially in capturing nonlinear consumption patterns. Kamber et al. (2021) conducted a comprehensive investigation into ANN-based models for predicting short-term electricity demand. Their study utilized hourly consumption data, examining how neural network structures could be optimized for different seasons and consumption profiles. The results emphasized that properly tuned ANN architectures outperformed conventional models, especially under fluctuating load conditions. Notably, the authors highlighted the advantage of multi-layered neural topologies in handling complex temporal relationships, a relevant consideration for feeder-level forecasting in dynamically changing regional networks such as Bölcek. Their findings support the integration of ANN-based techniques in localized forecasting systems aiming to enhance prediction accuracy and grid responsiveness [10]. Kaysal, Akarslan ve Hocaoğlu (2022), Türkiye'nin kısa vadeli elektrik yük tahminine yönelik farklı makine öğrenmesi algoritmalarının karsılastırmalı analizini sunmustur. Calısmada Yapay Sinir Ağları (ANN), Ridge Regresyonu, Lasso Regresyonu ve Destek Vektör Regresyonu (SVR) gibi çeşitli modeller, 2019 yılına ait saatlik elektrik tüketim verileri üzerinde test edilmiştir. Tahmin performansı, RMSE, MAE ve R² metrikleriyle değerlendirilmiş ve ANN modeli özellikle doğrusal olmayan tüketim eğilimlerini öğrenme kapasitesiyle öne çıkmıştır. Elde edilen sonuçlar, ANN'in 0.86 RMSE, 0.62 MAE ve 0.97 R² skorları ile diğer modellere kıyasla üstün performans gösterdiğini ortaya koymuştur. Bu bulgular, bölgesel düzeyde kısa dönem tahmin modelleri geliştirirken yapay sinir ağı tabanlı yaklaşımların dikkate alınması gerektiğini ve veri karakteristiklerine duyarlı model seçiminin tahmin doğruluğu üzerinde belirleyici bir etken olduğunu göstermektedir.

II. MATERIALS AND METHOD

This study aims to develop a multivariate short-term and medium-term electricity load forecasting model for the Bölcek feeder, located within the Bergama Transformer Center of Turkey's western distribution region. Historical load data collected from 2022 to 2024 were utilized for model training and evaluation, while forward-looking predictions were generated for the years 2025 through 2027. The methodological approach integrates deep learning with multivariate regression, specifically employing a Long Short-Term Memory (LSTM)-based neural network due to its proven capacity in modeling sequential dependencies in temporal datasets.

A. Data Collection and Preprocessing

The raw dataset was compiled from operational measurements recorded at the Bölcek feeder on an hourly basis. The collected data span across three years (2022–2024), covering various seasonal and operational conditions. Prior to model training, data were subjected to a series of preprocessing steps, including:

- **Missing Value Handling:** Interpolation techniques were employed to fill in sporadic missing entries.
- **Feature Engineering:** Additional variables such as calendar-based indicators (e.g., weekday/weekend, season) and lagged load values were generated to enhance the input feature space.
- **Normalization:** All numerical features were normalized using Min-Max scaling to ensure stable gradient descent convergence.

B. Model Architecture

The forecasting model was built using a Long Short-Term Memory (LSTM) neural network architecture, known for its effectiveness in learning temporal patterns and capturing long-term dependencies in time-series data. The model was designed as a multivariate regressor, taking multiple input features and forecasting a single target output—electric load. The architecture consisted of:

- **Input Layer:** Accepting multivariate sequences (e.g., load, hour, weekday, temperature if available).
- LSTM Layer(s): One or more LSTM layers with a specified number of hidden units, tuned via empirical experimentation.
- **Dense Output Layer:** A fully connected layer projecting the final hidden state to the predicted load value.

The model was implemented using Python and TensorFlow/Keras libraries, and trained on a GPU-enabled environment for computational efficiency.

C. Training and Evaluation

The dataset was split into training (2022–2023) and test sets (2024), with the test set simulating unseen operational conditions to assess generalizability. The loss function used was Mean Squared Error (MSE), and model performance was monitored using:

- Root Mean Square Error (RMSE)
- Mean Absolute Error (MAE)
- Coefficient of Determination (R²)

Optimization was conducted using the Adam optimizer with a learning rate schedule to avoid overfitting and enable faster convergence. Training was performed over 100 epochs with early stopping applied based on validation loss.

D. Forecasting Future Load(2025-2027)

After validating the model on 2024 data, the trained LSTM model was deployed to forecast hourly electricity load profiles for the years 2025 to 2027. These forward predictions are expected to support distribution planning and regional energy management.

III. RESULTS

In this section, the performance of the proposed LSTM-based multivariate forecasting model is presented. The model was trained using hourly electricity load data from 2022 and 2023, validated and tested on the year 2024, and used for forward predictions for the period of 2025 to 2027. The evaluation metrics used include Root Mean Square Error (RMSE), Mean Absolute Error (MAE), and the Coefficient of Determination (R²). The training loss showed steady convergence over the epochs, achieving a final MSE of approximately 0.0039. However, when applied to the 2024 test set, the model yielded a negative R² score, indicating poor generalization performance. This suggests that while the model was able to capture patterns in the training data effectively, it struggled to extrapolate to unseen data, possibly due to seasonal shifts or distributional changes in the input space. The predicted hourly load for selected months in 2025–2027 shows recurring seasonal trends, with noticeable peaks during summer and winter months, consistent with historical consumption behavior. However, due to the overfitting issue identified during testing, the absolute reliability of these long-term forecasts should be interpreted with caution. The test phase results—particularly the negative R² value—indicate that the model may have overfitted the training data or failed to capture structural shifts between 2023 and 2024. Contributing factors may include:

• Incomplete or noisy input features (e.g., missing weather data).

- Insufficient temporal diversity in the training set.
- Lack of ensemble regularization or hybridization.

These insights suggest potential improvements for future work, such as implementing ensemble LSTM architectures, introducing weather covariates, or applying attention mechanisms for better temporal context learning. All results obtained are shown in Table 1. The workflow diagram is shown in Figure 1.

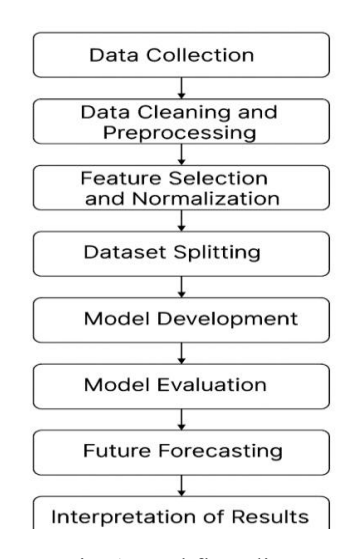


Fig. 1 Workflow diagram

 Dataset
 RMSE
 MAE
 R^2

 Training (2022-23)
 0.0625
 0.0481
 0.945

 Test (2024)
 0.1548
 0.1116
 -0.157

Table 1. Performance metrics summary

IV. DISCUSSION

The experimental results indicate that the proposed LSTM-based multivariate model performs well during training, achieving low error metrics and a high R² score. However, its test performance on 2024 data reflects a clear generalization problem, as evidenced by the negative R². This discrepancy suggests that the model learned temporal patterns specific to the training years (2022–2023) but failed to effectively adapt to variations in the unseen 2024 data. Several potential causes may underlie this issue. Firstly, load behavior in electrical distribution systems is highly sensitive to seasonal, behavioral, and policy-related factors. The absence of external

features such as weather data (temperature, humidity), calendar effects (holidays), or macroeconomic indicators may have limited the model's ability to generalize across different temporal contexts. Secondly, the relatively small size of the training dataset—limited to only two years of hourly data—may not have been sufficient to cover the complex, periodic patterns necessary for reliable extrapolation. Additionally, the model architecture did not include regularization techniques such as dropout or ensemble methods, which could have improved generalization performance. Despite the suboptimal performance on the 2024 test set, the forecasted load patterns for 2025–2027 appear structurally consistent with historical trends. The model was able to replicate annual demand cycles, suggesting that it retains some capacity to capture long-term seasonality. Nevertheless, these forecasts should be interpreted cautiously, and further refinements—such as the incorporation of hybrid deep learning models or feature expansion—are recommended for future studies.

V. CONCLUSION

This study presents a data-driven regional load forecasting application for the Bölcek feeder, leveraging a Long Short-Term Memory (LSTM) based multivariate regression model. The model was trained on hourly load data from 2022 to 2023 and validated on 2024 to predict electricity consumption for the 2025–2027 period. While the training results demonstrated strong fitting performance, the model failed to generalize effectively to the test set, as shown by a negative R² value. The findings emphasize the critical importance of feature diversity and model robustness in electrical load forecasting tasks. Even though LSTM networks are inherently capable of learning long-term dependencies, their standalone use may fall short in dynamic real-world environments unless supported by hybrid strategies or external inputs.

Future work should consider the integration of weather and socioeconomic indicators, attention-based mechanisms, and ensemble learning strategies to improve the model's adaptability and accuracy. Moreover, expanding the training dataset to include more years and capturing multiple seasonal cycles may significantly enhance generalization. Despite current limitations, this study contributes to the growing body of research emphasizing localized, feeder-level demand prediction using machine learning, and serves as a practical reference for utility companies and policymakers aiming to enhance distribution grid resilience and planning accuracy.

REFERENCES

- [1] Namaganda-Kiyimba, J., Mutale, J., & Azzopardi, B. (2021). Improving the Load Estimation Process in the Design of Rural Electrification Systems. *Energies*, *14*(17), 5505. https://doi.org/10.3390/en14175505
- [2] Azeem, A., Ismail, I., Jameel, S. M., & Harindran, V. R. (2021). Electrical load forecasting models for different generation modalities: A review. *IEEE Access*, 9, 142239–142263. https://doi.org/10.1109/ACCESS.2021.3119990
- [3] Evren, V., & Ozkan, I. A. (2021). Comparison of artificial neural network models of categorized daily electric load. *MANAS Journal of Engineering*, 9(Special 1), 24–34.

- [4] Chodakowska, E., Nazarko, J., & Nazarko, Ł. (2021). ARIMA models in electrical load forecasting and their robustness to noise. *Energies*, 14(23), 7952. https://doi.org/10.3390/en14237952
- [5] Shohan, M. J. A., Faruque, M. O., & Foo, S. Y. (2022). Forecasting of electric load using a hybrid LSTM-neural prophet model. *Energies*, 15(6), 2158. https://doi.org/10.3390/en15062158
- [6] Rodríguez Pajarón, P., Hernández, A., & Milanovic, J. V. (2021). Probabilistic assessment of the impact of electric vehicles and nonlinear loads on power quality in residential networks. *International Journal of Electrical Power & Energy Systems*, 129, 1-11. Chen, Y., & Zhang, D. (2021). Theory-guided deep-learning for electrical load forecasting (TgDLF) via ensemble long short-term memory. *Advances in Applied Energy*, 1, 100004. https://doi.org/10.1016/j.adapen.2020.100004
- [7] Chen, Y., & Zhang, D. (2021). Theory-guided deep-learning for electrical load forecasting (TgDLF) via ensemble long short-term memory. *Advances in Applied Energy, I*, 100004. https://doi.org/10.1016/j.adapen.2020.100004
- [8] Gasparin, A., Lukovic, S., & Alippi, C. (2022). Deep learning for time series forecasting: The electric load case. *CAAI Transactions on Intelligence Technology*, 7(1), 1–25. https://doi.org/10.1049/cit2.12023
- [9] Dong, Y., Ma, X., & Fu, T. (2021). Electrical load forecasting: A deep learning approach based on K-nearest neighbors. *Applied Soft Computing*, 99, 106900. https://doi.org/10.1016/j.asoc.2020.106900
- [10] Kamber, E., Körpüz, S., Can, M., & Yumurtacı Aydoğmuş, H. (2021). Yapay sinir ağlarına dayalı kısa dönemli elektrik yükü tahmini. *Endüstri Mühendisliği*, *32*(2), 364–379. https://doi.org/10.46465/endustrimuhendisligi.820509
- [11] Kaysal, K., Akarslan, E., & Hocaoğlu, F. O. (2022). Türkiye kısa dönem elektrik yük talep tahmininde makine öğrenmesi yöntemlerinin karşılaştırılması. *Bilecik Şeyh Edebali Üniversitesi Fen Bilimleri Dergisi*, *9*(2), 693–702. https://doi.org/10.35193/bseufbd.1004827

Analysis of uncontrolled blowouts from oil and gas drilling

Timur Chis^{1*}
AL-Gburi Hasan Ali Mosleh²
Daniel Iancu²

ABSTRACT

During drilling operations carried out for the purpose of exploring or exploiting oil and/or natural gas deposits, uncontrolled eruptions (technical accidents) have also occurred, which have led to damage to the well and, in particular, have affected the capacity of the productive layers to continue producing under the initial conditions provided for in the exploitation projects.

This article analyzes the inflow of fluids from the formation into the well and mathematizes the equations of flow of eruptive fluids through wells.

Keywords - Oil and gas drilling, oil and gas eruption, modeling

I INTRODUCTION

During oil and gas drilling a serious accidents can occur because it is posible to:

- a. During the passage of the productive layer, as a result of the penetration of fluids that saturate this layer into the drilling fluid,
- b. As a result of pressure variations during the extraction maneuver of the drilling rig,
- c. As a result of pistoning or sleeve operations on the productive layer and/or the casing string,
- d. As a result of the loss of drilling fluid during rock dislocation operations (as a result of its penetration into the productive layers) and its complete isolation,
- e. As a result of the use of a blowout preventer, unclassified or inappropriate, for the pressure class in the well,
- f. During drilling or operations to increase the productivity of wells,
- g. As a result of erosion/corrosion of the drill tubing or casing strings and therefore the occurrence of unscheduled multiphase fluid leaks,
- h. As a result of the failure of the sealing gaskets at the flanges of the strings or the blowout heads (occurrence of fluid leaks in the form of a jet).

The fluids that could erupt are [2]:

- Natural gas associated with productive or under-exploration deposits,
- Crude oil.
- Water associated with the deposit penetrated by drilling,
- Sand and traces of rocks dislodged by drilling,
- Components of the drilling fluid (chemicals, biological products, components to increase the capacity of the productive layer, elements to reduce the permeability of the drilled layer, etc.),
- Dislodged elements from equipment (metallic or other) damaged as a result of the uncontrolled flow of fluids from the erupting wells.

The way an uncontrolled eruption occurs is primarily due to the fact that during drilling, while crossing the layer saturated with fluids under pressure, a pressure imbalance usually occurs (between the hydrostatic pressure of the liquid column in the well and the pressure under which the fluids in the layer are found).

If the hydrostatic pressure of the liquid column is lower than the pressure in the formation, the fluids in the formation penetrate into the well fluid, leading to a sharp decrease in the hydrostatic pressure of the liquid column at the formation level (due to the diffusion of gas particles in the drilling fluid).

It has been observed that the fluids that saturate the formation can penetrate into the drilling fluid even if the hydrostatic pressure of the liquid column in the well (at the formation level) is higher than the pressure at which the fluids that saturate the formation are found (due to the gasification of the drilling fluid by the adsorption of gases on the surface of colloidal clay particles in the drilling fluid).

In the case of saturation of the productive layer only with the liquid phase (no free or in solution gases), a decrease in the specific gravity of the drilling fluid is observed (which can be corrected) and is due to the diffusion of liquid particles due to the density variation between the two fluids in contact.

The pathways of gas penetration into drilling fluids lead to gasification of the drilling fluid and are due to:

- a. Dissolution of gases in the free water in the drilling fluid,
- b. Diffusion in the form of bubbles,
- c. Adsorption on the surface of colloidal particles,
- d. Dislocation of rocks by the drilling bit and penetration of gases into the fluid,
 - e. Effusion processes.

II. MODELING OF OIL AND GAS ERUPTION

The volume of gases entering the solution is a function of pressure, temperature, nature of the gas, type of rocks, adsorption capacity of colloidal particles, etc.

The influence of pressure on the amount of dissolved gases (at a constant temperature) is determined by Henry's law [3]:

$$V_g = \alpha p \tag{1}$$

In equation 1 α is the solubility coefficient of gases in liquid (Nm³/m³ atm), V_g represents the volume of gases dissolved in one m³ of liquid (Nm³/m³), and p is the pressure of the analyzed system (bar).

But considering that in a well there cannot be a constant temperature (from the bottom of the well to the surface) there is a variability

of the solubility coefficient (at the bottom of the well the solubility of gases is lower).

On the other hand, the volume of dissolved gases depends on the nature of the gas, ethane and propane dissolving in a larger volume than methane.

In construction site practice it was observed that as the drilling fluid rises, the pressure at different levels decreases (towards the surface) leading to the release of gases from the solution and therefore its gasification (decrease in specific gravity).

The diffusion of gases into drilling fluids occurs in the vicinity of hydrocarbon-saturated layers (especially when circulation is interrupted for long periods of time).

The variation of the solubility coefficient of gases in the liquid (as a function of temperature) is given by the relationship [1]:

$$\alpha_2 = \alpha_1 e^{\frac{\Delta H(T_2 - T_1)}{R T_2 T_1}} \tag{2}$$

In equation 2 we have:

- α is the Bunsen constant (the coefficient that describes the volume of gas expressed under standard conditions that dissolves in a unit volume of solvent at a given pressure and temperature),
- H is the differential heat of dissolution,
- T is the absolute temperature, °K,
- R is the universal gas constant.

In the case of fluids that contain gases from the productive layers (derived by diffusion from fluids existing in the productive horizons or that contain gases in their composition), the extraction of dislocated rocks takes place (through the circulation of the drilling fluid), the gas bubbles (present in the fluid) reaching the detritus treatment and separation unit.

In practice, it is desirable that in the case of fluids containing associated gases, the drilling speed be chosen so that the volume of gases entering the drilling fluid is lower than that which would cause a decrease in the specific gravity of the fluid between the column (wellbore) and the drilling casing and therefore the migration of gases to the surface.

The adsorption of free gases on the surface of colloidal clay particles can lead to the manifestation of the productive layer (even if the hydrostatic pressure of the liquid column in the well at the level of this layer is higher).

Given that drilling fluids are colloidal solutions of clays and water, the particle radius being of the order of $r=3\cdot10^{-6}$ cm, the specific surface area is of the order of $=105\frac{cm^2}{dm^3}$ of fluid, the value of the specific surface area of the rock particles brought to the surface by the drilling fluid is extremely high, at the boundary of separation of the two phases (water/clay) the phenomenon of gas adsorption takes place (i.e. the agglomeration of gas molecules on the surface of the solid phase).

Due to this phenomenon we can determine the pressure of the fluids in the layer (at equilibrium) as:

$$p_s = \left(\frac{1}{A\Psi} + C\right) \frac{h\gamma}{10} \tag{3}$$

In equation 3 Ψ represents the content of gases embedded in the drilling fluid (expressed as a decimal fraction), A and C being experimentally determined coefficients.

Also in determining the pressure in the layer, it is important to determine the drilling depth h (m) and the specific gravity of the drilling fluid.

The analyses performed on the data from the studied drillings demonstrate that the useful values for the coefficients A and C are close to the values 1.08 and 0.074.

But analyzing equation 3 we can state that below the value $\Psi \leq 1$ (i.e. below the saturation limit), the factor $\frac{1}{A\Psi} + C$ is greater than 1 and therefore there is the possibility of digging a gas layer with a drilling fluid (digger) that has a hydrostatic pressure of the fluid column lower than the pressure in the layer.

The presence of gases in the drilling fluid makes the real pressure at the level of the productive layer to be[1]:

$$p_r = p_s - p_a = \frac{h\gamma}{10} \tag{4}$$

Or the above equation can also be written in the form:

$$p_r = \beta_a \frac{h\gamma}{10} \tag{5}$$

Where:

- p_s is the fluid pressure in the formation (bar),
- p_a is the adsorption pressure (bar),
- h is the height of the fluid column in the well (m),
- γ is the specific gravity of the drilling fluid (gr/cm3),
- β_a is a correction coefficient due to the adsorption phenomenon.

This coefficient is a function of the gas content α in the drilling fluid (expressed as a decimal fraction) and of two coefficients (A and C) determined experimentally.

$$\beta_a = \frac{1}{A^\alpha} + C \tag{6}$$

Analyzing equation 6, it is observed that below the saturation limit $(\alpha \le 1)$, we obtain $\beta_a \ge 1$ and therefore the pressure in the gas layer can be greater than the hydrostatic pressure of the drilling fluid used to penetrate this layer through the well.

$$\beta_a \cong \frac{1}{1.08^a} + 0.074 \tag{7}$$

When reaching the gas adsorption limit in the drilling fluid, $\alpha > 1$, the gases penetrate through the drilling fluid cake (deposited on the walls of the wellbore) in the form of fine networks of bubbles (adhering to the solid particles in the drilling fluid).

The radius of these bubbles varies inversely proportional to the gasfluid interfacial tension and the viscosity of the fluid, at high values of viscosity the bubbles have small radii and therefore can be more easily torn off the walls of the wellbore by the drilling fluid in the movement in which they then penetrate it.

In order to mathematize the above mentioned, a correction factor was introduced which is a function of the viscosity of the drilling fluid (μ expressed in s Marsch), namely:

$$\beta_V = 0.24 \frac{1}{1 + (\frac{\mu}{20})^2} + 0.88 \tag{8}$$

In this case the pressure in the fluid layer p_s can be written as:

$$p_s = (0.24 \frac{1}{1 + (\frac{\mu}{20})^2} + 0.88) (\frac{1}{A\Psi} + C) \frac{\dot{h}\gamma}{10}$$
 (9)

Which meets the condition:

$$(0.24 \frac{1}{1 + (\frac{\mu}{20})^2} + 0.88)(\frac{1}{A\Psi} + C) < 1 \tag{10}$$

The influx of fluids from the layer into the well can occur even though the apparent hydrostatic pressure of the drilling fluid column $(\frac{h\gamma}{10})$ at the level of the productive layer has a higher value than the pressure of the fluids that saturate the layer p_s .

$$p_s = \beta_a \beta_V \frac{h\gamma}{10} \tag{11}$$

When the viscosity tends to infinity β_V from equation 11 becomes equal to 0.88.

If the product $\beta_a\beta_V < 1$ then the inflow of fluids from the layer into the well occurs even if the numerical value of the hydrostatic pressure $(\frac{h\gamma}{10})$ of the drilling fluid at the level of the hole has a value greater than the saturated layer pressure p_s .

At low values of the viscosity of the drilling fluid, the bubbles are large and adhere strongly to the walls of the well (a greater mechanical energy is required to remove them).

III. ANALYSIS OF THE CHANGE IN THE HYDROSTATIC PRESSURE OF THE DRILLING FLUID DURING THE MANEUVER OF THE DRILLING RIG

The change in the hydrostatic pressure of the fluid column in the well, during the operation of the drilling rig, was highlighted by W.T. Cardwell [2].

W.T. Cardwell defined the viscosity of the drilling fluid in linear flow, starting from the axially symmetric flow relation:

$$\frac{\partial}{\partial x}(p + \rho gh) = \frac{\mu}{r} \frac{\partial}{\partial r} (r \frac{\partial v}{\partial r}) \tag{12}$$

Where:

- x is the distance of viscosity and velocity measurement along the flow axis,
- p is the drilling fluid pressure,
- ρ is the drilling fluid density,
- g is the gravitational acceleration,
- v is the drilling fluid velocity,
- r is the well radius.
- h is the well depth.

Given that the x-axis corresponds to the vertical of the well, equation 12 can be written as:

$$\frac{\partial p}{\partial x} - \rho g = \frac{\mu}{r} \frac{\partial}{\partial r} (r \frac{\partial v}{\partial r}) \tag{13}$$

In axial drilling fluid flow, none of the variables in equation 13 vary in the x direction, except for pressure and pressure drop, equation 13 can be simplified to the form:

$$\frac{\Delta p}{l} - \rho g = \frac{\mu}{r} \frac{\partial}{\partial r} (r \frac{\partial v}{\partial r}) \tag{14}$$

In equation 14, Δp is the pressure drop over length 1 (which is considered to be the length of a cylinder of surface S immersed in a cylinder of radius R.

An approximation is implicitly introduced in equation 14, namely that given the flow in depth, its effects on the well radius can be neglected, the deviation of the pressure (P) from the hydrostatic pressure being equal to:

$$P = \Delta p - \rho g l \tag{15}$$

In this case equation 15 becomes:

$$\frac{P}{I} = \frac{\mu}{r} \frac{\partial}{\partial r} \left(r \frac{\partial v}{\partial r} \right) \tag{16}$$

Equation 16 allows us to define the flow rate of the liquid (drilling fluid) inside the drill string (with radius S) and in the area between the drill string and the wellbore with radius S.

The equation for the flow rate of the drilling fluid through the inside of the drill string is given by the relation:

$$Q_p = -\frac{\pi P S^4}{8\mu l} + \pi S^2 u \tag{17}$$

And integrating the fluid flow through the area between the wellbore and the drill string, we obtain:

$$Q_a = -\frac{\pi P S^4}{8\mu l} (R^2 - S^2) \left(R^2 + S^2 - \frac{R^2 - S^2}{ln\frac{R}{S}} \right) + \frac{\pi u}{2} \left(\frac{R^2 - S^2}{ln\frac{R}{S}} - 2S^2 \right)$$
 (18)

If the borehole with radius R is closed at the bottom, the two fluxes must cancel each other out:

$$Q_p + Q_a = 0 (19)$$

$$Q_p + Q_a = 0$$

$$P = \frac{4l\mu u}{R^2} \frac{1}{(\frac{z^2}{z^2 - 1})lnz - (\frac{z^2}{z^2 - 1})}$$
(20)

$$P = \frac{4\tilde{l}\mu u}{R^2} F(z) \tag{21}$$

Where $z = \frac{R}{S}$ and u is fluid velocity.

The function
$$F(z)$$
 is given by the relation $F(z) = \frac{1}{(\frac{z^2}{z^2-1})lnz-(\frac{z^2}{z^2-1})}$, in

the specialized literature being determined by numerical calculation.

Analyzing the data of the wells in Romania We managed to determine by calculation the value of the function F(z) as a function of z, namely (figure 1):

$$F(z) = -0.0057z^6 + 0.1767z^5 - 2.1847 / z^4 + 13.686z^3 - 45.007z^2 + 70.913z - 35.963$$
 (22)

With a margin of error (the proportion of the variation in the dependent variable that is predictable from the independent variable) $R^2 = 0.9794$.

The pressure drop that occurs along the liquid column depends on the extraction speed, namely it increases with the speed of lifting the casing and also increases with the size of the annular space between the casing and the wellbore and directly proportional to the viscosity of the drilling fluid.

In the case of loading the drill bit or heavy casing with materials resulting from the dislocation of rocks, the space between them and the wellbore decreases even more so that this pressure variation actually leads to a decrease in the hydrostatic pressure of the liquid column (so at a value of this the layer starts to produce).

During the period when the casing is stopped for unscrewing a step, the balance is restored, but the pressure variation will occur when extracting the next step.

So the fluids that saturate the layer penetrate from the layer into the wellbore in the form of plugs at approximately equal intervals of time.

As the number of plugs increases, they are transshipped to the surface, causing small eruptions.

Finally, the hydrostatic pressure of the liquid column in the well drops below the pressure in the productive layer, at which point the layer will ensure the violent eruption of the drilling fluid-oil fluid mixture.

In the case of plugging the holes of the well, the pressure variation is accentuated at all levels in the well.

When lowering the drilling rig (rod) into the well, the same phenomenon occurs, with the caveat that the additional pressure acts downwards this time, which leads to an increase in the hydrostatic pressure of the liquid column exerted on the lower layers.

The increase in the hydrostatic pressure value leads to reaching the fracturing pressure of the productive layers and therefore a decrease in the liquid level in the well (due to its penetration into the cracks).

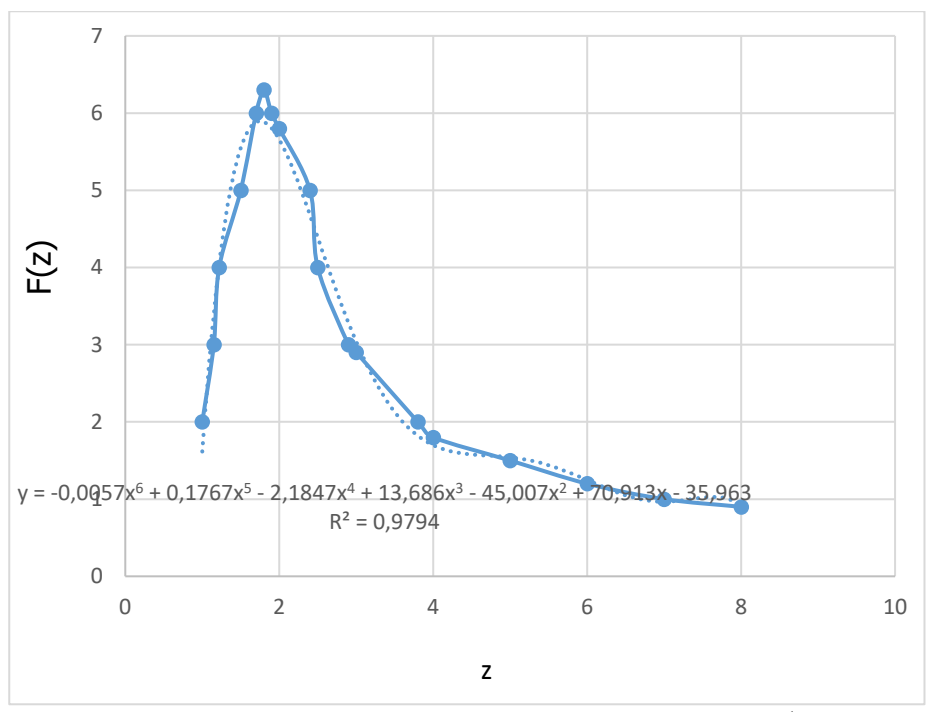


Fig 1. Evolution of the function F(z) as a function of z, $\left(F(z) = \frac{1}{\left(\frac{z^2}{z^2-1}\right)lnz-\left(\frac{z^2}{z^2-1}\right)}\right)$

When the rig stops, the balance is restored, but the liquid level in the well being low and therefore the hydrostatic pressure having a lower value than the pressure of the petroleum fluids, can lead to eruptive manifestations, due to the influx of fluids from the layer into the well.

In the present case, with a wellbore diameter of $8 \frac{3}{4}$ inches, and a drilling rig diameter of $4 \frac{1}{2}$ inches, we have a maneuver time of 10 seconds and with a drill string of 15,000 feet (4,572 m) we obtain a pressure drop of 1,000 psi (68 bar).

Crossing a zone with circulation losses (zone under oil, gas or aquifer formations) causes the liquid level in the well to decrease and therefore the hydrostatic pressure of the liquid column in the well (at the level of these formations) will become lower than the pressure under which the fluids that saturate the respective formations are found and therefore the fluids in the layer will begin to erupt.

Unlike the pistoning or sleeve effect, the pressure variation effect can occur in the rod packing without any external deposit (i.e. perfectly clean) or without the holes of the hole being clogged.

The pistoning or sleeve effect occurs when the drill, heavy rod or turbine are covered with material resulting from the dislocation of rocks and when the casing is moved upwards, the hydrostatic pressure of the liquid column under the sleeve decreases, which causes the inflow of fluids from the layer into the well.

When the maneuver is stopped, the pressure is restored, but the gases and crude oil no longer enter the layer, by repeating the phenomenon reaching a moment when the hydrostatic pressure of the liquid column at the layer level is lower than the pressure in the layer, so a sudden eruptive manifestation of the layer can be triggered.

Based on data collected in the specialized literature, in what follows we have created a numerical model regarding the evolution of the pressure drop when pulling or maneuvering the drill string for three pipe diameters (2 7/8 inch, 3 ½ inch and 4 ½ inch) over several time periods (90 seconds, 30 seconds, 10 seconds).

Thus we determined the pressure drop reported in psi/1000 feet (0.0689 bar/304 m or 0.000227 bar/m).

The equations are given in Table 1 and Figures 2,3,4.

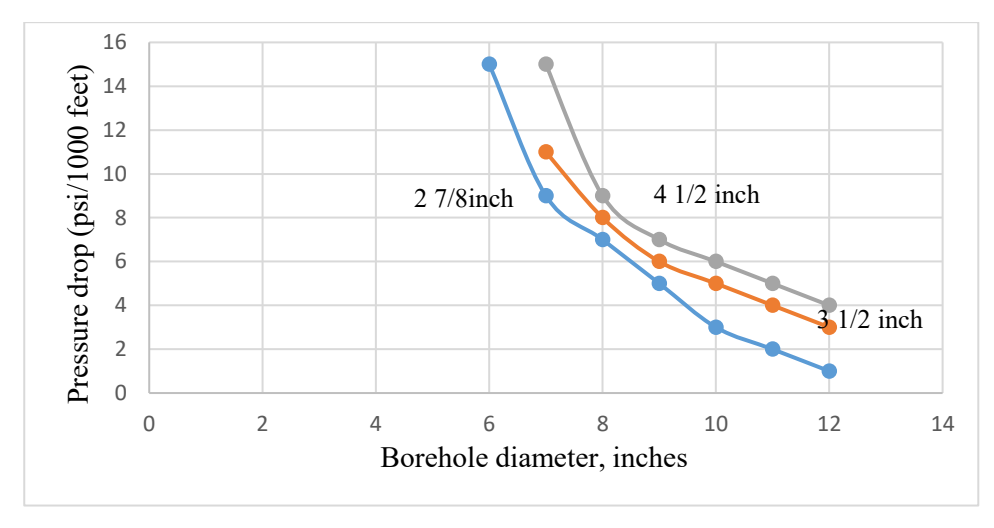


Fig. 2. Evolution of pressure drop (psi/1000 feet) as a function of wellbore diameter and drill string diameter at a handling time of 90 s

Table 1. Pressure drop reported in psi/1000 feet (0.0689 bar/304 m or 0.000227 bar/m).

Operational times, s	Wellbore diameter	Equation	R ²
90	2 7/8	$y = 203,41e^{-0,428x}$	0,9893
90	3 ½	$v = 60.61e^{-0.25x}$	0,991
90	4 1/2	$y = 70,39e^{-0,244x}$	0,9284
30	2 7/8	$v = 317.39e^{-0.363x}$	0,9874
30	3 ½	$y = 437,01e^{-0,374x}$	0,978
30	4 1/2	$y = 490,27e^{-0,362x}$	0,9924
10	2 7/8	$y = 1228,3e^{-0,413x}$	0,9697
10	3 ½	$v = 1479.8e^{-0.362x}$	0,9983
10	4 1/2	$y = 1150,5e^{-0,371x}$	0,9864

In the equations above, y represents the pressure drop reported in psi/1000 feet (0.0689 bar/304 m or 0.000227 bar/m) and x is the borehole diameter (inches).

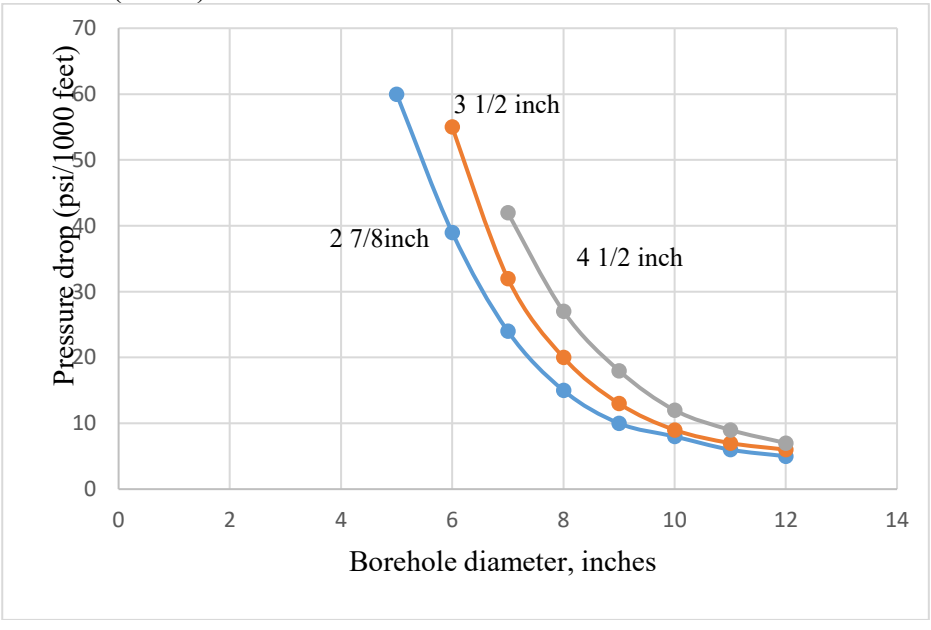


Fig. 3. Evolution of pressure drop (psi/1000 feet) as a function of wellbore diameter and drill string diameter at a handling time of 30 s

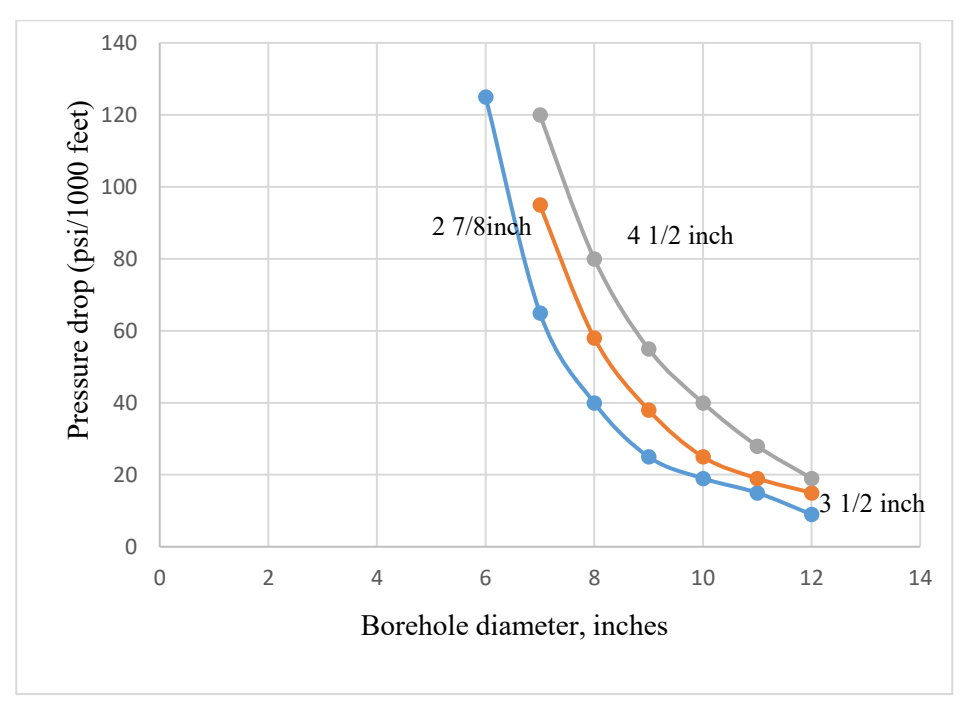


Fig. 2. Evolution of pressure drop (psi/1000 feet) as a function of wellbore diameter and drill string diameter at a handling time of 91 s

IV. RESULTS

The pressure drop that occurs along the liquid column depends on the extraction speed, namely it increases with the speed of lifting the casing and also increases with the size of the annular space between the casing and the wellbore and directly proportional to the viscosity of the drilling fluid.

In the case of loading the drill bit or heavy casing with materials resulting from the dislocation of rocks, the space between them and the wellbore decreases even more so that this pressure variation actually leads to a decrease in the hydrostatic pressure of the liquid column (so at a value of this the layer starts to produce).

During the period when the casing is stopped for unscrewing a step, the balance is restored, but the pressure variation will occur when extracting the next step.

So the fluids that saturate the layer penetrate from the layer into the wellbore in the form of plugs at approximately equal intervals of time.

As the number of plugs increases, they are transshipped to the surface, causing small eruptions.

Finally, the hydrostatic pressure of the liquid column in the well drops below the pressure in the productive layer, at which point the layer will ensure the violent eruption of the drilling fluid-oil fluid mixture.

In the case of plugging the holes of the well, the pressure variation is accentuated at all levels in the well.

When lowering the drilling rig (rod) into the well, the same phenomenon occurs, with the mention that the additional pressure acts downward this time, which leads to an increase in the hydrostatic pressure of the liquid column exerted on the lower layers.

The increase in the hydrostatic pressure value leads to reaching the fracturing pressure of the productive layers and therefore a decrease in the liquid level in the well (due to its penetration into the cracks).

Crossing an area with circulation losses (area located under oil, gas or aquifer formations) causes the liquid level in the well to decrease and therefore the hydrostatic pressure of the liquid column in the well (at the level of these formations) will become lower than the pressure under which the fluids that saturate the respective formations are found and therefore the fluids in the layer will begin to erupt.

Unlike the pistoning or sleeve effect, the pressure variation effect can occur at the rod seal without any external deposit (i.e. perfectly clean) or without the holes of the core being clogged.

The pistoning or sleeve effect occurs when the drill, heavy rod or turbine are covered with material resulting from the dislocation of rocks and when the casing is moved upwards, the hydrostatic pressure of the liquid column under the sleeve decreases, which causes the inflow of fluids from the layer into the well.

When the maneuver is stopped, the pressure is restored, but the gases and crude oil no longer enter the layer, by repeating the phenomenon reaching a moment when the hydrostatic pressure of the liquid column at the layer level is lower than the pressure in the layer, so a sudden eruptive manifestation of the layer can be triggered.

Based on data collected in the specialized literature, in what follows we have created a numerical model regarding the evolution of pressure drop when pulling or maneuvering the drill string, for three pipe diameters (2 7/8 inches, 3 $\frac{1}{2}$ inches and 4 $\frac{1}{2}$ inches) over several time periods (90 seconds, 30 seconds, 10 seconds).

V. CONCLUSION

So when extracting a cylindrical tube (the drill string) into another tube filled with liquid (the wellbore), the liquid in the immediate vicinity of the rising tube is drawn in the same direction, while the liquid further away from the tube tends to descend.

Since the liquid in the tube (the annular space) has an appreciable viscosity (of the drilling fluid), a shear phenomenon occurs between the two

streams, the rising liquid tends to reduce the hydrostatic pressure of the liquid column.

These pressure variations occur along the drill string and decrease along the fluid column from the bottom of the well to the surface.

Therefore, the pressure drop also depends on the extraction speed, increasing with the speed of lifting the string.

These pressure variations occur along the entire drill string and decrease linearly from the bottom of the well to the surface.

REFERENCES

- [1] T.Elusakin, , M. Shafiee, *Reliability analysis of subsea blowout preventers with condition-based maintenance using stochastic* Petri nets, Journal of Loss Prevention in the Process Industries, doi: https://doi.org/10.1016/j.jlp.2019.104026, 2020,
- [2] P. Hopkins, G. Goodfellow, R. Ellis, , N. Haswell, J. Jackson, *Pipeline risk assessment: new guidelines*, WTIA/APIA Welded Pipeline Symposium, Sydney, Australia, 2009.
- [3] D.Sulaiman, , D.Iancu, , H.Al Jubori, , The current state of research on the dilation processes of productive reservoir rocks related to natural gas wells, 75 Years of Energy and Performance in Education and Research 2023 Renewable Versus Fossil Fuels. Global Energy Perspectives, Ploiesti 9.11.2023, Book of abstracts, Editura Universității Petrol-Gaze din Ploiești, 2023, ISBN 978-973-719-887-7.

Risk assessment in the operation and safety of marine oil installations

Timur Chis^{1*}

Daniel Iancu ²

AL-Gburi Hasan Ali Mosleh²

ABSTRACT

After the Deepwater Horizon accident in 2010, the issue of creating adequate and modern EU-wide legislation on safety in the offshore oil and gas sector was raised. Thus, in June 2013, the European Parliament officially adopted Directive 30/2013/EU on the safety of offshore oil and gas operations (Offshore Safety Directive – OSD). The main objective of the Offshore Safety Directive is to reduce as much as possible the occurrence of major accidents and to limit their consequences in offshore oil and gas operations. Romania transposed the Offshore Safety Directive into Law 165, focusing on the technological, process and (risk) management aspects of offshore activities, the failure of which would have a possible significant impact on health and the environment, the objective being to ensure an adequate level of safety for People, Installations, The environment.

This article analyzes the risk of offshore structures in Romanian Black Sea Area

Keywords – Oil and gas platformas, risk assessment, modeling

I. INTRODUCTION

Oil – justifiably nicknamed "black gold" – has played an extremely important role in the world economy since the early years of the 20th century, and is still a very important player.

In recent years, there has been a shift in global industries towards other energy sources, such as wind power or electricity generated by photovoltaic panels, to ultimately replace oil and its derivatives, which are considered polluting.

The collapse in oil prices in 2014 negatively affected the activity of offshore drilling platforms, which also led to a drastic decrease in the number of active platforms worldwide.

As producers found themselves in a new environment, in which prices fell below the marginal cost of production, Offshore petroleum fluid production decreased in many oil-producing countries, in some cases even resuming the opening of new oil horizons.

Recent armed conflicts and especially the gradual transition of the global economy towards the Zero Emissions horizon, have led to the development of new possibilities for ensuring the energy necessary for the development of societies, with oil and natural gas consumption expected to decrease in the future.

In several states in the US, for example, the number of oil rigs, which had grown strongly between 2009 and 2014, has rapidly reached historically low levels.

As data on the number of operational offshore platforms show, the decline in their number was due to low oil prices and a shift towards other energy sources.

Over the course of six years, from 2008 to 2014, the number of natural gas production platforms fell 5 times (from around 1,600 in September 2008 to 340 today).

Regarding the current global oil reserves, which are expected to last a maximum of 47 years if no new discoveries are made, there are estimates that place them at about the same level as the amount extracted in the last 100 years, especially since the technological level that has been reached does not yet allow the full exploitation of existing reserves.

But known reserves will most likely last longer, because oil demand is declining in the highly developed part of the world.

According to current estimates, 79.4% of the world's proven oil reserves are located in OPEC member countries, with the largest share of OPEC oil reserves in the Middle East, accounting for 64.5% of OPEC's total.

OPEC member countries have made significant additions to their oil reserves in recent years, for example by adopting industry best practices, conducting intensive exploration and improving recovery.

As a result, OPEC's proven oil reserves currently amount to 1,189.80 billion barrels.

Romania would currently rank 44th with 600,000,000 barrels.

The offshore oil and gas industry is very important for the EU economy, with sixteen Member States involved.

II. CURRENT STATUS OF OFFSHORE PLATFORM SAFETY LEGISLATION

It is a fact that accidents that occur in the offshore area and that involve drilling and production installations, fixed or mobile, have happened and, unfortunately, still happen.

For a long time, offshore oil installations have been subject to EU legislative acts, applicable within the limits of territorial waters, i.e. 12 nautical miles from the baselines of the shore.

However, major shortcomings have been found in terms of legislative regulations in the event of a major accident beyond this limit, an event that could have a huge negative impact on human and material resources but also on the environment.

In 2013, the European Commission developed a much more comprehensive law on oil installations, which would target prevention, intervention and financial liability.

This directive was also implemented in Romania (due to the fact that our country has fluid hydrocarbon deposits in the Black Sea area and has also authorized operators to carry out exploitation, extraction and abandonment operations of these fossil resources. Law 165, which was promulgated in 2016, transposed into Romanian legislation Directive 2013/30, drafted by the European Parliament in 2013.

A critical analysis of the legislation on the safety of operation of Offshore installations and environmental protection (highlighted the lack in Romanian legislation, even in secondary legislation, of good practice guides, norms and

standards), of references to aspects that are part of offshore oil activity, which exist in the legislation of other countries with a tradition in the oil and gas industry.

III RISK ASSESSMENT AND IDENTIFICATION

Managing the integrity of offshore oil and gas platforms: a risk-based approach

Offshore oil and gas platforms are complex installations used for the exploration, drilling, extraction, processing and transportation of hydrocarbons.

These marine structures are designed to operate in extreme conditions, with varying temperatures and pressures, and handle potentially explosive substances.

Risks and regulations

Offshore operations present significant risks, which is why they are subject to rigorous risk assessments by insurance companies and government authorities. Failures can have serious consequences, including environmental pollution, human casualties and economic losses.

The importance of integrity management

Effectively managing the integrity of assets is crucial for the operational safety and reliability of facilities.

Offshore operators must develop integrity management strategies that ensure the safe, economical and reliable operation of platforms.

Optimizing Maintenance Costs

In the oil industry, maintenance costs represent a significant portion of expenses. Optimizing these costs by implementing risk-based inspection and maintenance plans is essential to reduce operational and economic risks.

From preventive to risk-based approaches

Stringent regulatory requirements and environmental concerns have led to the transition from time-based preventive maintenance strategies to risk-based approaches.

Risk assessment: an optimization technique

Risk assessment allows for the efficient allocation of inspection and maintenance resources, prioritizing activities based on the level of risk.

This approach contributes to cost control and operational safety.

The question is: what would be the risks identified for an oil installation located in the Black Sea and what could happen?

There are risks identified since the design period that can have an impact on health, safety at work and the environment.

Then there are risks associated with the operating period, production of hydrocarbons in the case of a fixed production platform.

The sections identified in this case would be:

- subsea wells with the eruption head mounted on the seabed;
- submarine pipelines and cables;
- the fixed platform itself, with or without crew on board;
- logistical operations at sea.

We have further compiled a list of possible hazards identified during the engineering period, relevant to the operational phase of the project, with the mention that some of them may lead to a major accident (Major Accident Hazard – PAM):

- unburned gaseous hydrocarbon released in the upper part of the installation (PAM);
 - process flame from the burner, fire caused by gas leakage (PAM);
 - explosions (PAM);
 - man overboard;
 - fires in various compartments;
 - collisions with ships (PAM);
 - earthquakes (PAM);
 - extreme weather (PAM);
 - helicopter crash (PAM);
 - hot surfaces:
 - frozen surfaces:
 - collapse of loads or unbalanced loads (PAM);
 - collapse of the structure (PAM);
 - people in contact with chemicals.

For major accident hazards/risks, a classification can be made according to type and location:

Risks associated with uncontrolled hydrocarbons:

- production manifold;
- wellhead, including flow pipes;
- well stations;
- risers/pipes;
- drilling and well operations

risks not associated with hydrocarbons:

- collision with ships;
- helicopter crash;
- collapse of loads or unbalanced loads;
- collapse of the structure, including due to earthquakes;
- process flame from the burner, fire caused by gas leakage. Specifically, below is a list of hazards identified for the activity

Specifically, below is a list of hazards identified for the activity in the offshore area of Romania, the Black Sea.

Hydrocarbons:

- crude oil in pumping;
- crude oil extracted with reduced pressure;
- associated petroleum gases (liquefied or in solution);
- hydrocarbons located (stored) in the reservoir;
- paraffin;
- gaseous hydrocarbons.

Explosives:

- substances that can cause detonation;
- traditional explosives.

Hazards associated with working under pressure:

- air under pressure;
- liquids under pressure;
- pressure vessels
- steam under pressure
- diving of maintenance and operating personnel.

Hazards associated with movement:

- land, naval, air transport;
- collision with other vessels;
- machinery with moving parts;
- hand tools that can cause cuts;
- transfer with personnel basket.

Hazards associated with environmental conditions:

- weather conditions;
- sea state:
- earthquake;
- corrosion of the structure of the facilities.

Other areas under which such specific risks can be identified would be: evacuation of personnel and equipment, medical issues, security, ergonomic issues, corrosive substances, biological hazards, toxic products, radiation, electricity, etc.

IV. ANALYSIS AND EVALUATION OF THE RISK IN THE OPERATION OF OFFSHORE INSTALLATIONS

If it were to happen, how serious would it be and what would be the chances of it happening again?

This question should be the starting point for the analysis process.

I will now highlight the quantitative and qualitative risk assessment methods.

As part of the general risk management process, quantitative analysis is a calculation process based on the data and information collected, with the aim of assessing the cost of risk in relation to the operation as accurately as possible.

It is very important that the data collected for performing the quantitative risk analysis are adequate and for this they must be studied over a sufficiently long period of time so as to cover various situations.

Since in this paper I will focus much of my attention on the fixed offshore installation, the Ana platform located in the Black Sea, let us imagine that in the last five starts of the process pump A located on the Ana jacket, it had a malfunction within eight hours of starting.

With this information, we can assume that the operators will understand that, without a countermeasure implemented, the next time they use the process pump A, there is a 100% chance that it will fail within the first eight hours of operation.

On the other hand, qualitative risk analysis is the process of evaluating the identified risk in terms of its severity and the likelihood of its consequences.

Qualitative risk analysis is a very useful defense tool available to the management team of an operation against risks.

It helps to eliminate potential doubts or uncertainties about the success of the operation, highlighting even risks that could cause less serious damage to the operation.

In other words, the more severe risks are targeted first so that the overall analysis is more efficient, allowing for better management of time and resources.

It is very important to understand what risk is, but especially to identify risks, to know them.

A simple definition of risk would be that it represents the possibility that something bad will happen.

In the following I will try to approach this knowledge from a quantitative point of view.

To achieve this goal, there are several steps to follow:

- 1. In the case of an offshore installation, we will inventory all tangible assets (machinery, tools, computers, etc.) but also intangible assets (patents, certifications, software, etc.) on board it.
 - 2. We will then assign a value to each of them.

As an example, a spare parts warehouse to be equipped with shelves, cabinets, etc. could cost relatively little but the parts and materials stored can be extremely valuable.

3. The risk exposure factor (FER) is calculated.

For this, all possible threats to each asset must be identified, which will help us understand how exposed each asset could be.

4. In fact, the exposure factor could be expressed as a percentage of loss.

V. RESULTS

This loss is specific to each asset considering a specific identified threat.

For example, in the case of a fire in the engine room of one of the diesel engines, a certain part of the neighboring equipment will suffer significant damage that could affect the operation taking place on the unit to a certain extent that can be expressed as a percentage.

This would be the exposure factor. The exposure factor is assigned to each asset for a single identified risk.

This factor will be small for assets that can be easily replaced.

The probability of single loss (PPU), can be calculated for an asset, for a risk associated with that asset.

It is calculated by the formula:

$$PPU = Asset Value (VB) x Exposure Factor (FER)$$
 (1)

and helps to better prioritize assets.

This way, the financial loss can be estimated each time a specific threat is associated with a specific asset.

1. Annual Occurrence Rate (AOR), identifies how often that specific threat associated with an asset can occur.

For example, how often can a storm occur with wind and waves close to the maximums recorded in the area where the facility is located?

Would it be possible to take into account the probability of such a storm if the facility were relocated?

If the facility is moved to another location, could there be other threats of a greater nature there?

For example, if the average over the last 50 years of occurrence of an extreme storm is 3/year, then the AOR is 3.

2. Calculate the annual loss probability (ALP).

PPA = Probability of One-Time Loss (PPU) x Annual Occurrence Rate (AOR) (2)

The annual loss probability (PPA) can help us understand how large the annual loss could be for a particular asset.

PPA helps us prioritize safety and backup measures, because now we know how much the loss will be for a particular asset and how often the associated risk will occur during a year.

3. The last step in the quantitative risk assessment is the cost-benefit analysis for any countermeasure being considered.

The calculation is done by first assessing how much each safety measure or countermeasure will cost, how much will it cost for the organization to have its own security team?

Then we subtract this cost from the PPA (annual loss probability).

If the result of this calculation is negative, then it is not financially reasonable to implement the countermeasures.

On the other hand, a positive result will show us how much it would be possible for the organization to save by implementing countermeasures that prevent a specific threat from affecting a particular asset.

Cost-benefit analysis (CBA) = PPA before countermeasures – PPA after countermeasures – Annual cost of countermeasures (ACC). (3)

As an example, let's imagine that we have a server worth 200,000 euros (VB).

A single specific threat or mismanagement (FER) could reduce this value by 10%, meaning that 20,000 euros (PPU) would be lost.

This is therefore the value of the loss once a year.

We can introduce certain countermeasures such as employee security awareness or strong passwords, which could reduce the threat.

We can also calculate how much it would cost to implement such countermeasures for that specific threat, on that server.

In other words, if we introduce the countermeasure, we could reduce the loss to, say, 10,000 euros.

If the cost of another countermeasure is 5,000 euros, then the value of the benefit is a positive value, that is, 5,000 euros.

$$PPU = VB \text{ x FER} = 200000 \text{ x } 10\% = 20000$$

$$Benefit \text{ value} = (20000 - 10000) - 5000 = 5000 \text{ euros}.$$
(5)

Obviously, at the level of an offshore installation, starting from such a model imagined on a very small scale, a complex calculation algorithm can be imagined, taking into account the complexity of such an installation.

VI. CONCLUSION

As a conclusion to this paper, I mention that there are gaps in Romanian legislation, but the experience of European countries and of professional and technological risk assessors has led to the mitigation of dangers and minimized the effects of possible incidents.

REFERENCES

- [1] R. S. Mohammad, D. Stoianovici, T. Chis, D. Iancu, (2023), *Neuronal Moddeling of Water Properties on Oil Field*, International Journal of Engineering Research and Reviews, ISSN 2348-697X (Online), Vol. 11, Issue 3, July 2023 September 2023, Page No: 48-58, https://www.researchpublish.com/papers/neuronal-moddeling-of-water-properties-on-oil-field,
- [2] A.G.H.A., Mosleh, D. Iancu., T. Chiş, (2025), Modeling the Effects of Accidents on Employees During Blowout Preventer Testing, ESP-JETA ESP Journal of Engineering & Technology Advancements ISSN: 2583-2646 / Volume 5 Issue 1 January 2025 / Page No: 30-40 Paper Id: JETA-V5I1P104 / Doi: 10.56472/25832646/JETA-V5I1P104,
- [3] D.Iancu, , R.Rădulescu, Şt Pelin, *Analysis of safety in operation of Romanian marine platforms* 75 Years of Energy and Performance in Education and Research 2023 Renewable Versus Fossil Fuels. Global Energy Perspectives, Ploiesti 9.11.2023, Book of abstracts, Editura Universității Petrol-Gaze din Ploiești, 2023, ISBN 978-973-719-887-7,

High-Performance and Durable DSSCs with PtNP/PANI/g-CN Nanocomposites: Moving Beyond Traditional Platinum Electrodes

Mücella ÖZBAY KARAKUŞ^{1*}

¹Department of Computer Engineering, İzmir Bakırçay University, Türkiye (ORCID: 0000-0003-0599-8802) *(mucella.ozbaykarakus@bakircay.edu.tr)

ABSTRACT

This study presents the development and application of a nanocomposite counter electrode composed of platinum nanoparticles (PtNP), polyaniline (PANI), and graphitic carbon nitride (g-CN) for dye-sensitized solar cells (DSSCs). The primary aim is to improve efficiency, stability, and costeffectiveness by offering a viable alternative to conventional platinum (Pt) fabricated PtNP/PANI/g-CN electrodes. **DSSCs** with demonstrated impressive initial performance, achieving an open-circuit voltage (V_{OC}) of 720 mV, a short-circuit current density (J_{SC}) of 22 mA/cm², and a power conversion efficiency (PCE) of 10.05%. These values exceeded those of standard Pt-based cells (V_{OC}: 720 mV, JSC: 19 mA/cm², PCE: 9.14%). A key advantage of the PtNP/PANI/g-CN electrodes lies in their long-term durability. Over a 12-month testing period, including weekly and monthly measurements, these DSSCs retained 80% of their initial efficiency, with V_{OC}, J_{SC}, and PCE values stabilizing at 708 mV, 17 mA/cm², and 7.98%, respectively. In contrast, Pt-based DSSCs declined significantly, dropping to 583 mV, 12 mA/cm², and a PCE of just 4.32%. Electrochemical impedance spectroscopy (EIS) confirmed the improved charge transfer characteristics of the composite electrodes, as evidenced by reduced series resistance and smaller semicircle diameters in Nyquist plots. These findings demonstrate that PtNP/PANI/g-CN nanocomposites offer not only superior initial performance but also exceptional long-term stability, positioning them as a promising, low-cost alternative for future DSSC technologies.

Keywords – DSSC; Renewable Energy Systems; Solar cells; PtNP/PANI/g-CN nanocomposite; Counter electrode

I. Introduction

The rapid Rapid population growth, along with technological and industrial advancements, has significantly increased the demand for clean and renewable energy sources [1-3]. Recently, solar energy has emerged as a prominent solution to overcome the current energy crisis, owing to its natural abundance, non-polluting characteristics, and status as a clean and renewable energy source. Due to these advantages, solar energy is increasingly preferred over conventional fossil fuels, which are toxic and costly, and thus has become an intense subject of research as a cost-effective, environmentally friendly, and sustainable energy generation method [4, 5].

In the direct conversion of solar energy into electricity, next-generation photovoltaic devices such as dye-sensitized solar cells (DSSCs) [6] perovskite solar cells (PSCs) [7], and organic solar cells (OSCs) [8] are extensively studied due to their rapidly increasing power conversion efficiencies (PCEs), low environmental impact, excellent flexibility,

relatively simple fabrication processes, and low production costs [9, 10]. Although the PCEs and sustainability of these next-generation solar cells are not yet sufficient for commercialization compared to conventional silicon solar cells [11], the moderate PCE values of silicon cells, the requirement for clean-room production conditions, the high manufacturing costs, and the ability to generate energy only under direct, clear, and unobstructed sunlight necessitate the development of alternative energy conversion technologies [12].

Among new-generation solar cells, DSSCs are particularly notable for commercialization due to their relatively low production cost and easy fabrication compared to other types [13]. A standard DSSC structure consists of a semiconductor layer (usually TiO₂) coated with a dye as the photoanode, a counter electrode, and a redox electrolyte typically containing a triiodide/iodide couple [14].

As shown in Fig. 1, the sensitizing dye attached to the TiO₂ film in a single layer absorbs incoming light and generates electrons that are injected into the conduction band of the semiconductor oxide. When light with a wavelength matching the band gap of the dye strikes the dye, it is absorbed, causing the electrons in the dye to be excited to an electrically high-energy state. This process results in the formation of electron-hole pairs. The excited electrons are transferred to TiO₂, initiating a redox cycle that continues as long as illumination is maintained, resulting in a continuous electron flow within the structure. In this way, photon energy is converted into electric current [15].

After the counter electrode performs charge separation in the cell, it is necessary for it to catalytically complete the missing charge of the electrolyte. Furthermore, the counter electrode must be resistant to the corrosive electrolyte [16].

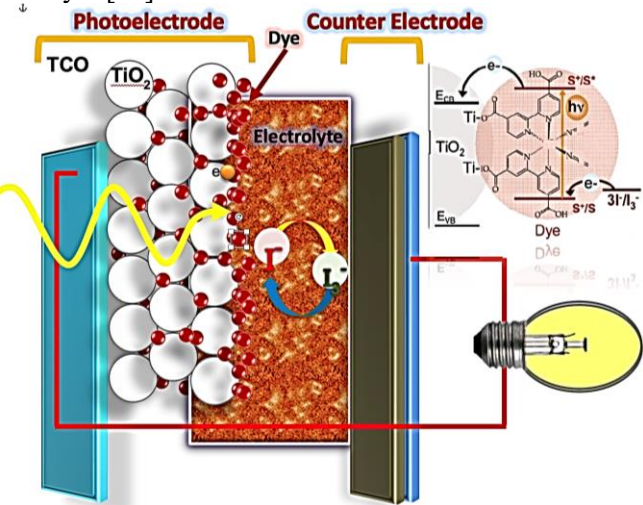


Fig. 1 The structure and operating principle of dye-sensitized solar cells

The counter electrode plays a critical role in DSSCs by collecting electrons and catalyzing the reduction reaction [13], thus being an indispensable component of the device structure. An efficient counter electrode must possess low charge transfer resistance, high electrical conductivity, excellent electrocatalytic activity, and high reflectivity [17, 18]. These properties enable the efficient transfer of electrons from the external circuit to the electrolyte, catalyze the reduction of I₃-/I- [17, 18], and enhance solar light utilization by reflecting unabsorbed light back to the sensitizer [19].

Traditional conductive glasses such as indium tin oxide (ITO) or fluorinedoped tin oxide (FTO), which are catalyst-free, provide low reduction rates when used as substrates for counter electrodes in DSSCs. Therefore, they require coating with catalytically active materials to accelerate the reaction [20]. In this context, platinum (Pt) films prepared on transparent conductive substrates are widely preferred due to their excellent conductivity and high electrocatalytic activity [21, 22]. However, Pt is a rare and expensive metal making large-scale production costly and commercialization. Furthermore, Pt suffers from corrosion and dissolution over time due to the aggressive I₃-/I⁻ redox couple [25], causing significant instability issues in DSSC counter electrodes [26, 27]. Therefore, developing alternative counter electrode materials with low cost, excellent stability, and comparable performance to Pt is seen as crucial [19] and researchers are focusing on finding suitable substitutes [13].

Recently, the discovery of carbon-based materials [28], polymers [13], and transition metal compounds [29] as Pt-like catalysts for DSSCs has sparked increased interest in alternative materials. Inspired by this, conductive polymers such as polyaniline (PANI) [30] and polypyrrole (PPy) [31], metal sulfides like cobalt sulfide (CoS₂) [32] and nickel sulfide (NiS₂) [33], metal oxides such as tungsten trioxide (WO₃) [34] and molybdenum trioxide (MoO₃) [35], and carbon-based materials like graphene [36, 37], carbon nanotubes (CNTs) [38, 39], carbon nanofibers (CNFs), and graphitic carbon nitride (g-CN) [40] have been proposed as promising candidates to replace Pt in DSSC counter electrodes.

Among these, carbon-based materials are preferred due to their high conductivity, stability, and catalytic activity [41]. However, their conductivity and catalytic activity are still relatively inferior to Pt [42]. Recent reports suggest that nitrogen (N) doping into the carbon (C) framework enhances the electrocatalytic activity, stability, and surface hydrophilicity of carbon-based materials [43]. Among carbon-based materials, g-CN, a naturally nitrogen-containing carbon material, is particularly attractive due to its low cost (owing to the abundance of C and N in nature) and high corrosion resistance compared to Pt. Moreover, g-CN is promising due to its ease of preparation, non-toxicity, stability [44, 45], and outstanding thermal and chemical properties [19]. Furthermore, g-CN

exhibits broad potential in providing multiple electroactive sites to promote I_3^-/I^- reduction [46, 47].

Graphitic carbon nitride (g-CN) is a two-dimensional (2D), n-type, metalfree polymeric semiconductor, where carbon and nitrogen atoms are connected by π -conjugated bonds. The precursors for synthesizing g-CN are typically nitrogen-rich and oxygen-free materials containing C-N bonds. Its unique properties, such as high stability in thermal and chemical environments and low-cost large-scale production, make g-CN a favorable candidate for preparing nanocomposites [13, 48, 49].

Additionally, g-CN possesses a moderate bandgap of ~2.7 eV, enabling the absorption of not only ultraviolet (UV) light but also part of the visible spectrum, particularly the blue region, thus increasing the photogeneration rate of charge carriers [50]. Therefore, utilizing g-CN as an alternative or additive to conventional solar cell materials could significantly enhance the cost-effectiveness, eco-friendliness, stability, and performance of next-generation devices [19].

Despite these advantages, the application of g-CN in next-generation solar cells remains at an early developmental stage, with unsatisfactory results reported thus far. This is attributed to factors such as low crystallinity, high defect density, small specific surface area, insufficient active sites, high charge carrier recombination rates, low electrical conductivity, and inadequate optical absorption in the visible region [51-52]. The low electrical conductivity of g-CN restricts electron transfer from the counter electrode to the electrolyte, resulting in high interfacial resistance and low catalytic activity [19].

However, overcoming these issues is possible through strategies such as morphology engineering to create two-, one-, or zero-dimensional (2D, 1D, 0D) nanostructures from bulk g-CN, producing nanocomposites with appropriate optoelectronic properties, and elemental doping [53-54]. For instance, g-CN is often combined with highly conductive materials to enhance its electrochemical performance [19].

Conductive polymers like PANI [43], carbon black (CCB) [47], multi-walled carbon nanotubes (MWCNTs) [46], and graphene [55] have been employed to fabricate Pt-free composite counter electrodes in DSSCs. These composites provide a high specific surface area and continuous charge transport pathways, thus reducing series resistance at the counter electrode/redox electrolyte interface and improving charge transfer. Consequently, they exhibit higher electrocatalytic activity and electrical conductivity compared to pure g-CN electrodes.

Summarizing the findings: PANI/g-CN hybrids synthesized by in situ polymerization of aniline monomers on g-CN under ultrasonic irradiation yielded a PCE of 1.79% [43]. In another study, a g-CN/MWCNT composite achieved a PCE of 6.34% [46]. CCB and graphene-based composites reached 5.09% [42]. and up to 7.46% [55] respectively. Thus, supporting

pure g-CN with conductive materials is a promising strategy. Nevertheless, these PCE values still fall short of the ~12% achieved with Pt-based DSSCs [56].

Moreover, based on current findings, completely eliminating Pt appears impractical; instead, incorporating Pt in small amounts to reduce costs and prevent corrosion is a more realistic approach. Additionally, metals play a critical role in enhancing the catalytic activity of g-CN. Its unique structure, rich in nitrogen lone pairs, facilitates efficient metal loading, which can modify its electronic structure and improve photocatalytic performance [57]. Consequently, research on metal/g-CN composites has become increasingly popular.

Pan et al. [58] theoretically predicted through primary calculations that metal atoms (such as Pd, Pt, etc.) could be incorporated into g-CN nanotubes (NTs). The incorporation of metal atoms effectively enhances the photoinduced carrier mobility of g-CN, narrows its bandgap, and further extends its visible light response range. Additionally, due to the interaction between negatively charged nitrogen atoms in g-CN and cations, g-CN exhibits a strong ability to capture cations. The integration of metals into the g-CN framework also enables electron enrichment in g-CN, thereby significantly improving its catalytic capabilities [57].

Shiraishi et al. [59] successfully deposited platinum nanoparticles (NPs) onto the surface of g-CN through a high-temperature annealing process, resulting in tightly bound Pt NPs on the g-CN surface. This strong interaction notably facilitated the seamless migration of photoinduced electrons from g-CN to the Pt NPs. As a result, Pt/g-CN was employed as an efficient photocatalyst for hydrogen production, achieving high catalytic activity. The addition of Pt in NP form not only significantly reduced costs but also improved electrocatalytic activity.

Nanoparticles, typically ranging in size from 1 to 100 nm, may exhibit size-dependent unique physical and chemical properties [60]. Owing to their increased surface area, nano-sized particles show distinctive characteristics. Among these, noble metal nanoparticles such as Au, Ag, Pt, and Pd display remarkable properties and are extensively utilized in electrocatalysis, antibacterial applications, electrochemical sensing reactions, biotechnology, and electronics [61]. Notably, Pt, with a high melting point of 1769 °C, is utilized for its resistance to corrosion and chemical attack, and acts as an efficient catalyst in various hydrogenation reactions (e.g., hydrogenation of o-chloronitrobenzene and cinnamaldehyde) [61].

Although the incorporation of Pt NPs enhances the conductivity and electrocatalytic activity of g-CN and provides partial corrosion resistance, further improvements are necessary to maximize conductivity and prevent corrosion, especially for DSSC (Dye-Sensitized Solar Cell) applications. Preventing the corrosion of metal components within the DSSC structure is critical. Consequently, researchers are not only focusing on increasing PCE

(Power Conversion Efficiency) but also developing multifunctional, adjustable corrosion-inhibiting materials with broad application potential. These materials must meet durability, stability, chemical resistance, and optical activity requirements.

In this context, electroconductive polymers (ECPs) have attracted attention. Among ECPs, polyaniline (PANI) stands out due to its catalytic and electrochemical performance. PANI's highly branched structure, excellent processability, high conductivity, large surface area, and chemical stability make it attractive for applications such as water purification and corrosion protection [62].

When doped with inorganic acids (e.g., hydrochloric acid) or organic acids (e.g., sulfosalicylic acid), the emeraldine base (EB) form of PANI can be easily converted into the emeraldine salt (ES) form, exhibiting increased conductivity due to protonation of the imine nitrogen atoms [63]. The partially oxidized ES form of PANI is also catalytically active, with low bandgap energy (Eg) and high electron transfer performance, attributed to the formation of polaron and bipolaron bands [62]. In addition, the redoxactive structure of PANI, consisting of oxidation (benzoquinone) and reduction (benzene) units, as well as its excellent environmental stability and π - π conjugated system, makes it suitable for corrosion-resistant coatings and modification of semiconductor photocatalytic activity [64, 65].

Beyond these applications, PANI is considered the most notable material among conductive polymers to potentially replace Pt as the counter electrode in DSSC devices. Its simple synthesis, significant catalytic activity, and good environmental stability make it an attractive alternative. However, PANI, being an organic semiconductor, has inherently limited charge transport capability. Thus, pure PANI still falls short of competing with Pt in terms of electrocatalytic activity and long-term stability, resulting in lower energy conversion efficiencies. Therefore, combining PANI with carbon-based materials or other nanomaterials is proposed as an effective strategy to enhance its conductivity and improve the overall performance of DSSC systems [66].

While this study serves multiple objectives, its principal aim is not to entirely replace the Pt counter electrode with an alternative material, but rather to enable the cost-effective fabrication of dye-sensitized solar cells (DSSCs) by reducing the amount of Pt used—without compromising its exceptional properties—thereby maintaining high catalytic activity and electrical conductivity. Given that the corrosive I₃-/I- redox electrolyte in DSSC configurations causes corrosion and dissolution of the Pt counter electrode, leading to reduced long-term stability and significant economic losses, mitigating these effects is critical for sustained device performance.

In this context, the rational selection of materials and an accurate understanding of bandgap engineering are pivotal for the development of efficient electrocatalysts. As evidenced in the current literature, the complete exclusion of Pt from DSSC systems remains unfeasible under present technological constraints. Although corrosion of the Pt counter electrode negatively impacts the stability of DSSCs, no alternative material has yet demonstrated a comparable combination of electrocatalytic activity, electrical conductivity, and corrosion resistance against the $\rm I_3^-/I^-$ redox couple.

Therefore, to address these interdependent challenges without compromising device efficiency, there is an urgent need for a smart counter electrode coating that can suppress corrosion while preserving catalytic performance. Within this framework, the present study proposes the design and application of a PtNP/PANI/g-CN composite structure aimed at enhancing the long-term stability of the Pt counter electrode and overcoming corrosion-related limitations in DSSCs.

Individually, each component—Pt, g-CN, and PANI—offers distinct advantages and inherent drawbacks when employed as counter electrode materials. While converting Pt into nanoparticle form (PtNPs) may effectively reduce both cost and corrosion, the accompanying decrease in Pt content could impair photocatalytic efficiency. The incorporation of graphitic carbon nitride (g-CN), which exhibits strong electrocatalytic activity, can mitigate this issue by facilitating the I₃-/I- reduction reaction and thereby enhancing short-circuit current. However, g-CN suffers from high charge carrier recombination rates and inherently low electrical conductivity. These limitations can be addressed by integrating it with PtNPs, which possess excellent electrical conductivity. Yet, due to the inadequate optical absorption of PtNP and g-CN in the visible spectrum, the addition of polyaniline (PANI)—a dark blue conductive polymer—can further augment the system by improving corrosion resistance, enhancing conductivity, and increasing light absorption. Moreover, the PtNP/PANI/g-CN composite is expected to increase the effective surface area, thereby further contributing to the overall device performance. The synergistic interplay among these three materials allows each to offset the limitations of the others, resulting in a structurally and functionally optimized counter electrode.

Previous studies have also demonstrated that power conversion efficiency (PCE) in DSSCs does not scale linearly with the thickness of the Pt film. In fact, reasonably high efficiencies can be achieved using ultrathin Pt layers (e.g., ~2 nm), suggesting that reductions in Pt content can partially alleviate production costs [25]. However, at such thicknesses, the Pt film becomes nearly transparent, limiting its ability to reflect photons back into the photoactive layer, which reduces light harvesting efficiency. Additionally, the reduced surface area associated with thinner films contributes to a decline in PCE. Conversely, the incorporation of PtNPs—as opposed to the use of standalone PANI or g-CN—offers potential advantages by increasing

both surface area and photocatalytic activity while concurrently enhancing corrosion resistance [61].

The synthesis of two-dimensional graphitic carbon nitride (g-CN) as a multifunctional protective layer in DSSCs has been reported due to its high nitrogen content and enhanced electrocatalytic activity, which improves the I₃-/I- reduction reaction and consequently increases the short-circuit current [43]. However, the intrinsic electrocatalytic performance of g-CN is limited by its poor electrical conductivity. To overcome this limitation, the incorporation of conductive materials such as metal dopants, conducting polymers, or carbon black composites into the g-CN matrix has been proposed as an effective strategy to facilitate electron transport and improve the electrocatalytic activity of g-CN [43].

Among the available options, combining g-CN with polyaniline (PANI) offers the advantage of not only enhancing electrical conductivity but also extending the material's optical response in the visible light region. Moreover, given that the electrical conductivity of PANI can be further improved by hybridizing it with conductive nanomaterials, the inclusion of platinum nanoparticles (PtNPs) into the system is expected to provide additional benefits. Specifically, PtNPs can enhance the electrocatalytic activity of PANI and concurrently contribute to corrosion resistance within the electrode architecture. This is because the catalytic activity of Pt can be maximized when employed in nanoparticulate form, owing to its high surface area-to-volume ratio and distinctive surface plasmon resonance properties [43].

Furthermore, PtNPs have been shown to significantly improve the photo-induced charge carrier mobility of g-CN, reduce its bandgap, and broaden its visible light absorption range. Consequently, the integration of PtNPs helps compensate for the inherently low electrical conductivity of g-CN, thereby restoring and even enhancing its electrocatalytic activity [48]. This approach not only facilitates a substantial reduction in overall material costs due to the decreased amount of Pt required but also enables the recovery of electrocatalytic performance, which is crucial for high-efficiency DSSC operation.

In the PtNP/g-CN composite structure, the incorporation of metal nanoparticles has the potential to alter the electronic structure of the semiconductor photocatalyst—particularly the band structure—thereby improving photocatalytic performance. Additionally, polyaniline (PANI), due to its excellent processability, high electrical conductivity, large surface area, and chemical stability [62] plays a critical role in enhancing electron transport. Within the composite matrix, PANI contributes by providing a high specific surface area and continuous charge transport pathways, which reduces the series resistance at the interface between the counter electrode and the redox electrolyte, ultimately facilitating more efficient charge transfer.

Compared to pure g-CN, such a composite electrode structure exhibits significantly improved electrocatalytic activity and electrical conductivity. This improvement is crucial, as pristine g-CN suffers from several intrinsic limitations, including low specific surface area, high charge carrier recombination rate, poor electrical conductivity, and insufficient optical absorption in the visible region. These drawbacks result in high interfacial resistance at the electrode/electrolyte interface during electrochemical reactions, thereby reducing catalytic activity [19]. To overcome these issues, the integration of PtNPs and PANI into the g-CN framework is proposed, enabling the formation of composite materials with tailored optoelectronic properties.

In summary, the primary objective of this study is to develop a novel PtNP/PANI/g-CN composite counter electrode for DSSCs that addresses the critical challenges of corrosion and high production cost. This composite structure is expected to offer a more efficient, cost-effective, and sustainable solution for solar energy conversion, thereby removing key obstacles to the commercialization of DSSC technology. By introducing an innovative approach to counter electrode design, this project aims not only to enhance DSSC performance and economic viability but also to contribute to the broader adoption of renewable energy technologies. The successful implementation of this composite system could mark a significant advancement in DSSC development, potentially reducing reliance on fossil fuels and conventional silicon-based solar cells.

II. MATERIALS AND METHOD

As part of the project, coatings with dual-function anti-corrosive and electro-photo catalytic activity will be prepared using Pt nanoparticles combined with PANI and g-CN. These coatings will be used as the back electrode in DSSC structures. The performance evaluations of the coatings will be conducted based on electrical and electrochemical test results, including short-circuit current (ISC), open-circuit voltage (VOC), power conversion efficiency (PCE), as well as electrochemical impedance spectroscopy (EIS) measurements.

A. g-CN Production

Initially, 24 grams of melamine powder was placed into a quartz boat and inserted into a tubular furnace. The system was purged and maintained under a continuous nitrogen gas flow to ensure an inert atmosphere throughout the process. The temperature of the furnace was gradually increased to 600 °C at a controlled heating rate of 1 °C per minute. Upon reaching 600 °C, the sample was held at this temperature for 3 hours to allow complete thermal polymerization and condensation of the melamine into graphitic carbon nitride (g-CN). After the dwell time, the furnace was allowed to cool naturally to room temperature without disrupting the nitrogen environment, thus preventing any oxidation or contamination of the product.

The resulting material, which appeared as a pale yellow solid, was collected and ground thoroughly using a ceramic mortar and pestle to obtain a fine powder. The final mass of the synthesized g-CN powder was measured to be 9.82 grams. This procedure yielded high-purity g-CN with a layered structure, making it suitable for further applications in the fabrication of composite electrodes and photocatalytic materials.

B. Synthesis Process of Nanoparticle-Modified PANI

The g-CN production was carried out via a one-step polymerization reaction. In the synthesis process, the materials were combined in the sequence described below. 5 g of melamine was calcined in an atmosphere of nitrogen gas at 600 °C for 6 hours (at a heating rate of 2°C/min). The yellow-colored solid product, approximately 3 g in weight, was obtained and then powdered to produce g-CN. Following this, 0.01 g of the synthesized g-CN powder was added to 10 mL of distilled water and subjected to sonication for 5 minutes. Subsequently, 1 mL of the homogeneous g-CN solution was added to 30 mL of a 7 M NaOH solution, along with 0.5 mL of K₂PtCl₄ at two different molarities (0.1 M and 0.2 M). The reaction was then stirred magnetically under ambient conditions.

To prevent the crystallization of platinum hydroxide, the K₂PtCl₄ solution was added all at once. After 30 minutes of stirring, the mixture was cooled to 0 °C, and 0.5 mL of aniline monomer was added. The color change (from brown to dark green) was observed, indicating the reaction between the aniline monomer and Pt₂⁺. The reaction was allowed to continue for another 30 minutes to complete the reaction between the aniline monomer and Pt₂⁺. Afterward, 10 mL of L-cysteine at different molarities (0.5 M, 0.8 M, and 1 M) was added to the reaction mixture, and the temperature was gradually increased to 60 °C at a heating rate of 1.5 °C/min.

L-cysteine, which is a ligand that binds to Pt₂⁺ through a coordination bond, was used as a reducing agent to enhance the reduction efficiency of Pt₂⁺ precursors to metallic Pt [67]. To obtain the optimum value and best performance, a total of six different types of nanocomposite structures were synthesized by varying the amounts of K₂PtCl₄ and L-cysteine, optimizing the synthesis process.

The reaction was allowed to continue for an additional 60 minutes to complete. Afterward, the reaction mixture was centrifuged at 4000 rpm for 20 minutes to separate the product from the solution. The resulting product was then dried in a vacuum oven at 60 °C for 24 hours, yielding 8 g of the powdered nanocomposite.

The prepared nanocomposite powder was dissolved in 1-Methyl-2-Pyrrolidone to achieve a concentration of 100 mg/10 mL and was then used in the coatings.

C. Counter Electrode and DSSC Production Process

Commercially purchased Fluorine-doped Tin Oxide (FTO) glass substrates (7 Ω /cm²) were first washed with detergent, then rinsed with ultra-pure water, and dried under nitrogen gas. For the electrophoretic deposition, the PtNP/PANI/g-CN solution prepared with 1-Methyl-2-Pyrrolidone, as described earlier, was used. FTO-coated glass substrates were placed in parallel within the solution, and a constant voltage of 200 V was applied for 2 hours using a power supply to complete the film deposition on the FTO surface.

After the cleaning procedure, the FTO-coated glass substrates were treated with TiO₂ paste (Ti-Nanoxide D/SP), applying a 5x5 mm² square active area onto the FTO by using the doctor blade technique. Following the preparation of the photoanode, the substrates were gradually heated before TiCl₄ treatment, and the first sintering step was completed at 450°C for 30 minutes. A 40 mM aqueous solution of TiCl₄ was prepared and heated to 70°C. The TiO₂ photoelectrodes were then treated with TiCl₄ for 30 minutes. Afterward, the photoelectrodes were removed from the solution, washed with deionized water and ethanol, and subjected to a second sintering process, where they were gradually heated again at 450°C for 30 minutes.

After the sintering process, the photoelectrodes were allowed to cool down to approximately 50-60°C. The photoelectrodes were then immersed in a 0.5 mM ethanol solution of Ruthenizer 535-bisTBA (N719) dye sensitizer, prepared with 10 times the mass of chenodeoxycholic acid, and kept in the dark for 18 hours at room temperature.

The prepared back electrodes were then combined with the photoelectrodes using a sealing gasket of 60 µm thickness, and the sandwich assembly of the two electrodes was injected with HI-30 liquid electrolyte, containing the iodide/triiodide (I₃-/I-) redox couple. To minimize experimental errors, three samples were prepared for each series, and the experiments were conducted with triplicate samples...

IV. EXPERIMENTAL RESULTS

A. Performnace Parameters of the Base Structured DSSCs

In this research the characterization of the produced DSSCs was initially carried out by examining the parameters that make up the structure. Subsequently, a series of experiments were conducted to determine the photovoltaic performance characteristics, and the obtained results were evaluated.

The results obtained showed in Table 1 and Fig. 2, that in DSSCs using a PANI back electrode, a higher current density was achieved compared to DSSCs using a Pt back electrode. However, due to the relatively lower open-circuit voltage (VOC), the efficiency was also relatively lower. In DSSCs produced with a PANI back electrode, the VOC value was the lowest, while ISC was the highest. On the other hand, when g-CN was used, the opposite trend was observed, with the highest VOC value but the lowest ISC among

all structures. Therefore, combining these two structures is likely to result in an average value. However, the addition of PtNP to the structure is expected to significantly improve the current-voltage performance and maximize the PCE value. This is because PtNPs play a role in increasing conductivity and reducing charge transfer resistance, while g-CN provides active sites for ion adsorption in the synthesized nanocomposite structure, and PANI supports Pt by initiating redox reactions between the electrolyte and PANI.

Table 1. Experimental performance parameters for Pt, PANI and g-CN counter electrode based DSSCs

Counter Electrode	VOC (mV)	JSC (mA/cm2)	FF (%)	μ(%)	
Pt	720	19	52	9.14	
PANI	666	16.2	58	6.3	
g-CN	710	11.87	54	4.7	

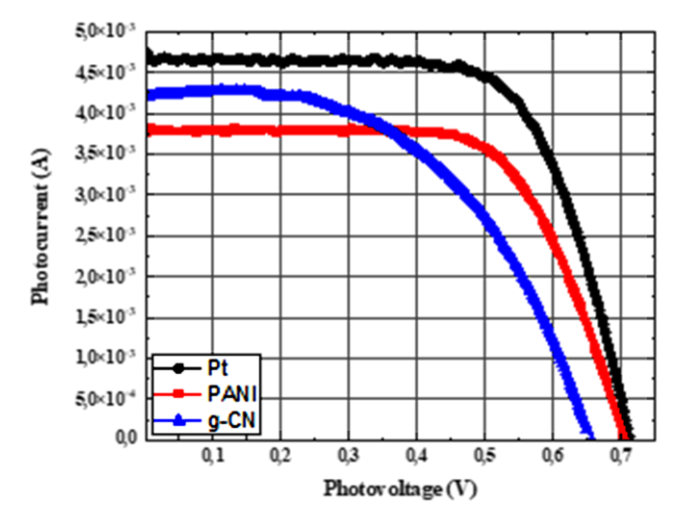


Fig. 2 Photovoltage vs. photocurrent graphs of base structured dye-sensitized solar cells

The photovoltaic performance parameters of the DSSCs fabricated with different counter electrodes — namely Pt, PANI, and g-CN are summarized in Table 1. Analyzing the open-circuit voltage ($V_{\rm OC}$), short-circuit current density ($J_{\rm SC}$), fill factor (FF), and power conversion efficiency (η), several important trends can be identified.

The conventional Pt counter electrode exhibits the highest overall performance among the tested electrodes, with a $V_{\rm OC}$ of 720 mV, a $J_{\rm SC}$ of 19 mA/cm², a FF of 52%, and a maximum power conversion efficiency of 9.14%. This outcome aligns with Pt's well-established superior catalytic activity and excellent electrical conductivity, enabling efficient charge transfer at the counter electrode/electrolyte interface.

On the other hand, when PANI is employed as the counter electrode, the device shows a noticeable decrease in $V_{\rm OC}$ (666 mV) and $J_{\rm SC}$ (16.2 mA/cm²) compared to Pt, but an improvement in the fill factor (58%). Despite the higher FF, the overall efficiency (η) drops to 6.3%. This behavior can be attributed to PANI's good conductivity and flexible structure, which facilitate charge transport; however, its catalytic activity toward the I_3 -/I-redox couple is inherently lower than that of Pt, thus resulting in reduced voltage and current density.

Meanwhile, the DSSCs based on g-CN electrodes present a relatively high $V_{\rm OC}$ of 710 mV — close to that of Pt — but suffer from a significantly reduced $J_{\rm SC}$ (11.87 mA/cm²) and a lower FF (54%), culminating in a modest PCE of 4.7%. These results are consistent with the known characteristics of g-CN: while it provides a favorable energy band structure and a relatively high photovoltage, its low electrical conductivity and high recombination rates limit efficient charge transport and current generation.

Fig. 3 depicts the independently determined I-V curves of PtNP/PANI/g-CN and Pt counter electrode based DSSCs. The study highlights that PtNP/PANI/g-CN exhibited a maximum efficiency of 10.05%, surpassing Pt, which achieved 9.14%. These results underscore significant advancements in dye-sensitized photovoltaic technology, demonstrating the effectiveness of PtNP/PANI/g-CN counter electrode in enhancing device efficiency. The findings suggest promising prospects for further optimizing DSSCs and advancing their performance in photovoltaic applications.

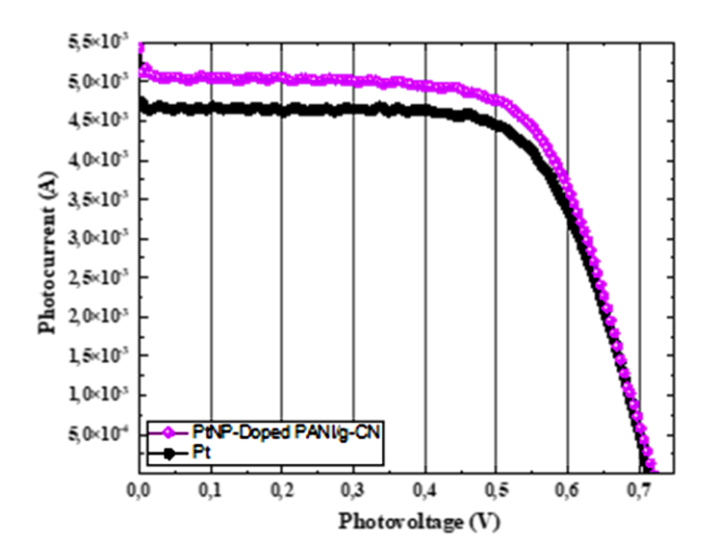


Fig. 3 Photovoltage vs. photocurrent comparison of the Pt and PtNP/PANI/g-CN counter electrodes for dye sensitized solar cells

B. Long-term stability Tests

A key distinguishing feature of the PtNP/PANI/g-CN composite electrodes is their exceptional long-term stability under operational conditions. To rigorously evaluate their durability, systematic stability assessments were conducted over a twelve-month period, with performance metrics recorded at both weekly and monthly intervals and the results are shown in Table 2 and Fig 4.

Counter Electrode	V _{OC} (mV)		J _{SC} (mA/cm ²)		FF (%)		μ(%)	
	Day	Day	Day	Day	Day	Day	Day 1	Day
	1	365	1	365	1	365		365
Pt	720	583	19	12	52	50	9.14	4.32
PtNP/PANI/g-	720	708	22	17	66	61	10.05	7.98
CN								

Table 2. Experimental performance parameters of DSSCs

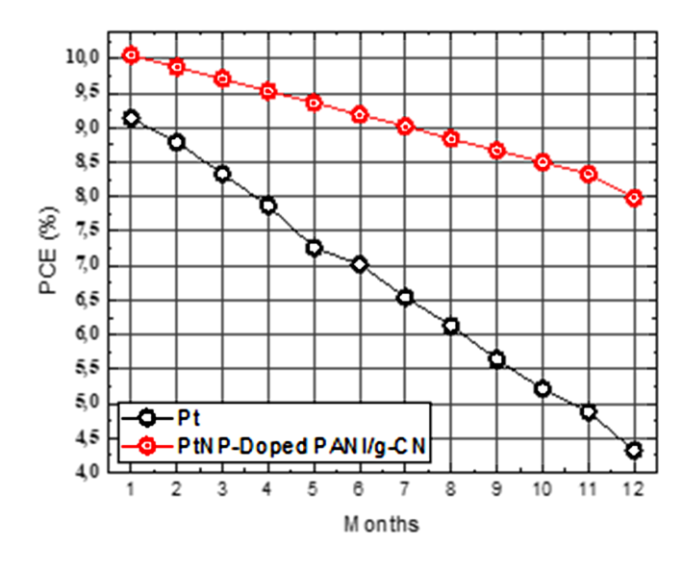


Fig. 4 One-year monthly stability analysis of the power conversion efficiency of DSSCs (Pt (blue) and PtNP/PANI/g-CN (red))

The results clearly demonstrate that DSSCs incorporating PtNP/PANI/g-CN maintained approximately 80% of their initial photovoltaic efficiency after one year of continuous evaluation. Specifically, these cells retained an open-circuit voltage ($V_{\rm OC}$) of 708 mV, a short-circuit current density ($J_{\rm SC}$) of 17 mA/cm², and a power conversion efficiency (PCE) of 7.98%.

In sharp contrast, reference DSSCs employing conventional platinum (Pt) electrodes exhibited significant performance deterioration over the same period. Their V_{OC} dropped to 583 mV, J_{SC} decreased to 12 mA/cm², and PCE was reduced to 4.32%, highlighting the inherent limitations of bare Pt

electrodes when exposed to the corrosive I₃-/I⁻ redox electrolyte environment. These comparative results underscore the critical advantage offered by the PtNP/PANI/g-CN composite, not only in mitigating corrosion-related degradation but also in maintaining efficient charge transfer dynamics at the electrode/electrolyte interface.

C. EIS Analysis Results of DSSCs

The Nyquist plots of the DSSCs were obtained using a VersaSTAT 3 Potentiostat/Galvanostat under dark conditions, at room temperature, and within a Faraday cage. An AC oscillator signal with an amplitude of 10 mV was applied, and the frequency range was set between 10 mHz and 1 MHz for all samples. From the Nyquist plots, the equivalent circuit parameters of the DSSCs were extracted and presented in Fig. 5.

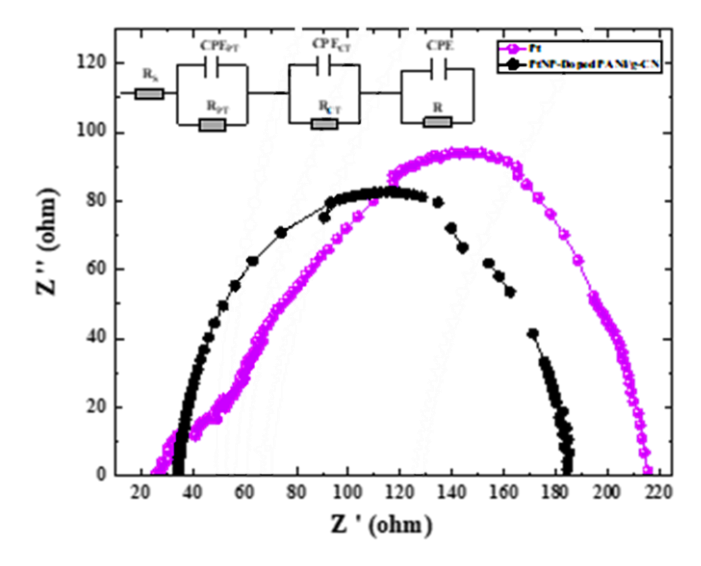


Fig. 5. Nyquist plots of the Pt and PtNP/PANI/g-CN counter electrodes for dye sensitized solar cells

As illustrated in Fig. 5, the Nyquist diagrams exhibit three distinguishable semicircles. The first semicircle in the high-frequency region corresponds to the charge transfer resistance (Rct) at the counter electrode. The second semicircle, located in the middle-frequency range, is associated with the resistance at the TiO₂/dye/electrolyte interface (Rpt), while the third semicircle in the low-frequency region represents the diffusion process within the electrolyte.

Charge transfer parameters were derived by fitting the Nyquist plots using the Z-View software, based on the equivalent circuit model depicted in the inset of Fig. 4. A close examination of Fig. 5 reveals that the DSSC with the PtNP/PANI/g-CN based counter electrode exhibits the lowest charge transfer

resistance (Rct) and the lowest series resistance among all the tested configurations, highlighting its superior electrical performance.

V. RESULTS AND DISCUSSION

This study aimed to investigate the influence of counter electrode materials—both in their pure and composite forms—on the photovoltaic performance of dye-sensitized solar cells (DSSCs). In particular, a novel composite material, PtNP/PANI/g-CN, which has not previously been reported in the DSSC literature, was synthesized and implemented as a counter electrode. The photovoltaic characteristics of the fabricated DSSCs were systematically evaluated and compared to standard counterparts employing conventional Pt, PANI, and g-CN electrodes.

Among the most notable features distinguishing the PtNP/PANI/g-CN composite electrodes from traditional materials is their outstanding long-term operational stability. To rigorously assess this property, a series of extended stability tests were carried out over a 12-month period, with data collected at both weekly and monthly intervals. The DSSCs incorporating PtNP/PANI/g-CN electrodes retained approximately 80% of their initial power conversion efficiency (PCE) after one year, maintaining a VOC of 708 mV, a JSC of 17 mA/cm², and a PCE of 7.98%. In contrast, DSSCs with conventional Pt electrodes exhibited significant performance degradation, with the PCE dropping to just 4.32% by the end of the test period. The results revealed that the DSSCs incorporating PtNP/PANI/g-CN electrodes were able to retain approximately 80% of their initial photovoltaic performance after one year.

The superior stability observed in the PtNP/PANI/g-CN-based devices can be attributed to the synergistic integration of its components: Pt nanoparticles provide high catalytic activity and electrical conductivity; PANI contributes excellent charge transport pathways due to its high intrinsic conductivity and flexible polymeric nature; and g-CN enhances surface area and offers additional active sites for redox reactions. The combination of these materials forms a robust and highly conductive network that effectively resists electrochemical degradation over prolonged operational periods.

Collectively, these findings suggest that PtNP/PANI/g-CN nanocomposite electrodes present a highly promising alternative to conventional Pt electrodes, offering enhanced longevity, stability, and photovoltaic performance. Such advancements represent a significant step toward the development of economically viable, durable, and commercially scalable DSSC technologies.

ACKNOWLEDGMENT

This study was supported by The Scientific and Technological Research Council of Türkiye (TÜBİTAK) under the 1002 - Short Term R&D Funding Program with the project number 124M760.

REFERENCES

- [1] Come Zebra, E.I., van der Windt, H.J., Nhumaio, G., Faaij, A.P.C., 2021. "A review of hybrid renewable energy systems in mini-grids for off-grid electrification in developing countries." Renewable and Sustainable Energy Reviews, 144, 111036.
- [2] Devadiga, D., Selvakumar, M., Shetty, P., Santosh, M.S., 2021. "Recent progress in dye-sensitized solar cell materials and photo-supercapacitors: A review." Journal of Power Sources, 493, 229698.
- [3] Vivek, C.M., Ramkumar, P., Srividhya, P.K., Sivasubramanian, M., 2021. "Recent strategies and trends in implanting renewable energy sources for sustainability A review." Materials Today: Proceedings, 46, 8204–8208.
- [4] Heffron, R., Halbrügge, S., K"orner, M.-F., Obeng-Darko, N.A., Sumarno, T., Wagner, J., Weibelzahl, M., 2021. "Justice in solar energy development." Solar Energy, 218, 68–75.
- [5] Liu, D., Wang, T., Chang, Z., Zheng, N., Xie, Z., Liu, Y., 2021. "Fused or unfused? Two-dimensional non-fullerene acceptors for efficient organic solar cells." Journal of Materials Chemistry A, 9, 2319–2324.
- [6] Kokkonen, M., Talebi, P., Zhou, J., Asgari, S., Soomro, S.A., Elsehrawy, F., Halme, J., Ahmad, S., Hagfeldt, A., Hashmi, S.G., 2021. "Advanced research trends in dye-sensitized solar cells." Journal of Materials Chemistry A, 9, 10527–10545.
- [7] Schileo, G., Grancini, G., 2021. "Lead or no lead? Availability, toxicity, sustainability and environmental impact of lead-free perovskite solar cells." Journal of Materials Chemistry C, 9, 67–76.
- [8] Wan, J., Xia, Y., Fang, J., Zhang, Z., Xu, B., Wang, J., Ai, L., Song, W., Hui, K.N., Fan, X., Li, Y., 2021. "Solution-processed transparent conducting electrodes for flexible organic solar cells with 16.61% efficiency." Nanomicro Letters, 13, 44.
- [9] Qureshi, A.A., Javed, S., Javed, H.M.A., Akram, A., Mustafa, M.S., Ali, U., Nisar, M.Z., 2021. "Facile formation of SnO2-TiO2-based photoanode and Fe3O4@rGO based counter electrode for efficient dye-sensitized solar cells." Materials Science in Semiconductor Processing, 123, 105545.
- [10] Schoden, F., Dotter, M., Knefelkamp, D., Blachowicz, T., Schwenzfeier Hellkamp, E., 2021. "Review of state-of-the-art recycling methods in the context of dye-sensitized solar cells." Energies, 14, 3741.
- [11] Giannouli, M., 2021. "Current status of emerging PV technologies: A comparative study of dye-sensitized, organic, and perovskite solar cells." International Journal of Photoenergy, 2021, 6692858.

- [12] Al Mahdi, H., Leahy, P. G., Alghoul, M., Morrison, A. P., 2024. "A Review of Photovoltaic Module Failure and Degradation Mechanisms: Causes and Detection Techniques." Solar, 4(1), 43-82.
- [13] Khorrambin, S., Ghasemi, S., & Hosseini, S. R., 2022. "Ultrasonically assisted preparation of molybdenum sulfide/graphitic carbon nitride nanohybrid as counter electrode material for dye-sensitized solar cell." Journal of Alloys and Compounds, 929, 167220.
- [14] Pang, B., Lin, S., Shi, Y., Wang, Y., Chen, Y., Ma, S., ... & Dong, L., 2019. "Synthesis of CoFe2O4/graphene composite as a novel counter electrode for high performance dye-sensitized solar cells." Electrochimica Acta, 297, 70-76.
- [15] Karaoğlan, G. K., Hışır, A., Maden, Y. E., Karakuş, M. Ö., & Koca, A. Synthesis, characterization, electrochemical, spectroelectrochemical and dyesensitized solar cell properties of phthalocyanines containing carboxylic acid anchoring groups as photosensitizer. Dyes and Pigments, 2022. 204, 110390.
- [16] Mehmood, U., Hussein, I. A., Harrabi, K., Tabet, N., & Berdiyorov, G. R. Enhanced photovoltaic performance with co-sensitization of a ruthenium (II) sensitizer and an organic dye in dye-sensitized solar cells. RSC Adv. 2016. 6, 7897–7901.
- [17] Rajeev, P.V., Gnanasekar, S., Gothandapani, K., Sellappan, R., Jacob, G., Raghavan, V., Pitchaimuthu, S., Sonar, P., Chandar, N.K., Jeong, S.K., Ahamed, M., Pandiaraj, S., Ramamoorthy, M., Grace, A.N., 2021. "Thermal decomposition derived nano molybdenum nitride for robust counter electrode in dye-sensitized solar cells." Materials Today Communications, 26, 102070.
- [18] Xu, L., Xu, J., Hu, H., Cui, C., Ding, Z., Yan, Y., Lin, P., Wang, P., 2019. "Hierarchical submicroflowers assembled from ultrathin anatase TiO2 nanosheets as light scattering centers in TiO2 photoanodes for dye sensitized solar cells". J. Alloy. Compd. 776, 1002–1008.
- [19] Muchuweni, E., Mombeshora, E. T., Martincigh, B. S., & Nyamori, V. O., 2022. "Graphitic carbon nitride-based new-generation solar cells: Critical challenges, recent breakthroughs and future prospects." Solar Energy, 239, 74-87.
- [20] Huang, Z., Wang, L., Wu, H., Hu, H., Lin, H., Qin, L., Li, Q., 2022. "Shape-controlled synthesis of CuS as a Fenton-like photocatalyst with high catalytic performance and stability." Journal of Alloys and Compounds, 896, 163045.
- [21] Kamarulzaman, U.A., Rahman, M.Y.A., Su'ait, M.S., Umar, A.A., 2021. "Nickel-palladium alloy-reduced graphene oxide as a counter electrode for dyesensitized solar cells." Journal of Molecular Liquids, 326, 115289.
- [22] Ramli, M.A., Mawarnis, E.R., Umar, M.I.A., Rahman, M.Y.A., Fauzia, V., Nurdin, M., Umar, A.A., 2021. "Charge transfer uplift in dye-sensitized solar cells

- using fibrous nanocrystals of platinum-based bimetallic counter electrodes." Surface and Interfaces, 26, 101311.
- [23] Kim, J.H., Hong, S.K., Yoo, S.-J., Woo, C.Y., Choi, J.W., Lee, D., Kang, J.-W., Lee, H.W., Song, M., 2021. "Pt-free, cost-effective and efficient counter electrode with carbon nanotube yarn for solid-state fiber dye sensitized solar cells." Dyes and Pigments, 185, 108855.
- [24] Zatirostami, A., 2021. "SnO2-based DSSC with SnSe counter electrode prepared by sputtering and selenization of Sn: Effect of selenization temperature." [3] Mettam GR, Adams LB. How to prepare an electronic version of your article. In: Jones BS, Smith RZ, editors. Introduction to the electronic age. New York: E-Publishing Inc; 1999. p. 281-304.
- [25] Theerthagiri, J., Senthil, A. R., Madhavan, J., & Maiyalagan, T., 2015. "Recent progress in non-platinum counter electrode materials for dye-sensitized solar cells." ChemElectroChem, 2(7), 928-945.
- [26] Ansari, S.A., Goumri-Said, S., Yadav, H.M., Belarbi, M., Aljaafari, A., Kanoun, M.B., 2021. "Directly grown of NiCo2S4 nanoparticles on a conducting substrate towards the high-performance counter electrode in dye-sensitized solar cell: A combined theoretical and experimental study." Solar Energy Materials and Solar Cells, 225, 111064.
- [27] Gnanasekar, S., Van Le, Q., Nirmala Grace, A., 2021. "Template-free synthesis of vanadium nitride nanopetals (VNNP) as a high-performance counter electrode for dye-sensitized solar cells." Solar Energy, 213, 145–153.
- [28] Han, Q., Liu, S., Liu, Y., Jin, J., Li, D., Cheng, S., Xiong, Y., 2020. "Flexible counter electrodes with a composite carbon/metal nanowire/polymer structure for use in dye-sensitized solar cells." Solar Energy, 208, 469–479.
- [29] Rashidi, S., Heydari, R.K., Esmaeili, S., Tran, N., Thangi, D., Wei, W., 2021. "WS2 and MoS2 counter electrode materials for dye-sensitized solar cells." Progress in Photovoltaics: Research and Applications, 29 (2), 238–261.
- [30] Sowbakkiyavathi, E.S., Murugadoss, V., Sittaramane, R., Dhanusuraman, R., Angaiah, S., 2021. "Cobalt selenide decorated polyaniline composite nanofibers as a newer counter electrode for dye-sensitized solar cell." Polymer Advanced Technologies, 32, 3137–3149.
- [31] Ahmed, U., Shahid, M.M., Shahabuddin, S., Rahim, N.A., Alizadeh, M., Pandey, A.K., Sagadevan, S., 2021. "An efficient platform based on strontium titanate nanocubes interleaved polypyrrole nanohybrid as a counter electrode for dye-sensitized solar cell." Journal of Alloys and Compounds, 860, 158228.
- [32] Vijaya, S., Landi, G., Wu, J.J., Anandan, S., 2020. "Ni3S4/CoS2 mixed-phase nanocomposite as counter electrode for Pt-free dye-sensitized solar cells." Journal of Power Sources, 478, 229068.

- [33] Noorani, B., Ghasemi, S., Hosseini, S.R., 2021. "Nanostructured nickel sulfide/graphene oxide-polypyrrole as a platinum-free counter electrode for dyesensitized solar cell." Journal of Photochemistry and Photobiology A: Chemistry, 405, 112966.
- [34] Tiwari, M., & Joshi, G. C. (2024). "Starch-assisted precipitation synthesis of molybdenum-doped WO3 nanoparticles for the degradation of crystal violet and rhodamine-B dye under direct sunlight irradiation." Journal of Sol-Gel Science and Technology, 1-20.
- [35] Maitra, S., Pal, S., Datta, S., Maitra, T., Dutta, B., Roy, S., 2021. "Nickel-doped molybdenum oxide thin film counter electrodes as a low-cost replacement for platinum in dye-sensitized solar cells." Materials Today: Proceedings, 39, 1856–1861.
- [36] Igman, E., Bayram, O., Mavi, A., Hasar, U.C., Simsek, O., 2020. "Photovoltaic performance of non-covalent functionalized single-layer graphene in dye-sensitized solar cells (DSSCs)." Journal of Materials Science, 56, 4184–4196.
- [37] Nemala, S.S., Ravulapalli, S., Kartikay, P., Banavath, R., Mallick, S., Bhargava, P., Bhushan, M., Mohapatra, D., 2021. "Natural solvent facilitated high-shear exfoliated graphene nanoplatelets enabled economically efficient and stable DSSC." Materials Letters, 287, 129263.
- [38] Sarilmaz, A., Ozen, A., Akyildiz, H., Siyahjani Gulte in, S., Kus, M., Ozel, F., 2021. "Carbon nanotube supported thiospinel quantum dots as counter electrodes for dye-sensitized solar cells." Solar Energy, 221, 243–253.
- [39] Peter, I.J., Vijaya, S., Anandan, S., Nithiananthi, P., 2021. "Sb2S3 entrenched MWCNT composite as a low-cost Pt-free counter electrode for dye-sensitized solar cell and a viewpoint for a photo-powered energy system." Electrochimica Acta, 390, 138864.
- [40] Durairasan, M., Saravanan, K.K., Siva Karthik, P., 2021. "Enhanced performance of dye-sensitized solar cell based g-C3N4/Ag3PO4 hybrid composites as novel electrodes fabricated by facial hydrothermal approach." Journal of Materials Science: Materials in Electronics, 32(5), 5404–5414.
- [41] Altinkaya, C., Atli, A., Atilgan, A., Salimi, K., Yildiz, A., 2020. "Facile fabrication of low-cost low-temperature carbon-based counter electrode with an outstanding fill factor of 73% for dye-sensitized solar cells." International Journal of Energy Research, 44(4), 3160–3170.
- [42] Wang, G., Zhang, J., Hou, S., 2016b. "g-C3N4/conductive carbon black composite as Pt free counter electrode in dye-sensitized solar cells." Materials Research Bulletin, 76, 454–458.

- [43] Afshari, M., Dinari, M., Momeni, M.M., 2018. "Ultrasonic irradiation preparation of graphitic-C3N4/polyaniline nanocomposites as counter electrodes for dye-sensitized solar cells." Ultrasonics Sonochemistry, 42, 631–639.
- [44] Hasija, V., Raizada, P., Singh, P., Verma, N., Khan, A.A.P., Singh, A., Selvasembian, R., Kim, S.Y., Hussain, C.M., Nguyen, V.-H., Le, Q.V., 2021. "Progress on the photocatalytic reduction of hexavalent Cr (VI) using engineered graphitic carbon nitride." Process Safety and Environmental Protection, 152, 663–678.
- [45] Saravanan, V., Lakshmanan, P., Ramalingan, C., 2021. "Alumina surface modified with graphitic carbon nitride: Synthesis, characterization and its application as photocatalyst." Diamond and Related Materials, 114, 108291.
- [46] Wang, G., Kuang, S., Zhang, J., Hou, S., Nian, S., 2016a. "Graphitic carbon nitride/ multiwalled carbon nanotubes composite as Pt-free counter electrode for high efficiency dye-sensitized solar cells." Electrochimica Acta, 187, 243–248.
- [47] Wang, G., Zhang, J., Kuang, S., Zhang, W., 2016c. "Enhanced electrocatalytic performance of a porous g C3N4/graphene composite as a counter electrode for dyesensitized solar cells." Chemistry A European Journal, 22, 11763–11769.
- [48] Faisal, M., Ahmed, J., Jalalah, M., Alsareii, S.A., Alsaiari, M., Harraz, F.A., 2023. "Rapid elimination of antibiotic gemifloxacin mesylate and methylene blue over Pt nanoparticles dispersed chitosan/g-C3N4 ternary visible light photocatalyst." Environmental Science and Pollution Research, 30(22), 61710-61725.
- [49] Guo, F., Li, L., Shi, Y., Shi, W., Yang, X., Li, H., 2023. "Achieving superior anticorrosion and antibiofouling performance of polyaniline/graphitic carbon nitride composite coating." Progress in Organic Coatings, 179, 107512.
- [50] Yang, X., Zhao, L., Wang, S., Li, J., Chi, B., 2021. "Recent progress of g-C3N4 applied in solar cells." J. Materiomics 7, 728–741.
- [51] Aboubakr, A.E.A., El Rouby, W.M.A., Khan, M.D., Revaprasadu, N., Millet, P., 2021. "Effect of morphology and non-metal doping (P and S) on the activity of graphitic carbon nitride toward photoelectrochemical water oxidation." Solar Energy Materials and Solar Cells, 232, 111326.
- [52] Bie, C., Cheng, B., Fan, J., Ho, W., Yu, J., 2021. "Enhanced solar-to-chemical energy conversion of graphitic carbon nitride by two-dimensional cocatalysts." EnergyChem, 3, 100051.
- [53] Rono, N., Kibet, J.K., Martincigh, B.S., Nyamori, V.O., 2021. "A review of the current status of graphitic carbon nitride." Critical Reviews in Solid State and Materials Sciences, 46, 189–217.
- [54] Rono, N., Kibet, J.K., Martincigh, B.S., Nyamori, V.O., 2021. "A comparative study between thermal etching and liquid exfoliation of bulk graphitic carbon nitride

- to nanosheets for the photocatalytic degradation of a model environmental pollutant, Rhodamine B." Journal of Materials Science: Materials in Electronics, 32, 687–706.
- [55] Yuan, H., Liu, J., Li, H., Li, Y., Liu, X., Shi, D., Wu, Q., Jiao, Q., 2018. "Graphitic carbon nitride quantum dot decorated three-dimensional graphene as an efficient metal-free electrocatalyst for triiodide reduction." J. Mater. Chem. A 6, 5603–5607.
- [56] Roy, P., Vats, A. K., Tang, L., Kurokawa, Y., & Pandey, S. S., 2024. "Controlling adsorption of two dyes on TiO2 surface to improve the efficiency of see-through dye-sensitized solar cells." Solar Energy, 269, 112339.
- [57] Wang, L., Wang, C., Hu, X., Xue, H., & Pang, H. 2016d. "Metal/graphitic carbon nitride composites: synthesis, structures, and applications." Chemistry–An Asian Journal, 11(23), 3305-3328.
- [58] Pan, H., Zhang, Y.W., Shenoy, V. B., & Gao, H., 2011. "Ab initio study on a novel photocatalyst: functionalized graphitic carbon nitride nanotube." ACS Catalysis, 1(2), 99-104.
- [59] Shiraishi, Y., Kofuji, Y., Kanazawa, S., Sakamoto, H., Ichikawa, S., Tanaka, S., & Hirai, T., 2014. "Platinum nanoparticles strongly associated with graphitic carbon nitride as efficient co-catalysts for photocatalytic hydrogen evolution under visible light." Chemical communications, 50(96), 15255-15258.
- [60] Sajid, M., Płotka-wasylka, J., 2020. "Nanoparticles: Synthesis, characteristics, and applications in analytical and other sciences." Microchemical Journal, 154, 104623.
- [61] Khan, M. A. R., Al Mamun, M. S., & Ara, M. H., 2021. "Review on platinum nanoparticles: Synthesis, characterization, and applications." Microchemical Journal, 171, 106840.
- [62] Jovanović, A., Bugarčić, M., Marinković, A., Sokić, M., 2023. "Insights Into the Application of Polyaniline-Based Composites in Environmental Engineering." Metallurgical and Materials Data, 1(1), 25-31.
- [63] Yang, H. D., Huang, J. H., Shibata, K., Lu, D., Maeda, K., Hu, C., 2020. "Boosting photocatalytic H2O2 production by coupling of sulfuric acid and 5-sulfosalicylic acid incorporated polyaniline with g-C3N4." Sustainable Energy and Fuels, 4(8), 4186–4195.
- [64] Chen, X., Liu, P., Liu, C., Liu, G., Wei, J., Xu, J., Jiang, Q., Liu, X., Jiang, F., 2021. "Microstructure control for high capacitance polyaniline." Electrochimica Acta, 391, 138977.
- [65] Wu, H.H., Chang, C.W., Lu, D., Maeda, K., Hu C., 2019. "Synergistic effect of hydrochloric acid and phytic acid doping on polyaniline-coupled g-C3N4 nanosheets

for photocatalytic Cr(VI) reduction and dye degradation." ACS Applied Materials Interfaces, 11, 35702–35712.

- [66] Bora, A., Mohan, K., Phukan, P., Dolui, S.K., 2018. "A low-cost carbon black/polyaniline nanotube composite as an efficient electro-catalyst for triiodide reduction in dye-sensitized solar cells." Electrochimica Acta, 259, 233–244.
- [67] Yamauchi, O., Odani, A., Takani, M., 2002. Metal-amino acid chemistry. Weak interactions and related functions of side chain groups, J. Chem. Soc. Dalton Trans. 18, 3411–3421.